UC Berkeley
UC Berkeley Electronic Theses and Dissertations

Title

Development and Implementation of Detailed Soot Surface Oxidation Model into Kinetic Monte Carlo Simulations of Graphene-Edge Oxidation

Permalink

https://escholarship.org/uc/item/9995512f

Author

Singh, Ravi Ishwar

Publication Date

2016

Peer reviewed|Thesis/dissertation

Development and Implementation of Detailed Soot Surface Oxidation Model into Kinetic Monte Carlo Simulations of Graphene-Edge Oxidation

By

Ravi Ishwar Singh

A dissertation submitted in partial satisfaction of the

requirements for the degree of

Doctor of Philosophy

in

Engineering – Mechanical Engineering

in the

Graduate Division

of the

University of California, Berkeley

Committee in charge:

Professor Michael Frenklach, Chair
Professor Jyh-Yuan Chen
Professor K. Birgitta Whaley

Summer 2016

Abstract

Development and Implementation of Detailed Soot Surface Oxidation Model into Kinetic
Monte Carlo Simulations of Graphene-Edge Oxidation

by

Ravi Ishwar Singh

Doctor of Philosophy in Engineering – Mechanical Engineering

University of California, Berkeley

Professor Michael Frenklach, Chair

This dissertation presents a newly established, detailed model of elementary reactions of
soot oxidation. Surface oxidation is the primary mechanism by which carbon is removed
from soot. Previously, soot oxidation has been modeled using a one-step global mechanism
based on chemical analogy to phenyl oxidation. The one-step model, however, is limited
to simple descriptions of surface geometry. Studies of soot growth revealed that chemical
analogy alone is insufficient to describe the reactions taking place at the particle surface.
Steric effects, neighboring sites, and substrate size must also be considered. For soot
growth, studies performed by the Frenklach group found a much richer chemistry than
previously thought to exist, most notably the incorporation of five-member rings into the
substrate leading to curvature of the initially planar aromatics. Recent experimental studies
have found that the soot oxidation rate depends on soot particle curvature, so a one-step
global mechanism is insufficient to explain the experimental observations. The purpose of
developing a detailed kinetic model is to gain a qualitative and quantitative understanding
of oxidation processes of soot particles, large polycyclic aromatics, and graphene edges.

To build the oxidation model, the energetics and kinetics of key elementary oxidation
reactions were investigated. Reaction rate coefficients and product branching ratios were
calculated for the oxidation of six- and five-member ring graphene-edges by molecular
oxygen at temperatures and pressures relevant to combustion. The reactions and their
corresponding rates were added to an existing model of soot surface growth along with
reactions for oxidation of six-member rings by OH, thermal decomposition of oxyradicals,
and O, H, and OH abstraction and addition.

Detailed kinetic Monte Carlo (KMC) simulations of high-temperature oxidation by
molecular oxygen of a graphene sheet were performed using the newly established model
of graphene-edge reactions. The KMC results revealed two principal pathways for an
oxyradical site: oxidation and regeneration of an aromatic radical site. The overall

oxidation rate is computed to be time-dependent, with reactivity decreasing over time as the ratio of reactive edge sites decreases relative to the number of basal-plane carbon atoms. At the same time, the oxidation rate was found to be higher for graphene with a higher initial curvature. Both results are in accord with experimental observations. Analysis showed that distinct aspects of graphene-edge morphology are responsible for curvature either raising or reducing the oxidative reactivity of the graphene edge.

Oxidation pathways for graphene-edge five-member rings reacting with atomic oxygen were investigated. The rate coefficient for oxidation by atomic oxygen exceeded that of for oxidation by molecular oxygen by several orders of magnitude. The detailed surface oxidation model was augmented to include this reaction along with several more abstraction and oxidation reactions.

KMC simulations were then performed in an evolving gas phase environment that was coupled to the surface chemistry for conditions analogous to those of shock tube experiments of soot oxidation at high temperatures. The KMC results showed that the oxidation rate was dependent on several factors. CO concentration profiles calculated from the KMC model were found to be in agreement with experimental measurements.

Table of contents

List of figures

List of tables

Acknowledgments

I am tremendously grateful for all of the people in my life who have helped make this dissertation possible. I would like to begin by thanking my adviser, Professor Michael Frenklach, for his continuous guidance and support throughout my doctoral studies. He has helped me to improve my research, analytical, technical writing, and presentation skills.

Along with my adviser, I would also like to thank the other members of my dissertation committee: Professor K. Birgitta Whaley and Professor Jyh-Yuan Chen, for their time and insightful comments which contributed to this dissertation.

During my time at Berkeley, I have enjoyed collaborations with two computational chemistry groups. Professor Alexander Mebel at Florida International University and his postdoctoral researcher Vadim Kislov performed quantum chemical calculations for the oxidation of aromatics that were crucial to the work presented in this dissertation. Professor Mebel's expertise in the field of computational chemistry and his friendly disposition made him a pleasure to work with. I was also fortunate to collaborate Professor William A. Lester Jr. and his postdoctoral researcher Srimanta Pakhira. I greatly appreciated my discussions with Professor Lester and the wisdom he provided about many subjects.

I would like to thank my lab mates for all of their support. David Edwards helped me get acclimated to the group. He taught me how to use MultiWell as well as all of the basics of soot oxidation. Even though he had already graduated, Russell Whitesides promptly and helpfully answered any question that I had regarding the KMC code that he developed during his studies. I have also been privileged to work with and get to know Matt Speight, Jim Oreluk, Wenyu Li, and Zhenyuan Liu. I will miss sharing an office with them.

Lastly, I would like to thank my family for everything that they have done for me. My parents always supported me and encouraged me to follow my passion, whether it was to play baseball, join the drumline, or study engineering. My sister, Indira, has inspires me with her powerful self-motivation and determination. To Jillian, my girlfriend, I could not have reached where I am today without your love. Throughout the last three and half years, she has always been there for me no matter how many miles away we were, and I cannot thank her enough.

1 Introduction

1.1 Soot Background

Energy generation is essential for society to maintain a high standard of living. The strength of industry, speed of transportation, and the many comforts and conveniences of the household and workplace require the efficient utilization of energy, the majority of which is generated from the burning of fossil fuels such as coal, oil, and natural gas. The Energy Information Administration (EIA) stated in their 2015 Annual Energy Outlook report that combustion is the basis for over 84 % of the energy produced in the United States of America (USA) and that the overall energy mix is not expected to change dramatically over the next 25 years [1]. The harvesting of energy through burning of fuels poses a major problem regarding the formation of pollutants that include CO, CO_2, O_3, NO_x, SO_x, and soot (particulate matter). While the emissions for all of the listed species should be taken into account when designing combustion devices, this dissertation will concentrate on the formation of soot.

Soot is a mass of solid carbon particles that are formed in fuel rich zones during combustion. Soot is composed of approximately eight parts of carbon to one part of hydrogen by moles [2] but also contains trace amounts of zinc, phosphorus, calcium, iron, silicon, and chromium [3-6]. While soot emissions can have positive effects on combustion such as enhancing heat transfer through radiation, they also impose negative consequences on human health and the environment.

Early studies linked inhalation of larger soot particles (particulate matter PM_{10}; diameter < 10 μm) to a wide range of serious health effects, including chronic lung disease, lung cancer, asthma attacks, cardiovascular disease, and strokes [7]. Later studies would show that smaller soot particles ($PM_{2.5}$ and $PM_{0.1}$) were actually more closely correlated with those negative health outcomes due to their ability to more easily penetrate into the lungs [8].

In addition to the health risks associated with exposure to soot, there are also climate change issues with soot emissions. The most recent estimate of the total climate forcing caused by soot is +1.1 W m^{-2} which is higher than that of noted greenhouse gas methane (+0.86 W m^{-2}) and second only to the climate forcing of carbon dioxide (+1.56 W m^{-2}) [9]. The major mechanism of climate forcing for soot is the absorption of solar radiation by airborne particles which leads to warming of the atmosphere. Deposition of particles onto snow and ice can also lead to melting due to increased solar absorption.

Due to its adverse effects, soot is a regulated pollutant in many countries. In the USA, the Environmental Protection Agency (EPA) regulates particulate matter emissions, which include soot, through the Federal Clean Air Act. In 1997, the annual standard for $PM_{2.5}$ emissions allowed was set to 15 μg/m^3. In 2012, the EPA issued a more restrictive standard of 12 μg/m^3 for the protection of public health and the environment [10].

Given the EPA regulations for particulate matter, soot emissions are an important design constraint when developing new combustion devices. Soot formation is a complex process due to its complex and strongly interlinked chemical and physical processes which include gas phase chemistry, surface chemistry, and particle dynamics. As a result, the design of prototypes that attempt to control parameters like particle size and number density are based on a trial-and-error approach that can be quite costly and time consuming. As an alternative approach, we can work to create predictive and robust computational models for soot. The models can provide insight into the underlying physical and chemical mechanisms driving the process and be used to develop combustion devices with greater control over soot formation. To do this, we must understand how soot is produced.

1.2 Soot Formation

Although the soot formation process is complex and yields many unanswered questions, here is what is known. Soot precursors form in the gas phase and nucleation of the precursors produces particles. Next, particles collide with other particles to form larger particles (coagulation) or collide while maintaining their shape (agglomeration). Simultaneously, heterogeneous reactions take place at the particle surface. The surface reactions include surface growth in which gas phase species are adsorbed to the surface, and surface oxidation which removes carbon from the soot [2, 11, 12]. Figure 1.1 shows an illustration of the soot formation process.
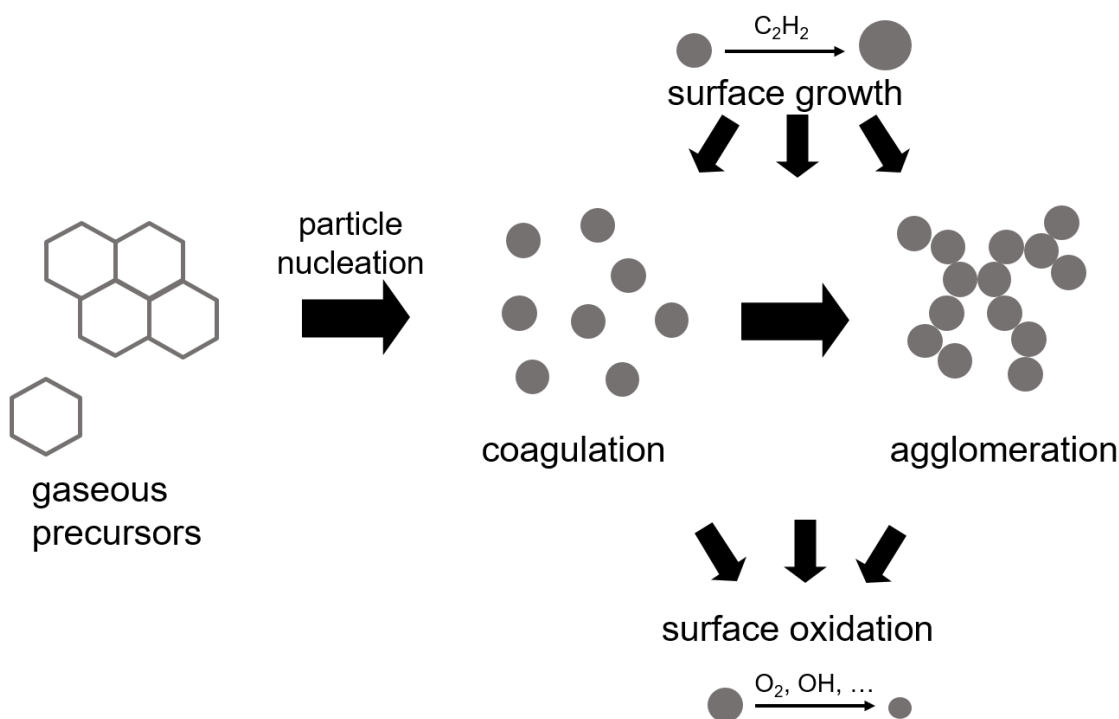
Figure 1.1. Schematic diagram of the soot formation process.

The research presented in this dissertation focuses on the surface chemistry, and oxidation in particular. Before describing how soot surface reactions are modeled, I will include a brief primer on the nomenclature used when discussing soot surface reactions.

1.2.1 Soot Surface Nomenclature

The soot particle is composed of stacks of large molecules called polycyclic aromatic hydrocarbons or PAHs [11]. When investigating reactions that occur on soot edges, theoretical studies have postulated that the soot edge reactions can be thought of as being chemically analogous to reactions of PAH edges [13, 14]. Figure 1.2 shows an example of a PAH that can be thought of as being chemically similar to a soot edge.
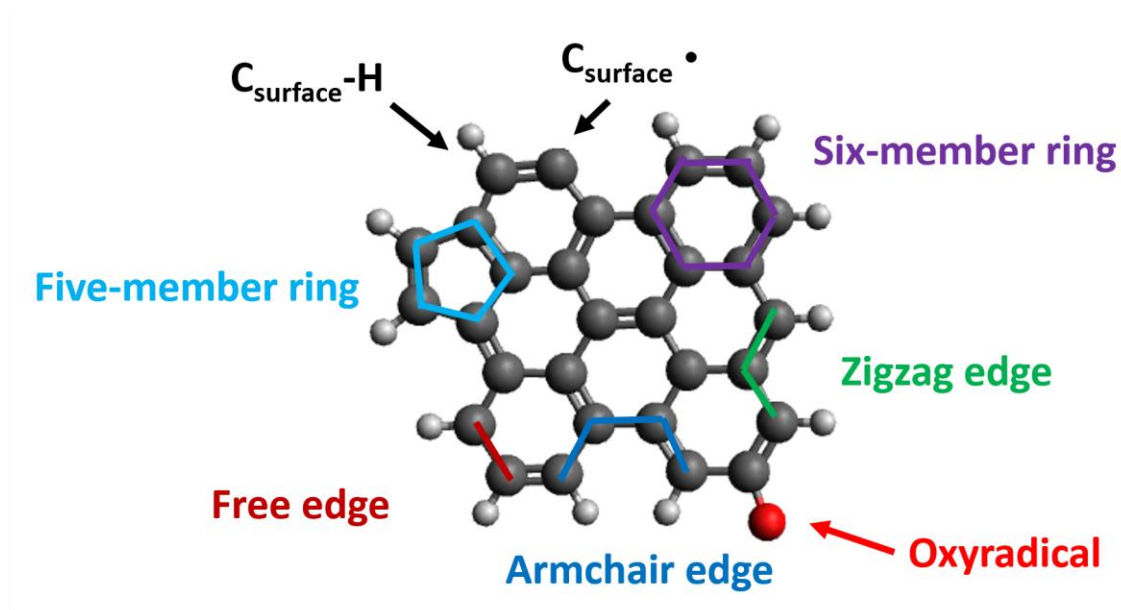
Figure 1.2. Example of PAH with key terms labeled.

The graphene sheet is made up of six- and five- member rings. Six member rings consist of six carbon atoms in a hexagonal shape. Five-member rings can also form, and their introduction into to the PAH induces curvature. Surface reactions occur along the edges of the graphene. The edge site carbon atoms can have radical sites ($C_{surface}•$), bond to hydrogen ($C_{surface}$–H), or bond to oxygen to form an oxyradical. The carbon atoms not on the edge are called basal-plane carbon atoms. There are several types of edges that include zigzag, armchair, and free edges. All of these terms will be referred to repeatedly throughout this dissertation when discussing surface reactions.

1.3 Modeling of Surface Reactions

Mechanistic modeling of soot-particle surface chemistry began with postulating chemical similarity between growth of particle constituent graphene edges and gas-phase polycyclic aromatic hydrocarbons (PAH) [13, 14]. Being able to explain much of the soot formation phenomena [11], the initial models limited the aromatic extension to the planar growth.

A much richer chemistry was discovered in subsequent theoretical studies [15-20], revealing migration of five-member aromatic rings: "free migration" over the growing

graphene edge [15] and "embedded migration" within the grown layer of graphene [16]. The migrating five-member rings turned out to transform (isomerize) into six-member rings [18]. The evolution of graphene edges with the newly-established five-member-ring chemistry exhibited bending of graphene sheets [21].

All of these studies were focused on PAH and graphene-edge growth chemistry. At that time, oxidation had received less attention. In the 1990's, Frenklach and co-workers proposed a model of soot oxidation containing two principal steps: the reaction of O_2 with a surface radical site, and the attack of OH on a generic surface site [14, 22]. For each reaction, one C atom was assumed to be removed for every O atom of the gaseous reactant, and a fresh surface site was regenerated. The rate coefficient for the oxidation by O_2 step was assigned by analogy to that of phenyl oxidation [23]. Oxidation by OH was described by using the collision efficiency values reported in flame experiments [24]. While this oxidation model has been utilized in studies of soot oxidation [25], it does not account for steric effects. Given the significance of the effects of soot morphology found for surface growth, further study of oxidation pathways was merited.

Initial studies concerning the oxidation of aromatics found that oxyradicals were a key intermediate formed that could then thermally decompose into five-member rings and produce CO [25-32]. The Frenklach group investigated the thermodynamic stability of zigzag and armchair graphene-edge oxyradicals [33, 34] and discovered that thermodynamic stability varied significantly depending on the location of the oxyradical site and was correlated with substrate aromaticity. The Frenklach group proceeded to investigate the kinetics of the thermal decomposition of oxyradicals on zigzag and armchair edges [35, 36]. These studies found that the rate coefficient for decomposition of a six-member ring oxyradical to form a five-member ring and CO depended on the number of "free edges" on either side of the $C - O$ bond with the rate being higher for more free edges. After gaining insight into the thermal decomposition of oxyradicals, the focus moved to the initial oxidation step. Because OH is thought to be the primary oxidizer of soot [37], Edwards et al. [38] investigated the oxidation reaction of phenanthryl radical with OH using B3LYP and CBS-QB3 calculations of pertinent potential energy surfaces and RRKM-ME calculations of rate coefficients. They found that the reaction proceeds by OH addition to the radical site followed by H atom migration/elimination and by oxyradical decomposition via expulsion of the CO group. After studying soot oxidation by OH, the next step was to study the pathways for oxidation of soot by O_2.

1.4 Overview

In this dissertation, I discuss how I developed a detailed model of soot surface oxidation and present the results of kinetic Monte Carlo (KMC) simulations of graphene-edge oxidation at high-temperature that utilize the model. Chapter 2 presents the methodologies used to investigate reaction pathways, calculate reaction rate coefficients and product branching ratios, simulate surface oxidation of graphene-edges. Chapters 3 and 4 give the reaction rate analysis for the oxidation of six- and five-member rings, respectively, by molecular oxygen. In Chapter 5, the results of KMC simulations using the detailed surface oxidation model are presented. The simulations elucidate major kinetic features of

graphene-edge oxidation and reproduce experimentally-observed phenomena regarding curvature effects on oxidation rate. Chapter 6 presents reaction rate analysis for an oxidation pathway in which a graphene-edge five-member ring is oxidized by atomic oxygen. This pathway is shown to be kinetically favorable to the analogous reaction of a five-member ring with molecular oxygen. Chapter 7 shows how KMC simulations were augmented by coupling the surface reactions to the evolving gas phase environment of a Plug Flow Reactor (PFR) and presents the subsequent results of high-temperature oxidation simulations which are in accord with published experimental data from shock tube studies. Lastly, Chapter 8 synthesizes the conclusions from the previous chapters and discusses future work that will be done with the surface oxidation model.

2 Methodology

2.1 Reaction Rate Coefficient Calculations

2.1.1 Master Equation Modeling

The rate coefficients of the systems studied were calculated using the MultiWell suite of codes [39-41]. MultiWell solves the one-dimensional time-dependent energy-transfer master equations for a multi-well and multi-channel unimolecular reaction system using a stochastic approach [42, 43]. Microcanonical rate coefficients for all elementary reactions studied were computed with MultiWell at the Rice-Ramsperger-Kassel-Marcus (RRKM) level of theory. The latest version of the MultiWell code was used for each of the reactions studied. Results found using earlier versions of MultiWell were checked against newer versions to ensure that the values were not affected by updates to the code.

Key parameters required for the MultiWell simulations, such as reaction barriers, frequencies, and moments of inertia were taken from the quantum-chemical calculations of the present study. Following Gilbert and Smith [44], vibrational frequencies were examined by graphically visualizing the associated normal mode vibrations to identify internal rotational modes and, accordingly, all internal rotors were treated as 1-D hindered rotors.

Rate coefficients were computed at temperatures and pressures relevant to combustion (1000 – 2500 K; 0.01 – 100 atm). Argon was chosen as the bath gas collider. The collisional energy transfer probability was estimated by the exponential-down model. For the calculations described in Chapters 3 and 4, the quantity $\langle \Delta E \rangle_{\text{down}}$ was held at a constant value of 260 cm^{-1} as done in previous studies by the Frenklach group [16-19, 35, 36]. For the computations detailed in Chapter 6, $\langle \Delta E \rangle_{\text{down}}$ was varied using the temperature-dependent expression of Hippler et al. [45]. Lennard-Jones parameters were estimated from an empirical correlation [46]. An energy grain size of 15 cm^{-1} for the first segment of the double array and a maximum energy of 500,000 cm^{-1} were used to determine the density of states. For each set of initial conditions, the number of trials was varied to keep statistical error below 5 %.

MultiWell simulations can be used to calculate rate coefficients for thermal decomposition and chemical activation reactions, but all of the reactions studied here fall into the latter category. The chemical-activated rate coefficients were derived from the accumulated species fractions of the products, as was done previously [16-19, 35, 36, 38]. The accumulated species fractions were found by running a MultiWell simulation started with a chemical-activated initial energy distribution. The species fractions were found after the average energy of the initial adduct converges to a constant value, indicating the end of the chemically-activated simulation. Product formation rates were obtained by multiplying the

product fractions by the high-pressure reaction rate coefficient of the adduct formation reaction.

High-pressure-limit rate coefficients for product formation were calculated by using the high-pressure-limit rate coefficients of all well-to-well channels involved in the reactant-to-product reaction path and numerically solving a differential equation system of the corresponding species rate equations. For the computations, an excess of the reactant O_2 was utilized so that the high-pressure-limit rate coefficient could be found by measuring the slope of the reactant profile. This rate was then multiplied by the product fractions to determine the product formation rates in the high-pressure limit.

2.1.2 Barrierless Reaction Rate Coefficient Calculations

Calculations of thermal rate coefficients for the barrierless channels were carried out using variable reaction coordinate-transition state theory (VRC-TST) in the VariFlex code developed by Klippenstein and co-workers [47, 48]. Briefly, the VRC-TST approach separates the transition state's degrees of freedom into "conserved" and "transitional" modes. The conserved modes marginally change over the reaction process and are treated as rigid rotors or harmonic oscillators by directly computing the corresponding sums of states. The transitional modes are treated classically through a phase-space integral. Then, the partition function of a transition state is calculated through a convolution of these two types of modes, by varying the distance along the reaction coordinate and recalculating the contribution of the transitional modes to the partition function until a minimum reaction rate is found [47]. VariFlex calculates the microcanonical rate coefficients which can be used as inputs for MultiWell simulations thereby enabling MultiWell to account for barrierless channels.

The VariFlex calculations require inputs that are similar to those used in MultiWell (bond dissociation energies, frequencies, moments of inertia, etc.). The energy grain sizes and maximum energy used in VariFlex must be the same as those used in the MultiWell calculations. Additionally, the VRC-TST calculations necessitate calculation of the potential along the minimal energy reaction path (MEP). Details about the potentials used for each calculation are given in the chapters for those particular reactions.

2.2 Kinetic Monte Carlo Simulations

Since the early 1990's, the Frenklach group has utilized Monte Carlo simulations to study topics including diamond surface growth [49, 50], particle aggregation [51], and soot surface growth [15, 52]. The aromatic growth model developed by Frenklach, Schuetz, and Ping (FSP) was able to simulate surface reactions including ring adsorption, desorption, and transformations, as well as migration of five-member rings. This kinetic model had some limitations, namely that it restricted growth to one direction, did not account for substrate curvature, and made steady state assumptions for several intermediates due to

computational constraints. Whitesides and Frenklach improved upon the FSP model by creating a kinetic Monte Carlo (KMC) model for graphene-edge growth that contained a more detailed description of elementary surface reactions and allowed for substrate curvature by linking itself to a Molecular Mechanics (MM) geometry optimization package [21]. The KMC methodology is this dissertation follows from the work of Whitesides and Frenklach [21, 53].

The KMC simulations tracked a single graphene "molecule" evolving in a flame-like environment, but maintaining the gas phase in a constant state, i.e., at constant values of temperature, pressure, and species mole fractions, which allowed us to investigate unambiguously the influence of individual factors on the simulation outcome. At each time step, a reaction event was selected stochastically and then applied.

The processes of surface growth and oxidation were modeled as a Markovian sequence of reaction events. There are two types of reactions that comprise the present model: bimolecular reactions between the gaseous species and surface sites, and unimolecular ''decompositions'' of surface species. All stochastic events were treated as first-order processes, with the respective per-site rates. The second-order reactions produced pseudo-first-order rate constants through multiplication of the gas-surface rate coefficient by the concentration of the gaseous reactant. The selection of the reaction event and specific graphene-edge site was done by application of the Gillespie algorithm [42, 43] adapted for surface processes [49, 50]. Briefly, given an instant of a current reaction event, t_n, the time of the next reaction event to occur at substrate site i is $t_{n+1,i} = t_n - (\ln u)/k_{\text{total},i}$, where u is a random number distributed uniformly from 0 to 1 ($Unif(0,1)$) and $k_{\text{total},i} = \Sigma_j k_{j,i}$ is the sum of the per-site rates of reactions possible at site i. The smallest among the $t_{n+1,i}$ values, computed for all surface reaction sites, becomes the time instant of the next reaction event, t_{n+1}, and the particular reaction to occur at that time is chosen according its probability $p_{j,i} = k_{j,i}/k_{\text{total},i}$ upon drawing another random number u. Once a reaction event is implemented, the process repeats itself.

To properly account for the evolving curvature, the KMC model was coupled to molecular-mechanics geometry optimization using the MM3 potential [54] with the TINKER molecular mechanics package [55]. The MM3 potential has been found to produce geometries for fullerenes in good agreement with the ab initio Hartree-Fock method [56] as well as experimental and DFT results for fullerenic fragments [57]. Optimization of the structure geometry was performed after each structure-changing event. The geometry optimization step properly accounted for substrate curvature while maintaining physically accurate bonding and geometric configuration of the evolving structures. A check was made after each geometry optimization to ensure that the geometry produced by the molecular mechanics code was consistent with the bonding implied by the KMC model. Specifically, the code tested if the geometry optimization left all carbon atoms within a specified distance of the other atoms to which they were bonded in the KMC description. If any two carbon bonds were found to be separated by more than two angstroms, the simulation was ended.
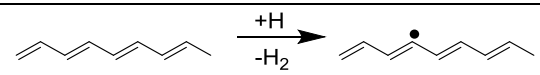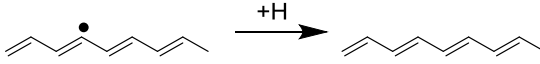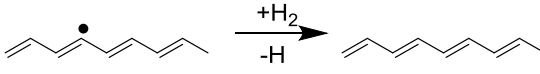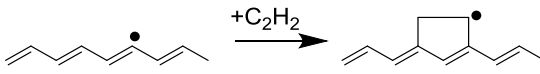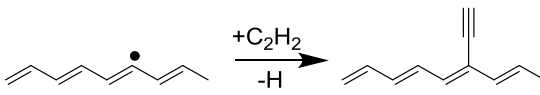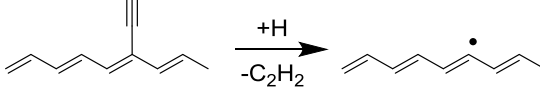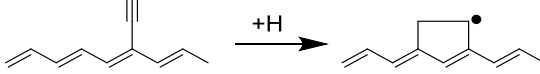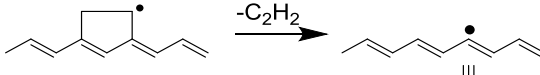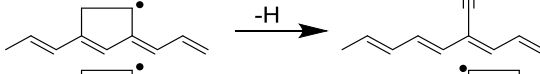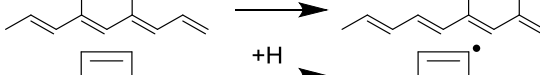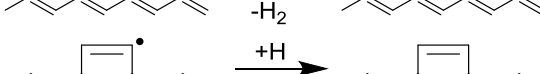
The evolution of the graphene structure was monitored by computing the numbers of reaction events, instantaneous substrate size, and its five-member ring fraction, f_{R5}, the latter defined as [53]

$$f_{R5} = \frac{32}{12} \frac{N_{R5}}{N_{R5} + N_{R6}},$$ (1)

where N_{R5} and N_{R6} are the number of five- and six-member rings, respectively, and the 32/12 coefficient normalizes Eq. 1 to have $f_{R5} = 1$ for buckminsterfullerene, C_{60}.

The set of surface reactions employed in the current KMC model contains 45 growth and 59 oxidation reactions. The reaction model of soot surface growth and oxidation is presented in Table 2.1. The rates for each reaction (k's) are pseudo-first order with units of s^{-1}.

Table 2.1. KMC reactions.

	reaction	per-site rate coefficient (s, mol/cm^3, K)
1	$\xrightarrow[-H_2]{+H}$	$k_1 = 4.2 \times 10^{13} e^{-8052/T} [H]$
2a	$\xrightarrow{+H}$	$k_{2a} = 2 \times 10^{13} [H]$
2b	$\xrightarrow[-H]{+H_2}$	$k_{2b} = \dfrac{k_1}{7.59 e^{-2097/T}} \dfrac{[H_2]}{[H]}$
3	$\xrightarrow{+C_2H_2}$	$k_3 = \dfrac{k_a k_b}{k_b + k_c + k_d} [C_2H_2]$
4	$\xrightarrow[-H]{+C_2H_2}$	$k_4 = \dfrac{k_a k_d}{k_b + k_c + k_d} [C_2H_2]$
5	$\xrightarrow[-C_2H_2]{+H}$	$k_5 = \dfrac{k_c k_e}{k_b + k_c + k_d} [H]$
6	$\xrightarrow{+H}$	$k_6 = \dfrac{k_b k_e}{k_b + k_c + k_d} [H]$
7	$\xrightarrow{-C_2H_2}$	$k_7 = 3.1 \times 10^{11} T^{0.87} e^{-37403/T}$
8	$\xrightarrow{-H}$	$k_8 = 6.7 \times 10^{11} T^{0.84} e^{-35625/T}$
9	$\xrightarrow{}$	$k_9 = 1.3 \times 10^{11} T^{0.16} e^{-23099/T}$
10	$\xrightarrow[-H_2]{+H}$	$k_{10} = 5.07 \times 10^{7} T^{1.93} e^{-6518/T} [H]$
11a	$\xrightarrow{+H}$	$k_{11a} = 6.08 \times 10^{12} T^{0.27} e^{-141/T} [H]$

9
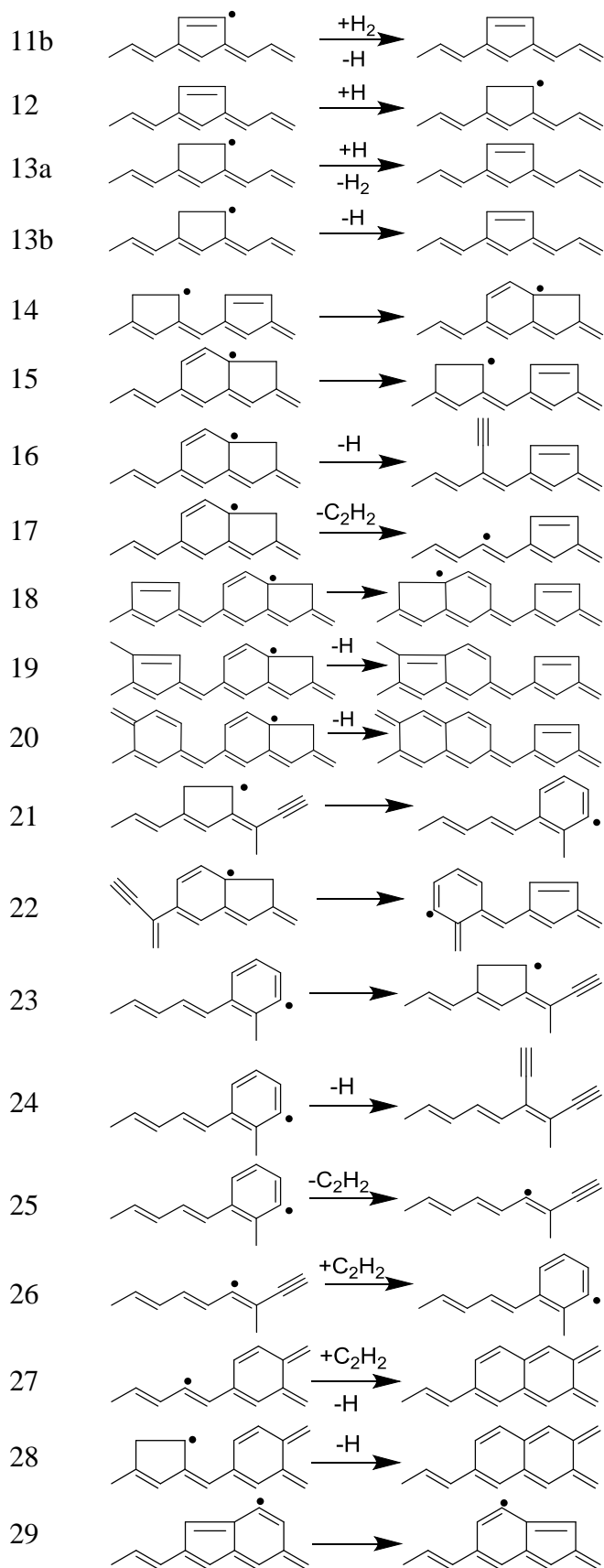
11b		$+H_2$ / $-H$	$k_{11b} = 9.46 \times 10^3 T^{2.56} e^{-2529/T} [H_2]$
12		$+H$	$k_{12} = 5.40 \times 10^{11} T^{0.45} e^{-916/T} [H]$
13a		$+H$ / $-H_2$	$k_{13a} = 2 \times 10^{12} [H]$
13b		$-H$	$k_{13b} = \dfrac{k_{12}}{1.791 e^{17708/T}}$
14			$k_{14} = 8.9 \times 10^5 T^{2.28} e^{-30944/T}$
15			$k_{15} = 2.1 \times 10^9 T^{1.14} e^{-41952/T}$
16		$-H$	$k_{16} = 3.8 \times 10^{10} T^{1.30} e^{-51929/T}$
17		$-C_2H_2$	$k_{17} = 4.0 \times 10^{10} T^{1.53} e^{-57225/T}$
18			$k_{18} = k_{15}$
19		$-H$	$k_{19} = k_{15}$
20		$-H$	$k_{20} = k_{15}$
21			$k_{21} = k_9$
22			$k_{22} = k_{15}$
23			$k_{23} = \dfrac{k_9}{k_7 + k_8 + k_9} 1.3 \times 10^{11} T^{1.08} e^{-35428/T}$
24		$-H$	$k_{24} = \dfrac{k_8}{k_7 + k_8 + k_9} 1.3 \times 10^{11} T^{1.08} e^{-35428/T}$
25		$-C_2H_2$	$k_{25} = \dfrac{k_7}{k_7 + k_8 + k_9} 1.3 \times 10^{11} T^{1.08} e^{-35428/T}$
26		$+C_2H_2$	$k_{26} = \dfrac{k_a k_f}{k_c + k_d + k_f} [C_2H_2]$
27		$+C_2H_2$ / $-H$	$k_{27} = 1.9 \times 10^{10} T^{0.712} e^{-4893/T} [C_2H_2]$
28		$-H$	$k_{28} = k_9$
29			$p_{29} = 0.5$

30 $p_{30} = 0.5$

31 $p_{31} = 2/3$

32 $p_{32} = 1/3$

33 $+C_2H_2$ $\quad k_{33} = \dfrac{k_{17}}{3.24 \times 10^3 e^{-52539/T}} [C_2H_2]$

34 $+C_2H_2$ $\quad k_{34} = k_{33}$

35 $+C_2H_2$, $-H$ $\quad k_{35} = 1.0 \times 10^{10} T^{0.955} e^{-5326/T} [C_2H_2]$

36 $\quad k_{36} = 7.0 \times 10^{10} T^{0.018} e^{6059/T} [H]$

37 $-H$ $\quad k_{37} = k_9$

38 $-H$ $\quad k_{38} = k_{15}$

39 $+C_2H_2$ $\quad k_{39} = k_{33}$

40 $-H$ $\quad k_{40} = 3.49 \times 10^{12} T^{-0.39} e^{-1228/T}$

41 $-H$ $\quad k_{41} = 3.86 \times 10^{11} T^{-0.21} e^{-8908/T}$

42 $+CH_3$, $-H$ $\quad k_{42} = 1.0 \times 10^{13} [CH_3]$

43 $\quad p_{43} = 1/3$

44 $+\bigcirc$, $-H$ $\quad k_{44} = 1.90 \times 10^{76} T^{-18.90} e^{-19884/T} [A1]$

45 $+H$, $-\bigcirc$ $\quad k_{45} = \dfrac{k_{44}}{1.45 \times 10^{-13} T^{3.23} e^{3998/T}} \dfrac{[H]}{[A1]}$

46 $+O_2$, $-O$ $\quad k_{46} = 3.17 \times 10^{13} e^{-1017/T} [O_2]$

47 $+O_2$, $-O$ $\quad k_{47} = k_{46}$

48 $+O_2$, $-O$ $\quad k_{48} = 3.91 \times 10^{13} e^{-1496/T} [O_2]$

49 $\xrightarrow[-O]{+O_2}$ $k_{49} = k_{48}$

50 $\xrightarrow[-O]{+O_2}$ $k_{50} = k_{48}$

51 $\xrightarrow{-CO}$ $k_{51} = 1.08 \times 10^2 T^{3.28} e^{-21866/T}$

52 $\xrightarrow{-CO}$ $k_{52} = 4.02 \times 10^{-2} T^{4.38} e^{-24624/T}$

53 $\xrightarrow{-CO}$ $k_{53} = 6.42 \times 10^{10} T^{1.00} e^{-29183/T}$

54 $\xrightarrow{-CO}$ $k_{54} = k_{53}$

55 $\xrightarrow{+OH}$ $k_{55} = 1.47 \times 10^{14} e^{-632/T} [\text{OH}]$

56 $\xrightarrow{+OH}$ $k_{56} = k_{55}$

57 $\xrightarrow{+OH}$ $k_{57} = k_{55}$

58 $\xrightarrow{+OH}$ $k_{58} = k_{55}$

59 $\xrightarrow{+OH}$ $k_{59} = k_{55}$

60 $\xrightarrow{-H}$ $k_{60} = 2.13 \times 10^{15} e^{-42305/T}$

61 $\xrightarrow{-H}$ $k_{61} = k_{60}$

62 $\xrightarrow{-H}$ $k_{62} = k_{60}$

63 $\xrightarrow{-H}$ $k_{63} = k_{60}$

64 $\xrightarrow{-H}$ $k_{64} = k_{60}$

65 $\xrightarrow{+H}$ $k_{65} = 4.34 \times 10^{14} e^{-984/T} [\text{H}]$

66 $\qquad$ $k_{66} = k_{65}$

67 $\qquad$ $k_{67} = k_{65}$

68 $\qquad$ $k_{68} = k_{65}$

69 $\qquad$ $k_{69} = k_{65}$

70 $\qquad$ $k_{70} = 2.14 \times 10^{16} e^{-52988/T}$

71 $\qquad$ $k_{71} = k_{70}$

72 $\qquad$ $k_{72} = k_{70}$

73 $\qquad$ $k_{73} = k_{70}$

74 $\qquad$ $k_{74} = k_{70}$

75 $\qquad$ $k_{75} = 1.14 \times 10^{12} \left(\dfrac{T}{300} \right)^{2.117} e^{-5603/T} [\text{H}]$

76 $\qquad$ $k_{76} = k_{75}$

77 $\qquad$ $k_{77} = k_{75}$

78 $\qquad$ $k_{78} = k_{75}$

79 $\qquad$ $k_{79} = k_{75}$

80 $\qquad$ $k_{80} = 1.70 \times 10^{14} e^{-9635/T} [\text{H}_2]$

81 $\qquad$ $k_{81} = k_{80}$

82 $\qquad$ $k_{82} = k_{80}$

83 $\qquad$ $k_{83} = k_{80}$

84    $\xrightarrow[\;-H\;]{+H_2}$ $k_{84} = k_{80}$

85    $\xrightarrow[\;-H_2O\;]{+H}$ $k_{85} = 2.00 \times 10^{14} e^{-2670/T} [H]$

86    $\xrightarrow[\;-H_2O\;]{+H}$ $k_{86} = k_{85}$

87    $\xrightarrow[\;-H_2O\;]{+H}$ $k_{87} = k_{85}$

88    $\xrightarrow[\;-H_2O\;]{+H}$ $k_{88} = k_{85}$

89    $\xrightarrow[\;-H_2O\;]{+H}$ $k_{89} = k_{85}$

90    $\xrightarrow[\;-CO_2\;]{+O_2}$ $k_{90} = 3.45 \times 10^{11} e^{-13422/T} [O_2]$

91    $\xrightarrow[\;-HO_2\;]{+O_2}$ $k_{91} = 1.05 \times 10^{13} e^{-30190/T} [O_2]$

92    $\xrightarrow[\;-H_2O\;]{+OH}$ $k_{92} = 3.88 \times 10^{3} T^{2.683} e^{-369/T} [OH]$

93    $\xrightarrow[\;-H\;]{+O}$ $k_{93} = 4.0 \times 10^{12} e^{-2328/T} [O]$

94    $\xrightarrow[\;-H\;]{+O}$ $k_{94} = k_{93}$

95    $\xrightarrow[\;-H\;]{+O}$ $k_{95} = k_{93}$

96    $\xrightarrow[\substack{-CO \\ -H}]{+OH}$ $k_{96} = 1.0 \times 10^{14} [OH]$

97    $\xrightarrow[\substack{-CO \\ -H}]{+OH}$ $k_{97} = k_{96}$

98    $\xrightarrow[\substack{-CO \\ -H}]{+OH}$ $k_{98} = k_{96}$

99    $\xrightarrow[\substack{-CO \\ -H}]{+OH}$ $k_{99} = k_{96}$

100	+H$_2$O, -CO, -H$_2$	$k_{100} = 1.0 \times 10^{12}[\text{H}_2\text{O}]$
101	+H$_2$O, -CO, -H$_2$	$k_{101} = k_{100}$
102	+H$_2$O, -CO, -H$_2$	$k_{102} = k_{100}$
103	+H$_2$O, -CO, -H$_2$	$k_{103} = k_{100}$
104	+O, -CO	$k_{104} = 6.29 \times 10^{12}\left(\dfrac{T}{298}\right)^{0.505} e^{-306/T}[\text{O}]$

For reactions 3 – 6 and 26: $k_a = 1.1 \times 10^7 T^{1.71} e^{-1960/T}$, $k_b = 6.8 \times 10^{11} e^{-11084/T}$,

$k_c = 1.3 \times 10^{14} e^{-21025/T}$, $k_d = 4.8 \times 10^{12} e^{-16875/T}$, $k_e = 1.5 \times 10^{10} T^{0.85} e^{-601/T}$,

$k_f = 2.5 \times 10^{12} T^{-0.13} e^{-7902/T}$

Reactions 1 – 45. The surface growth reactions and their corresponding rate coefficients are taken from Whitesides and Frenklach [21, 53] and further discussion of those reactions can be found in those studies. Reactions 2, 11, and 13 each occur in two different ways and are expressed as parts (a) and (b) in Table 2.1. For the simulations presented in Chapter 5 where the gas phase composition is constant, the reaction rates for those three reactions have been combined as the consumption or production of gas phase species by the surface reactions did not need to be considered. For the KMC simulations discussed in Chapter 7, those reactions were split into two parts to properly account for the change in the gas phase species involved in the reactions.

Reactions 46 – 50. The calculation of rate coefficients for the oxidation of six-member rings by O$_2$ is discussed in detail in Chapter 3. Reactions 46 and 47 were assigned the high-pressure-limit rate coefficients computed for the prototype reaction of phenyl + O$_2$ → phenoxy + O. The rate coefficients for reactions 48, 49, and 50 are taken from the calculation of pyrenyl + O$_2$ → pyrenoxy + O.

Reactions 51 – 54. The rates of thermal decomposition of oxyradicals were taken from the RRKM-ME calculations performed by Edwards et al. [35] for the decomposition of graphene armchair oxyradicals. The study found that the rate coefficients depended on the position of the radical site could affect product yields. Reaction 51 was given the high-pressure-limit rate coefficients of (R1) from Edwards et al. [35]. Reaction 52 corresponds with (R2), and reactions 53 and 54 were assigned the rate coefficients for (R3).

Reactions 55 – 59. The attack of OH on a radical site to form an R-OH site was taken from the RRKM-ME calculations of rate coefficients for the reaction phenanthryl + OH performed by Edwards et al. [38].

Reactions 60 – 64. The elimination of H from R-OH to form an oxyradical is also taken from Edwards et al. [38].

Reactions 65 – 69. The rate for H addition to an oxyradical was computed using the rate coefficients for reactions 60 – 64 and the corresponding equilibrium constants of reactions 65 – 69 which are published in [38].

Reactions 70 – 74. The rates for the reverse of reactions 55 – 59 are taken from Edwards et al. [38].

Reactions 75 – 79. The rate coefficients for the reaction R-OH + H → R-O• + H_2 were taken from the calculations performed by Meana-Paneda et al. [58] for the reaction CH_3OH + H → CH_3O + H_2.

Reactions 80 – 84. The rate coefficients for the reverse of reactions 75 – 79 were found by taking the forward rate for the reaction CH_3OH + H → CH_3O + H_2 calculated in [58] and multiplying it by the equilibrium constants calculated by Jodkowski et al. [59].

Reactions 85 – 89. The rate of H addition to produce H_2O and form a radical site is taken from shock tube measurements of the thermal decomposition of methanol performed by Hidaka et al. [60].

Reaction 90. The calculation for the rate of oxidation of a five-member ring by O_2 is discussed in Chapter 4. The high-pressure-limit rate is used in the KMC model.

Reaction 91. The rate coefficient for hydrogen abstraction by O_2 utilizes the per-site rate coefficient for the reaction of benzene + O_2 → phenyl + HO_2 determined in shock tube experiments performed by Asaba and Fujii [61].

Reaction 92. The rate coefficient for hydrogen abstraction by OH is the per-site rate coefficient of benzene + OH → phenyl + H_2O as determined by Seta et al. [62].

Reactions 93, 94, and 95. The rate coefficient for R-H + O → R-O• + H is the per-site rate coefficient for benzene + O → phenoxy + H from a study by Leidreiter and Wagner [63].

Reactions 96 – 99. The rate coefficient for six-member ring oxidation by OH was calculated to be 1×10^{14} cm^3 mol^{-1} s^{-1} in the high-pressure limit in [38].

Reactions 100 – 103. The rate coefficient for six-member ring oxidation by H_2O was estimated to be 1×10^{12} cm^3 mol^{-1} s^{-1} in the high-pressure limit based on the results of a mechanistic study by Dong et al. [64].

Reaction 104. The calculations for the rate coefficient for five-member ring oxidation by O in the high-pressure limit is discussed in Chapter 6.

3 Oxidation of Graphene-Edge Six-Member Rings by Molecular Oxygen

The first step towards building a detailed oxidation model was to calculate the rate coefficients for key elementary oxidation reactions. This chapter presents theoretical calculations of the product branching fractions and rate coefficients for the oxidation of graphene-edge six-member rings by molecular oxygen. These elementary reactions and their corresponding rate coefficients were incorporated into the KMC surface oxidation model.

3.1 Introduction

The reactions of aromatic radicals with molecular oxygen play an important role in combustion of hydrocarbon fuels. The oxidation reactions occur simultaneously with the growth of polycyclic aromatic hydrocarbons (PAHs), and the processes compete to effectively determine the amount of soot produced in combustion. Also, oxidation generates energy which can further growth processes [12].

Oxidation of six-member aromatic rings with molecular oxygen have been previously studied both experimentally and theoretically in small molecules (phenyl radical) and prototype PAH systems (naphthyl radicals). Experimentally, rate coefficients for the phenyl + O_2 reaction have been measured in two relatively low temperature ranges of 297–473 [23] and 418–815 [65] K and computed using the canonical variational transition state theory in conjunction with a density functional potential [66]. At low temperatures, the peroxy radical C_6H_5OO formed via the addition/stabilization mechanism was determined the major product [23], whereas at temperatures above 1000 K the reaction was inferred to produce phenoxy radical, C_6H_5O + O, with possible minor contributions from o- and p-benzoquinone, o/p-$C_6H_4O_2$, plus atomic hydrogen [67]. Phenoxy radical can undergo unimolecular decomposition to the cyclopentadienyl radical + CO [23, 68] and thus the oxidation with O_2 essentially converts the six-member ring of phenyl to a five-member ring. The only products of the C_6H_5 + O_2 reaction observed in crossed molecular beam experiments under single-collision conditions at collision energies of 5–26 kcal/mol were C_6H_5O + O [69-71]. However, the most recent experimental study of the reaction in a combustion-simulating chemical reactor at 873 and 1003 K with product identification by tunable VUV photoionization gave the phenoxy radical, cyclopentadienyl, and ortho-benzoquinone as major primary products, whereas secondary products included para-benzoquinone, phenol, cyclopentadiene, 2,4-cyclopentadienone, vinylacetylene, and acetylene [72]. 2,4-cyclopentadienone, C_5H_4O, was suggested to originate from fragmentation of another hypothetical primary product, pyranyl radical C_5H_5O, which was not detected because apparently it was unstable under the experimental conditions.

The oxidation kinetics of the naphthyl radical was studied by Marinov et al. [73], who estimated the rate coefficient of the 1-$C_{10}H_7$ + O_2 reaction in their kinetic modeling of a laminar premixed n-butane flame, and by Lin and co-workers [74], who reported thermal

rate coefficients for the 2-naphthyl + O_2 system at 299–444 K and concluded that at these low temperatures the reaction proceeds via the association-stabilization mechanism to the naphthyl peroxy radical $C_{10}H_7OO$, which may then lose the oxygen atom yielding the naphthoxy radical, $C_{10}H_7O$.

Mebel and co-workers reported extensive *ab initio* studies of the potential energy surfaces (PESs) for the $C_6H_5 + O_2$ and $C_{10}H_7 + O_2$ reactions [31, 75]. According to their study, the most energetically favorable reaction channels are those leading to the formation of five-member rings together with CO+O or CO_2. However, the PES by itself is not sufficient to predict reaction rate coefficients and product branching ratios at temperatures and pressures relevant to combustion. I partnered with Mebel and co-workers to utilize the results of their quantum chemistry calculations to perform RRKM-master equation (RRKM-ME) computations to determine temperature- and pressure-dependent rate coefficients and product branching ratios for these reactions. The results of these calculations are presented in this chapter.

3.2 Prototype Reactions

Phenyl, 1-naphthyl, 2-naphthyl, and pyrenyl were selected as prototypes of single and multi-ring aromatic radicals. The structures are shown in Figure 3.1. These four prototype molecules were chosen to see how the size of the molecule and position of the radical site might affect the relative product yields.

Phenyl   1-naphthyl   2-naphthyl   Pyrenyl
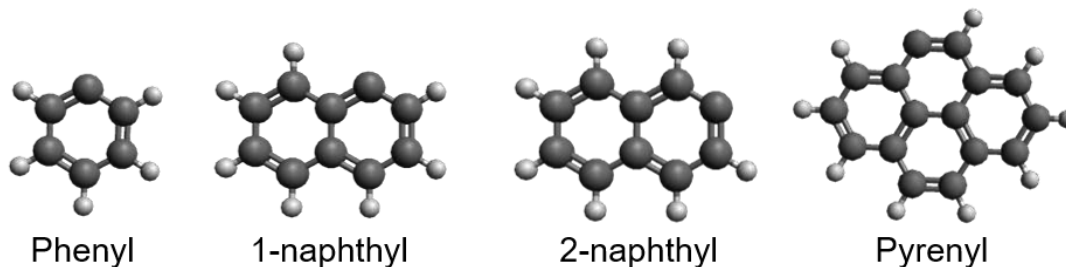
Figure 3.1. Structures of aromatic radicals.

3.3 Potential Energy Surfaces

This section will briefly discuss the quantum chemistry calculations performed by Mebel and co-workers and will present the potential energy diagrams from their work that were used as inputs into the rate coefficient calculations.

For the phenyl + O_2 reaction, Mebel and co-workers optimized the geometries and computed vibrational frequencies of all of the species involved in the reaction at the hybrid density functional B3LYP/6-311++G** level of theory. The relative energies of the species were refined by single-point calculations using the modified Gaussian 2 G2M(MP2) method. The resulting potential energy diagram for the phenyl + O_2 reaction (Figure 8

from [31]) is presented in Figure 3.2. The reaction begins with the barrierless addition of molecular oxygen to the radical site to form phenyl peroxy $C_6H_5O_2$, which can dissociate into the following products: phenoxy radical $C_6H_5O + O$, pyranyl $C_5OH_5 + CO$, $C_5H_5 + CO_2$, and 1,2-benzoquinone $C_6H_4O_2 + H$. The phenoxy radical, due to its chemical activation, can further dissociate to cyclopentadienyl $C_5H_5 + CO$. More detailed descriptions of the calculations and discussions of reaction pathways are presented in Tokmakov et al. [31].
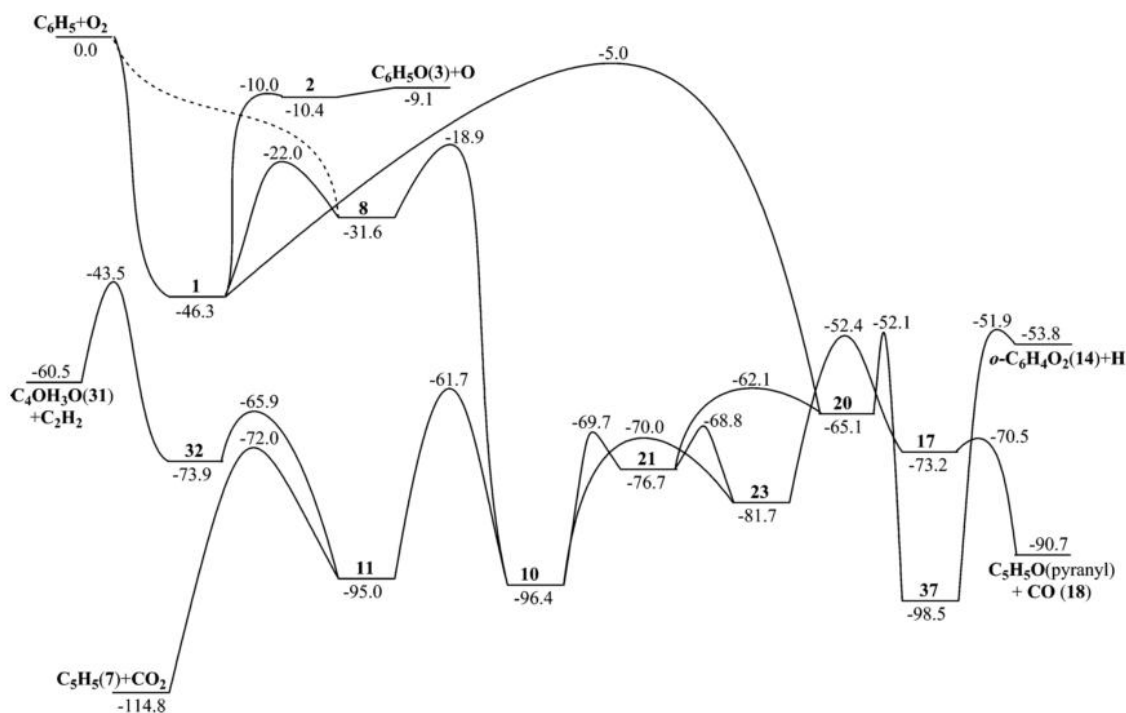
Figure 3.2. Potential energy diagram for the phenyl + O_2 reaction, taken from [31]. Relative energies are given in kcal/mol as calculated at the G2M level.

The PESs of the 1-naphthyl + O_2 and 2-naphthyl + O_2 reactions were studied at the G3(MP2,CC)//B3LYP/6-311G** level of theory. The resulting potential energy diagrams were published in Zhou et al. [75], and are reproduced here in Figures 3.3 – 3.8. Similarly to the reaction of phenyl with molecular oxygen, barrierless addition of O_2 to form a naphthoxy radical $C_{10}H_7O$ is followed by decomposition to indenyl $C_9H_7 + CO$. As an alternative pathway, one of the oxygen atoms from the initial naphthyl peroxy adduct $C_{10}H_7O_2$ can be inserted into one of the six-member rings to form two fused six-member C_6 and seven-member C_6O rings. These intermediates can then decompose into indenyl + CO_2, benzonpyranyl $C_9OH_7 + CO$, and naphthoquinone $C_{10}H_6O_2 + H$. Further discussion about the other channels can be found in [75].
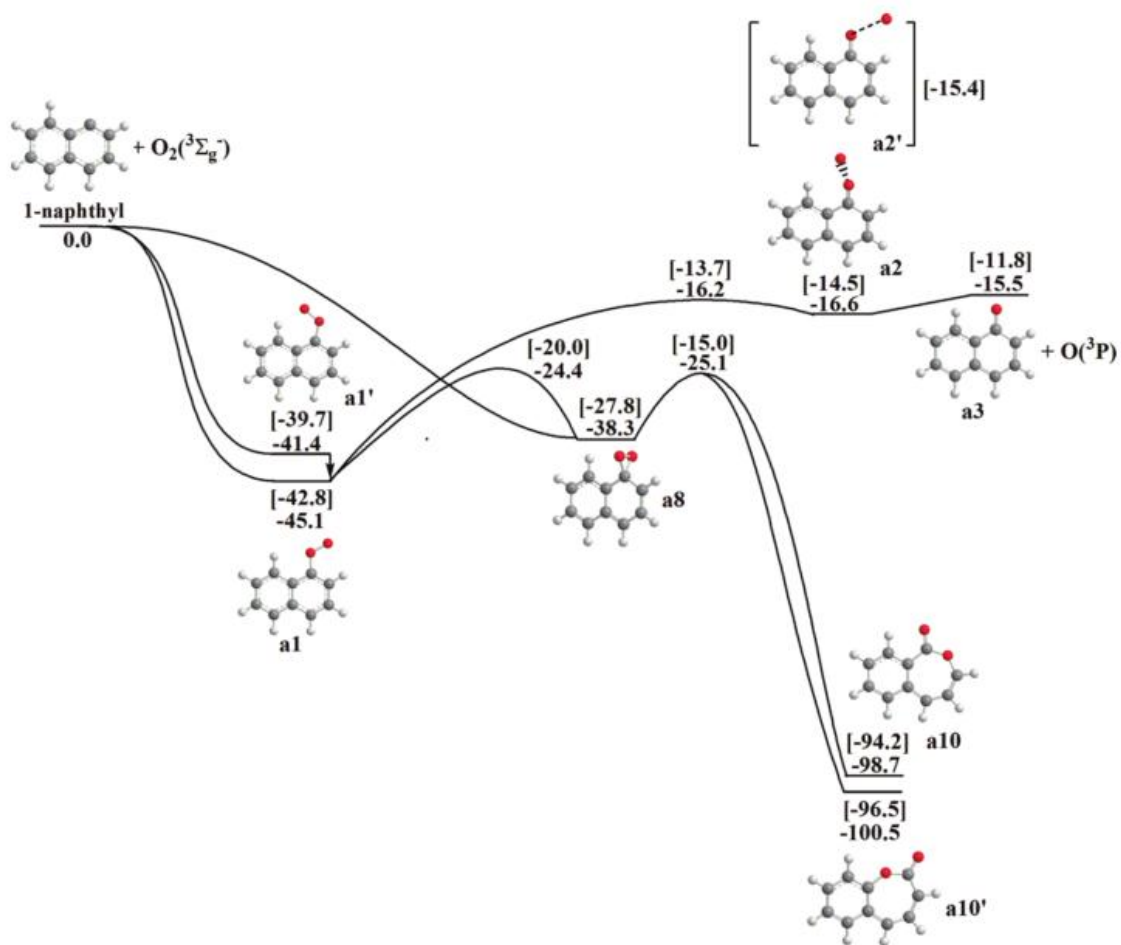
Figure 3.3. Potential energy diagram for the initial channels of the 1-naphthyl + O₂ reaction, taken from [75]. Relative energies are given in kcal/mol as calculated at the G3 and B3LYP/6-311G** + ZPE (in brackets) levels of theory.
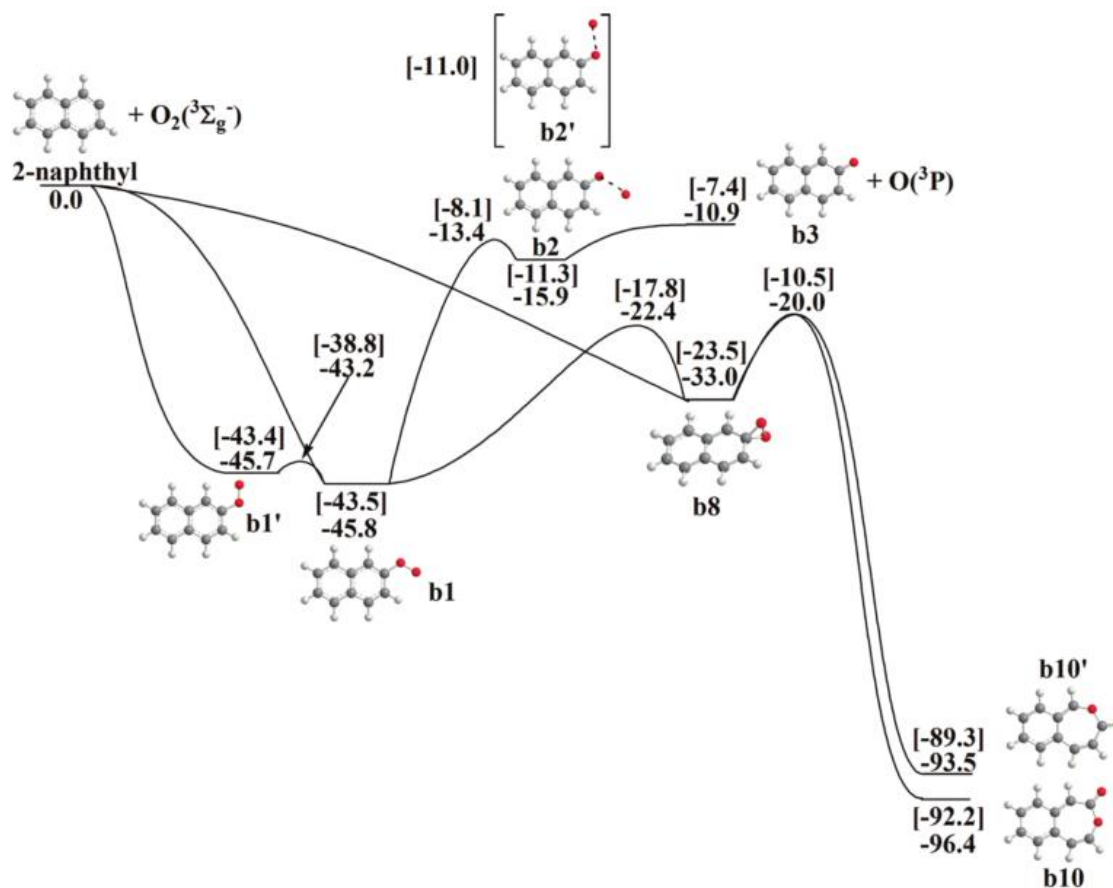
Figure 3.4. Potential energy diagram for the initial channels of the 2-naphthyl + O_2 reaction, taken from [75]. Relative energies are given in kcal/mol as calculated at the G3 and B3LYP/6-311G** + ZPE (in brackets) levels of theory.
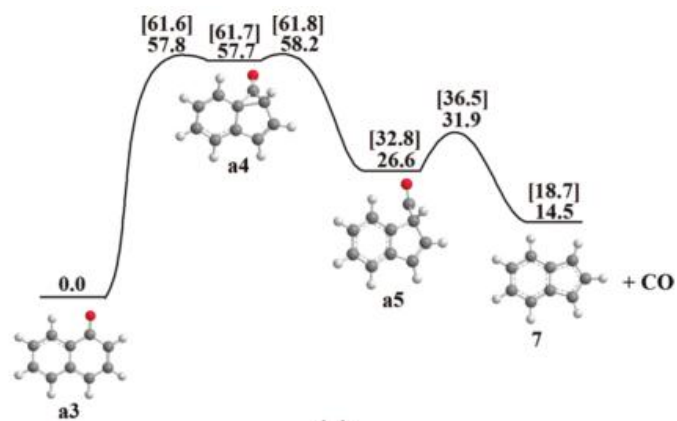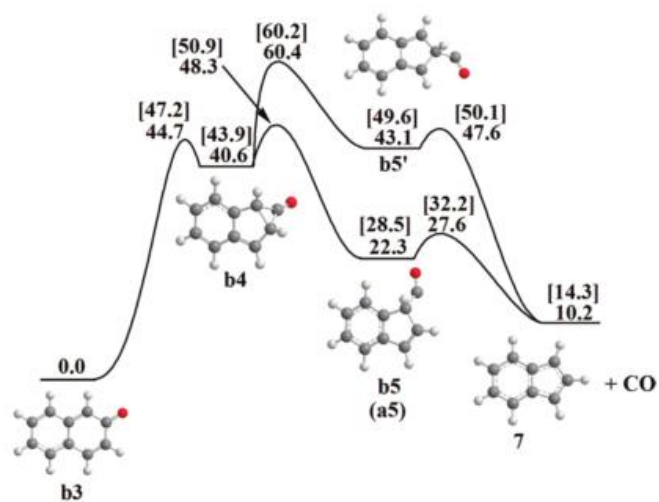
Figure 3.5. Potential energy diagram for the dissociation channels of (a) 1-naphthoxy and (b) 2-napthoxy radicals, taken from [75]. Relative energies are given in kcal/mol as calculated at the G3 and B3LYP/6-311G** + ZPE (in brackets) levels of theory.
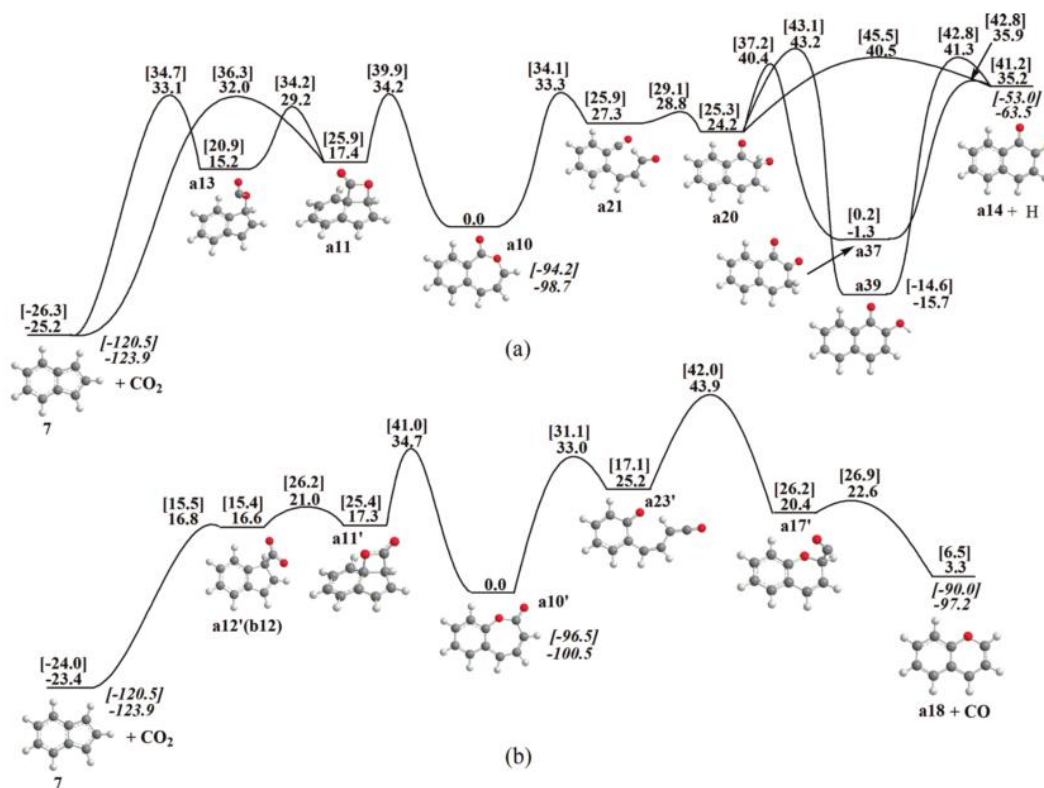
Figure 3.6. Potential energy diagram for the dissociation channels of the (a) **a10** and (b) **a10'** intermediates in the 1-naphthyl + O_2 reaction, taken from [75]. Relative energies are given in kcal/mol as calculated at the G3 and B3LYP/6-311G** + ZPE (in brackets) levels of theory.
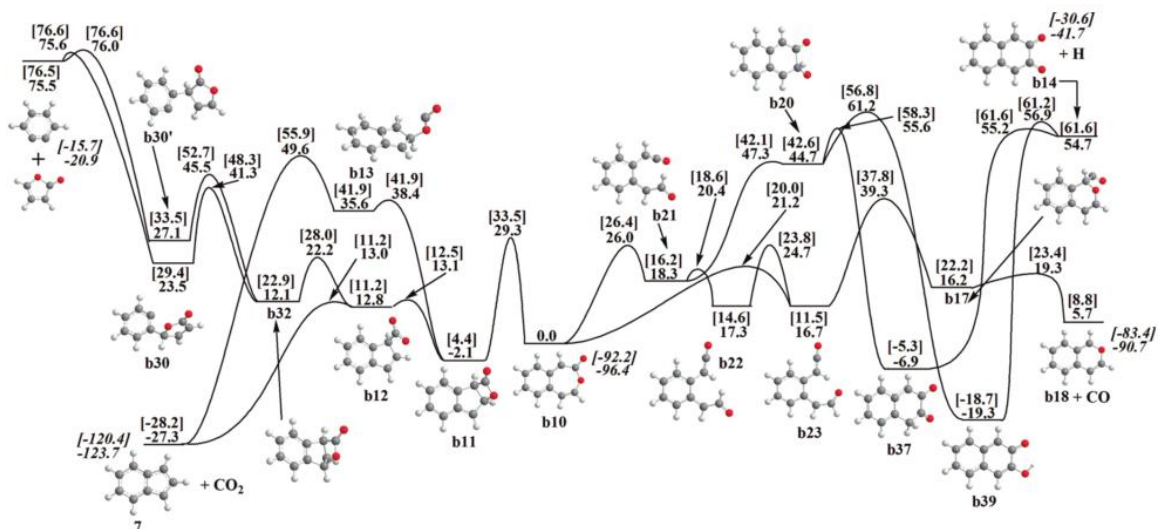
Figure 3.7. Potential energy diagram for the dissociation channels of the **b10** intermediate in the 2-naphthyl + O_2 reaction, taken from [75]. Relative energies are given in kcal/mol as calculated at the G3 and B3LYP/6-311G** + ZPE (in brackets) levels of theory.
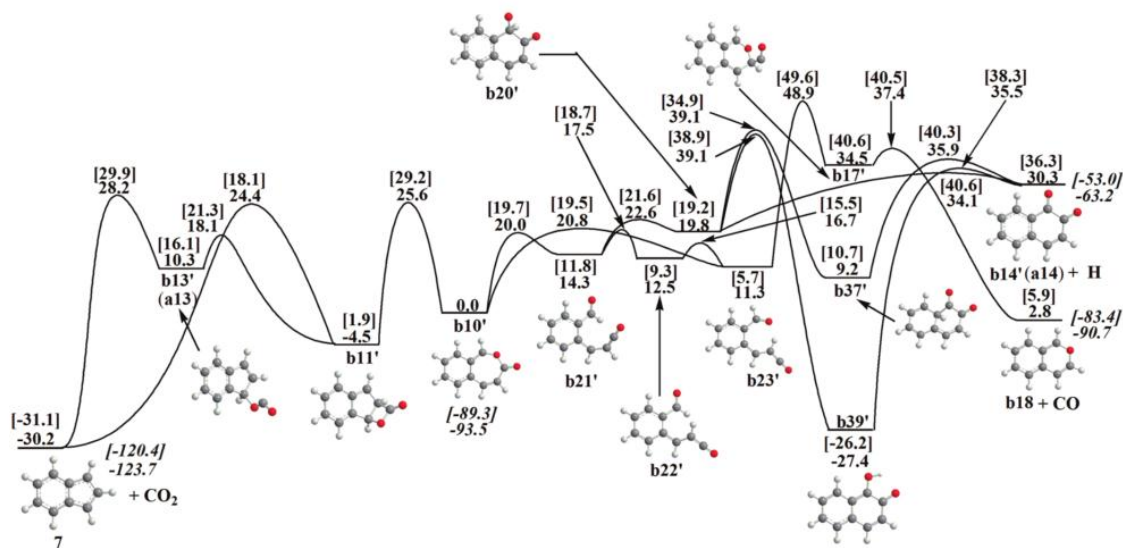
Figure 3.8. Potential energy diagram for the dissociation channels of the **b10'** intermediate in the 2-naphthyl + O_2 reaction, taken from [75]. Relative energies are given in kcal/mol as calculated at the G3 and B3LYP/6-311G** + ZPE (in brackets) levels of theory.

Mebel also examined the energetics of the pyrenyl + O_2 reaction at the G3 level of theory. G3(MP2,CC)//B3LYP/6-311G**. The potential energy diagram is shown in Figure 3.9. The only channel that was considered was the one in which atomic oxygen was eliminated and the subsequent unimolecular decomposition of the remaining oxypyrenyl radical. These quantum-chemical calculations were performed after the RRKM-ME calculations for the phenyl and naphthyl systems were done. The results in the ensuing section will show that the single channel considered for the pyrenyl system was the only dominant channel at temperatures relevant to combustion (1500 – 2500 K).
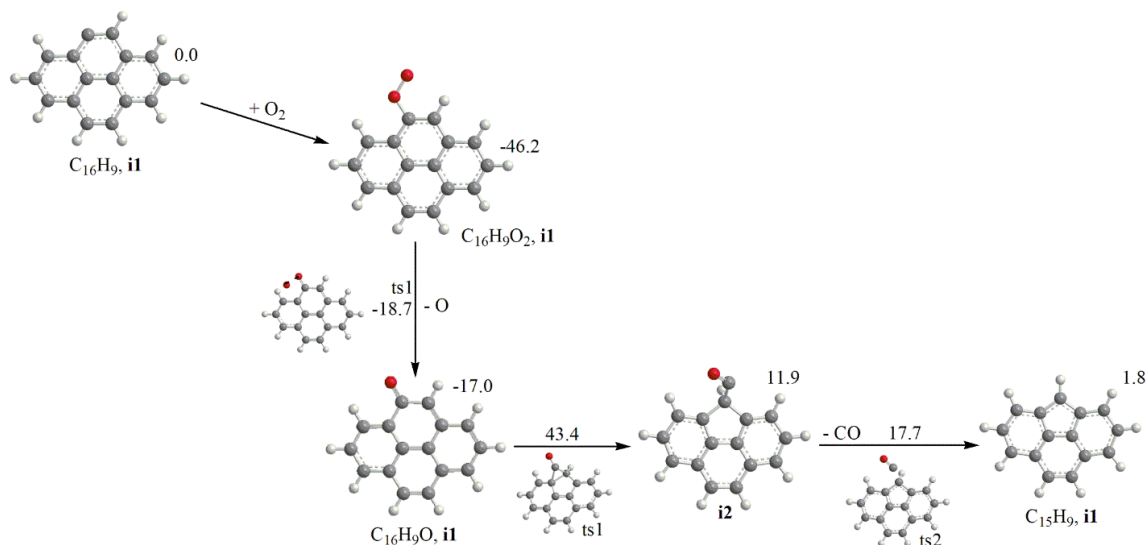
Figure 3.9. Potential energy diagram for the pyrenyl + O_2 reaction. Relative energies are given in kcal/mol as calculated at the G3 level.

3.4 Reaction Rate Coefficients

3.4.1 Entrance Channel Reaction Rate Coefficients

VRC-TST calculations of thermal rate coefficients for the barrierless phenyl + O_2, naphthyl + O_2, and pyrenyl + O_2 association channels were performed using VariFlex [47, 48]. One of the key inputs into the VRC-TST calculations is the potential along the minimal energy reaction path (MEP), i.e., the stretching potential (as it is called in the VariFlex user manual). Kislov et al. [76] computed the stretching potential for the addition of O_2 to phenyl by performing single-point energy calculations at the multi-reference second-order perturbation-theory CASPT2(19,14)/aug-cc-pVDZ level. For the larger naphthyl + O_2 and pyrenyl + O_2 systems, the CASPT2(19,14) potential for phenyl + O_2 was scaled to reproduce the accurate $C_{10}H_7$–O_2 and $C_{16}H_9$–O_2 bond dissociation energies. The computed stretching potentials for VariFlex calculations were provided in a tabulated form and then interpolated by a VariFlex built-in procedure.

The pyrenyl + O_2 VariFlex calculations encountered an additional complication. Due to an artificial restriction in the VariFlex program, the reaction rate could not be variationally calculated for bond lengths shorter than the distance from the center of mass for each fragment to the bonding point. This limitation is a problem for pyrenyl which is relatively large. For example, the distance from the center of mass of $C_{16}H_9$ radical to the bonding oxygen atom is 3.0 Å. This means that if the true reaction rate minimum occurs for a bond length lower than 3.0 Å, then the calculated rate constant will be over-estimated. To correct this, a smaller molecule (phenyl) was chosen as a surrogate of the larger one for the barrierless reactions. The bond dissociation energies, potentials, number of electronic states, and symmetry numbers for the surrogate reaction were altered to match the corresponding values of the actual reaction. For the $C_{16}H_9 + O_2$ reaction, the true minimum

reaction rate occurred at a bonding distance of 2.05 Å. Figure 3.10 illustrates the surrogate reaction technique used for the VRC calculations. Tables 3.1 and 3.2 show the canonical rates for the surrogate and original reactions, respectively.
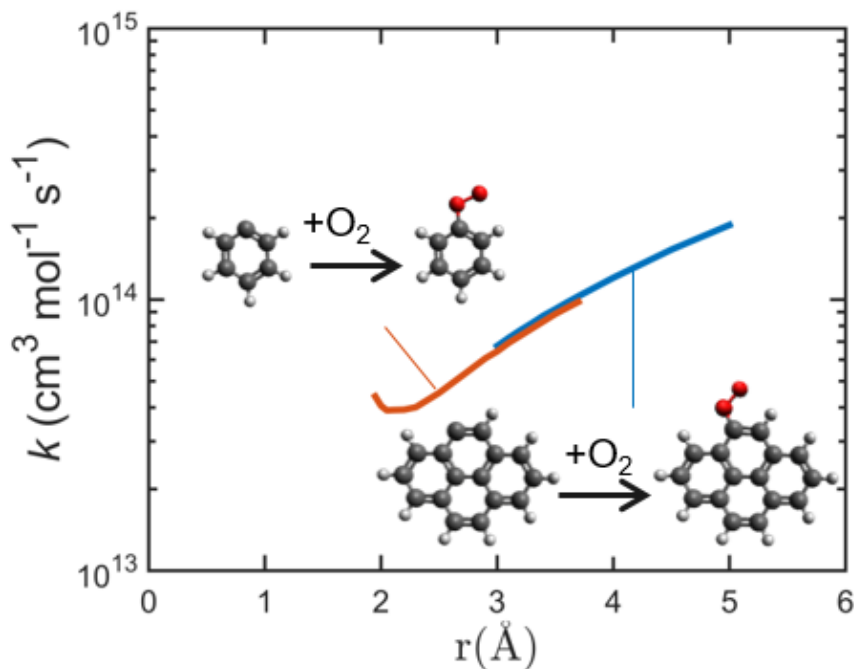
Figure 3.10. Canonical reaction rates for pyrenyl + O_2 → oxypyrenyl and phenyl + O_2 → phenyl peroxy at $T = 2500$ K at the high-pressure limit as a function of bond length.

Table 3.1. Canonical rates for phenyl + O_2 → phenyl peroxy at $T = 2500$ K at the high-pressure limit as a function of bond length.

r (Å)	k (cm^3 mol^{-1} s^{-1})
1.95	4.39E+13
2.00	4.06E+13
2.05	3.90E+13
2.10	3.91E+13
2.15	3.92E+13
2.20	3.93E+13
2.30	4.00E+13
2.50	4.52E+13
2.70	5.24E+13
2.90	6.08E+13
3.00	6.44E+13

3.10	6.92E+13
3.30	7.83E+13
3.50	8.84E+13
3.70	9.81E+13

Table 3.2. Canonical rates for pyrenyl + $O_2 \rightarrow$ oxypyrenyl at T = 2500 K at the high-pressure limit as a function of bond length.

r (Å)	k (cm^3 mol^{-1} s^{-1})
3.00	6.74E+13
3.10	7.22E+13
3.20	7.71E+13
3.30	8.19E+13
3.40	8.73E+13
3.50	9.21E+13
3.60	9.75E+13
3.70	1.03E+14
4.00	1.20E+14
4.50	1.52E+14
5.00	1.88E+14

Next, the microcanonical rates for the surrogate reactions were calculated for the full range and for the restricted range of bonding distances. The ratio needed to correct the restricted range values was then calculated to be 0.58. This correction factor was then applied to the microcanonical rates of the original system.

3.4.2 Overall Thermal Rate Coefficients

The microcanonical rate coefficients from the VRC-TST calculations presented in the previous section were used as inputs for the RRKM-ME computations. Before calculating rate coefficients and product branching ratios at combustion temperatures, it was necessary to compare the computed overall phenyl + $O_2 \rightarrow$ products rate coefficients with the available experimental data. The goal of my calculations was to generate reliable rate coefficients for combustion temperatures, so I focused my comparison on the higher-temperature data set reported by Schaugg and co-workers for the 418−815 K temperature range and p = 0.7 mbar measured using a fast flow reactor technique [65]. As seen in Figure 3.11, the VRC-TST/RRKM-ME calculations closely reproduce Schaugg's

experiment. The difference between the calculated and measured rate coefficients is within a factor of 1.4−2.0 at higher temperatures (656−815 K) and slightly increases to a factor of 3.0 at 418 K. The calculated rate coefficients show positive temperature dependence, which is consistent with the experiment; the fitted Arrhenius expression gives the activation energy of 1.9 kcal/mol, only slightly higher than the apparent activation energy of 0.6 kcal/mol observed in experiment. The agreement between the theoretical and experimental activation energies is even better within the higher temperature 724–815 K range, where the measured rate coefficients exhibit strong Arrhenius-like behavior with E_a = 2.2 kcal/mol.
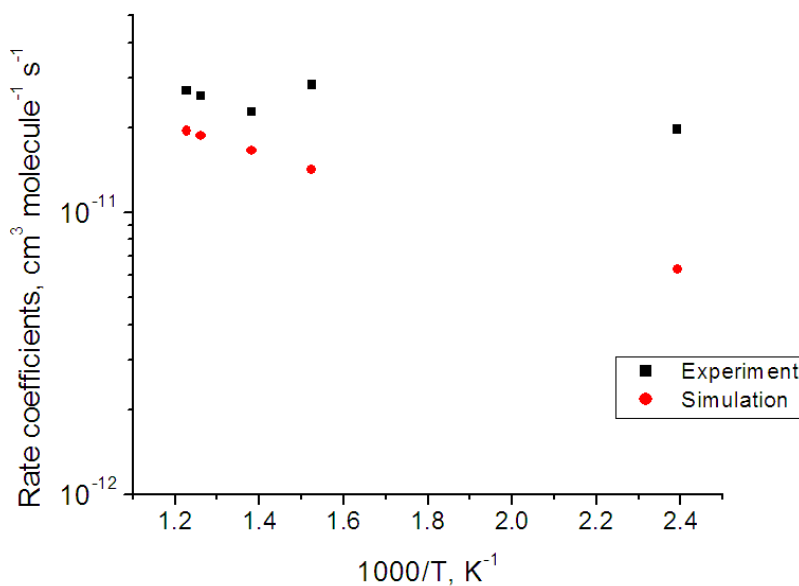
Figure 3.11. Comparison of the calculated total rate coefficients of the phenyl + O_2 reaction with experimental data at 415 – 815 K (from [65]).

One can expect that the theoretical rate coefficients calculated at temperatures relevant to combustion should be accurate within 40% or better as the agreement between experiment and theoretical predictions improves with temperature. Meanwhile, the larger deviation observed at low temperatures ($T = 418$ K) may be attributed to the fact that computed rate coefficients are much more sensitive to inaccuracies in the stretching potential and in the theoretical approach in general, the factors which affect theoretical rate coefficients more significantly at lower temperatures than at high temperatures. Interestingly, the low-temperature kinetic measurements reported by Yu and Lin [23] for the 297−473 K temperature range and pressures of 20−80 Torr show a negative activation energy of -0.32 kcal/mol, although in the temperature range where the two experimental data sets overlap, 418−473 K, the rate coefficients obtained by Yu and Lin are in close agreement with those measured by Schaugg et al. as seen in Figure 3.12.
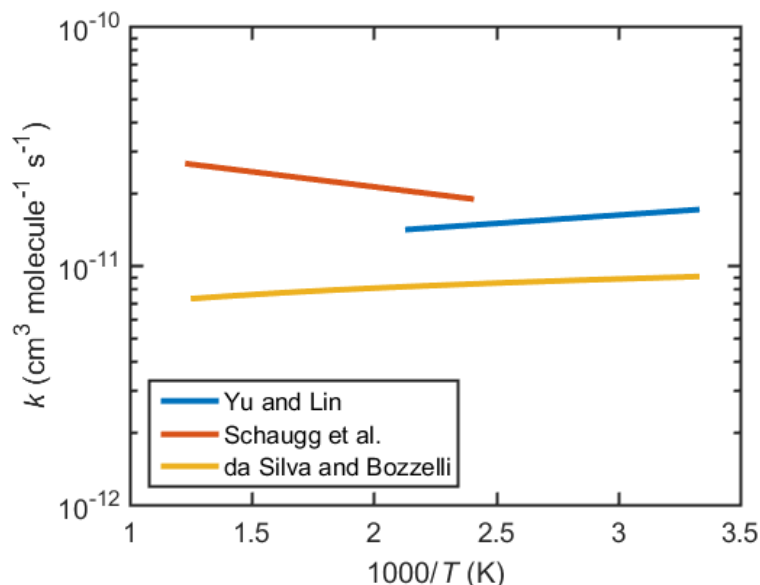
Figure 3.12. Comparison between rates from the literature [23, 65, 66] for the association of phenyl + O_2.

The available experimental data suggest that the rate coefficient has a minimum at around 400 K. Such a behavior can be explained by the fact that the bimolecular rate coefficient is proportional to $\exp(\Delta S^\#/R) \times T^2 \times \exp(-\Delta H^\#/RT)$ and even though the reaction is barrierless and thus has a negative $\Delta H^\#$, as the temperature rises, the decrease of $\exp(-\Delta H^\#/RT)$ appears to be slower than the increase of T^2 in the pre-exponential factor. Noteworthy is that the calculations presented here correctly reproduced the positive temperature dependence of the rate coefficient at higher temperatures, whereas the earlier calculations by da Silva and Bozzelli [66] did not.

Rate coefficients for the phenyl + O_2, 1- and 2-naphthyl + O_2, and pyrenyl + O_2 reactions computed at combustion-relevant temperatures of 1500−2500 K are collected in Table 3.3. Since the total rate coefficients are practically pressure-independent, only the values computed at 1 atm are presented in Table 3.3. The results demonstrate that all of the rate are close to each other at the same temperatures, with differences not exceeding 30 %.

Table 3.3. Total bimolecular rate coefficients of product formation (in cm^3 molecule^{-1} s^{-1}) calculated at different temperatures and P = 1 atm.

T, K	phenyl + O_2	1-naphthyl + O_2	2-naphthyl + O_2	pyrenyl + O_2
1500	2.96×10^{-11}	3.08×10^{-11}	3.53×10^{-11}	2.72×10^{-11}
2000	3.46×10^{-11}	3.81×10^{-11}	4.58×10^{-11}	3.97×10^{-11}
2500	4.16×10^{-11}	4.20×10^{-11}	5.49×10^{-11}	5.20×10^{-11}

3.4.3 Product Branching Ratios and Individual Rate Coefficients for Product Formation

MultiWell simulations were performed for the phenyl + O_2 and naphthyl + O_2 systems first in order to gain insight into the dominant pathways for these reactions. The RRKM-ME calculations for the pyrenyl + O_2 reaction were performed later with only one product formation channel, so the discussion of product branching ratios will only include results from phenyl and naphthyl. The following tables show calculated rate coefficients of the formation of all individual products in the phenyl + O_2, 1-naphthyl + O_2, and 2-naphthyl + O_2 reactions at the temperatures of 1500, 2000, and 2500 K and pressures of 0.01, 0.10, 1, and 10 atm (Tables 3.4 – 3.18), product branching ratios (Tables 3.19 – 3.30), and high-pressure rate coefficients of the elementary unimolecular reaction steps (Tables 3.31 – 3.33).

Table 3.4. Rate coefficient (in cm^3 s^{-1}) of the reaction $C_6H_5 + O_2 \rightarrow C_6H_5O + O$.

	P (atm)			
T (K)	0.01	0.1	1	10
1500	1.7E-11	2.0E-11	2.3E-11	2.4E-11
2000	6.1E-12	9.0E-12	1.4E-11	2.2E-11
2500	1.3E-12	3.0E-12	8.4E-12	1.5E-11

Table 3.5. Rate coefficient (in cm^3 s^{-1}) of the reaction $C_6H_5 + O_2 \rightarrow C_5H_5 + CO + O$.

	P (atm)			
T (K)	0.01	0.1	1	10
1500	7.1E-12	4.4E-12	1.7E-12	4.1E-13
2000	2.6E-11	2.3E-11	1.8E-11	1.1E-11
2500	3.9E-11	3.7E-11	3.2E-11	2.5E-11

Table 3.6. Rate coefficient (in cm^3 s^{-1}) of the reaction $C_6H_5 + O_2 \rightarrow C_5H_5 + CO_2$.

T (K)	k (cm^3/s)
1500	1.5E-12
2000	5.6E-13
2500	2.3E-13

Table 3.7. Rate coefficient (in cm^3 s^{-1}) of the reaction $C_6H_5 + O_2 \rightarrow C_5H_5O + CO$.

T (K)	k (cm^3/s)
1500	2.8E-12
2000	1.5E-12
2500	8.3E-13

Table 3.8. Rate coefficient (in cm^3 s^{-1}) of the reaction $C_6H_5 + O_2 \rightarrow o\text{-}C_6H_4O_2 + H$.

T (K)	k (cm^3/s)
1500	6.1E-13
2000	3.1E-13
2500	1.6E-13

Table 3.9. Rate coefficient (in cm^3 s^{-1}) of the reaction $1\text{-}C_{10}H_7 + O_2 \rightarrow 1\text{-}C_{10}H_7O + O$.

T (K)	P (atm)			
	0.01	0.1	1	10
1500	1.1E-11	1.3E-11	1.5E-11	1.6E-11
2000	3.6E-12	7.3E-12	1.4E-11	2.1E-11
2500	4.3E-13	2.3E-12	7.1E-12	1.8E-11

Table 3.10. Rate coefficient (in cm^3 s^{-1}) of the reaction $1\text{-}C_{10}H_7 + O_2 \rightarrow C_9H_7 + CO + O$.

T (K)	P (atm)			
	0.01	0.1	1	10
1500	4.7E-12	2.4E-12	6.7E-13	1.6E-13
2000	2.2E-11	1.8E-11	1.1E-11	4.5E-12
2500	3.2E-11	3.0E-11	2.5E-11	1.4E-11

Table 3.11. Rate coefficient (in cm^3 s^{-1}) of the reaction 1-C$_{10}$H$_7$ + O$_2$ → C$_9$H$_7$ + CO$_2$.

T (K)	k (cm^3/s)
1500	3.5E-12
2000	2.2E-12
2500	1.4E-12

Table 3.12. Rate coefficient (in cm^3 s^{-1}) of the reaction 1-C$_{10}$H$_7$ + O$_2$ → 1-C$_9$H$_7$O + CO.

T (K)	k (cm^3/s)
1500	7.3E-12
2000	6.8E-12
2500	5.4E-12

Table 3.13. Rate coefficient (in cm^3 s^{-1}) of the reaction 1-C$_{10}$H$_7$ + O$_2$ → C$_{10}$H$_6$O$_2$ + H.

T (K)	k (cm^3/s)
1500	4.3E-12
2000	3.8E-12
2500	2.9E-12

Table 3.14. Rate coefficient (in cm^3 s^{-1}) of the reaction 2-C$_{10}$H$_7$ + O$_2$ → 2-C$_{10}$H$_7$O + O.

T (K)	P (atm)			
	0.01	0.1	1	10
1500	5.3E-12	1.1E-11	1.7E-11	2.2E-11
2000	2.7E-13	1.1E-12	4.7E-12	1.2E-11
2500	1.7E-14	1.1E-13	1.1E-12	5.8E-12

Table 3.15. Rate coefficient (in cm^3 s^{-1}) of the reaction 2-C$_{10}$H$_7$ + O$_2$ → C$_9$H$_7$ + CO + O.

T (K)	P (atm)			
	0.01	0.1	1	10
1500	2.3E-11	1.8E-11	1.1E-11	6.1E-12
2000	4.1E-11	4.0E-11	3.7E-11	3.0E-11
2500	5.2E-11	5.2E-11	5.1E-11	4.6E-11

Table 3.16. Rate coefficient (in cm^3 s^{-1}) of the reaction 2-C$_{10}$H$_7$ + O$_2$ → C$_9$H$_7$ + CO$_2$.

T (K)	k (cm^3/s)
1500	2.4E-12
2000	1.2E-12
2500	6.1E-13

Table 3.17. Rate coefficient (in cm^3 s^{-1}) of the reaction 2-C$_{10}$H$_7$ + O$_2$ → 2-C$_9$H$_7$O + CO.

T (K)	k (cm^3/s)
1500	2.2E-12
2000	1.5E-12
2500	9.9E-13

Table 3.18. Rate coefficient (in cm^3 s^{-1}) of the reaction 2-C$_{10}$H$_7$ + O$_2$ → C$_{10}$H$_6$O$_2$ + H.

T (K)	k (cm^3/s)
1500	2.2E-12
2000	1.6E-12
2500	1.1E-12

Table 3.19. Product branching ratios of the association of $C_6H_5 + O_2$ at 0.01 atm.

T (K)	Product Branching Ratio				
	$C_6H_5O + O$	$C_5H_5 + CO + O$	$C_5H_5 + CO_2$	$C_5H_5O + CO$	$C_6H_4O_2 + H$
1500	0.59	0.24	0.05	0.02	0.10
2000	0.18	0.76	0.02	0.01	0.04
2500	0.03	0.94	0.01	0.00	0.02

Table 3.20. Product branching ratios of the association of $C_6H_5 + O_2$ at 0.1 atm.

T (K)	Product Branching Ratio				
	$C_6H_5O + O$	$C_5H_5 + CO + O$	$C_5H_5 + CO_2$	$C_5H_5O + CO$	$C_6H_4O_2 + H$
1500	0.68	0.15	0.05	0.02	0.10
2000	0.26	0.67	0.02	0.01	0.04
2500	0.07	0.90	0.01	0.00	0.02

Table 3.21. Product branching ratios of the association of $C_6H_5 + O_2$ at 1 atm.

T (K)	Product Branching Ratio				
	$C_6H_5O + O$	$C_5H_5 + CO + O$	$C_5H_5 + CO_2$	$C_5H_5O + CO$	$C_6H_4O_2 + H$
1500	0.77	0.06	0.05	0.02	0.10
2000	0.40	0.53	0.02	0.01	0.04
2500	0.20	0.77	0.01	0.00	0.02

Table 3.22. Product branching ratios of the association of $C_6H_5 + O_2$ at 10 atm.

T (K)	Product Branching Ratio				
	$C_6H_5O + O$	$C_5H_5 + CO + O$	$C_5H_5 + CO_2$	$C_5H_5O + CO$	$C_6H_4O_2 + H$
1500	0.81	0.01	0.05	0.02	0.10
2000	0.62	0.31	0.02	0.01	0.04
2500	0.36	0.61	0.01	0.00	0.02

Table 3.23. Product branching ratios of the association of 1-$C_{10}H_7$ + O_2 at 0.01 atm.

T (K)	Product Branching Ratio				
	1-$C_{10}H_7O$ + O	C_9H_7 + CO + O	C_9H_7 + CO_2	C_9H_7O + CO	$C_{10}H_6O_2$ + H
1500	0.36	0.15	0.11	0.24	0.14
2000	0.09	0.57	0.06	0.18	0.10
2500	0.01	0.76	0.03	0.13	0.07

Table 3.24. Product branching ratios of the association of 1-$C_{10}H_7$ + O_2 at 0.1 atm.

T (K)	Product Branching Ratio				
	1-$C_{10}H_7O$ + O	C_9H_7 + CO + O	C_9H_7 + CO_2	C_9H_7O + CO	$C_{10}H_6O_2$ + H
1500	0.43	0.08	0.11	0.24	0.14
2000	0.19	0.47	0.06	0.18	0.10
2500	0.05	0.72	0.03	0.13	0.07

Table 3.25. Product branching ratios of the association of 1-$C_{10}H_7$ + O_2 at 1 atm.

T (K)	Product Branching Ratio				
	1-$C_{10}H_7O$ + O	C_9H_7 + CO + O	C_9H_7 + CO_2	C_9H_7O + CO	$C_{10}H_6O_2$ + H
1500	0.49	0.02	0.11	0.24	0.14
2000	0.38	0.28	0.06	0.18	0.10
2500	0.17	0.60	0.03	0.13	0.07

Table 3.26. Product branching ratios of the association of 1-$C_{10}H_7$ + O_2 at 10 atm.

T (K)	Product Branching Ratio				
	1-$C_{10}H_7O$ + O	C_9H_7 + CO + O	C_9H_7 + CO_2	C_9H_7O + CO	$C_{10}H_6O_2$ + H
1500	0.51	0.01	0.11	0.24	0.14
2000	0.55	0.12	0.06	0.18	0.10
2500	0.43	0.34	0.03	0.13	0.07

Table 3.27. Product branching ratios of the association of $2\text{-}C_{10}H_7 + O_2$ at 0.01 atm.

T (K)	Product Branching Ratio				
	$2\text{-}C_{10}H_7O$ + O	C_9H_7 + CO + O	C_9H_7 + CO_2	C_9H_7O + CO	$C_{10}H_6O_2$ + H
1500	0.15	0.66	0.07	0.06	0.06
2000	0.01	0.90	0.03	0.03	0.03
2500	0.00	0.95	0.01	0.02	0.02

Table 3.28. Product branching ratios of the association of $2\text{-}C_{10}H_7 + O_2$ at 0.1 atm.

T (K)	Product Branching Ratio				
	$2\text{-}C_{10}H_7O$ + O	C_9H_7 + CO + O	C_9H_7 + CO_2	C_9H_7O + CO	$C_{10}H_6O_2$ + H
1500	0.31	0.50	0.07	0.06	0.06
2000	0.02	0.88	0.03	0.03	0.03
2500	0.00	0.95	0.01	0.02	0.02

Table 3.29. Product branching ratios of the association of $2\text{-}C_{10}H_7 + O_2$ at 1 atm.

T (K)	Product Branching Ratio				
	$2\text{-}C_{10}H_7O$ + O	C_9H_7 + CO + O	C_9H_7 + CO_2	C_9H_7O + CO	$C_{10}H_6O_2$ + H
1500	0.49	0.32	0.07	0.06	0.06
2000	0.10	0.80	0.03	0.03	0.03
2500	0.02	0.93	0.01	0.02	0.02

Table 3.30. Product branching ratios of the association of $2\text{-}C_{10}H_7 + O_2$ at 10 atm.

T (K)	Product Branching Ratio				
	$2\text{-}C_{10}H_7O$ + O	C_9H_7 + CO + O	C_9H_7 + CO_2	C_9H_7O + CO	$C_{10}H_6O_2$ + H
1500	0.63	0.17	0.07	0.06	0.06
2000	0.26	0.64	0.03	0.03	0.03
2500	0.11	0.85	0.01	0.02	0.02

Table 3.31. High-pressure rate coefficients (in s^{-1}) of the elementary reactions in the $C_6H_5 + O_2$ reaction system.

Reaction	1500 K	2000 K	2500 K
$C_6H_5O_2$|i1 → $C_6H_5O_2$|i8	2.4E+09	2.1E+10	8.2E+10
$C_6H_5O_2$|i1 → C_6H_5O + O	7.2E+08	1.9E+10	1.4E+11
$C_6H_5O_2$|i1 → $C_6H_5O_2$|i20	4.6E+04	1.5E+06	1.2E+07
$C_6H_5O_2$|i1 → C_6H_5 + O_2	4.8E+08	2.2E+10	2.1E+11
$C_6H_5O_2$|i8 → $C_6H_5O_2$|i1	9.8E+11	2.3E+12	3.8E+12
$C_6H_5O_2$|i8 → C_6H_5 + O_2	1.8E+11	2.2E+12	9.4E+12
$C_6H_5O_2$|i8 → $C_6H_5O_2$|i10	1.1E+11	3.6E+11	7.1E+11
$C_6H_5O_2$|i10 → $C_6H_5O_2$|i8	5.6E+00	4.3E+03	2.3E+05
$C_6H_5O_2$|i10 → $C_6H_5O_2$|i11	6.1E+07	1.2E+09	7.2E+09
$C_6H_5O_2$|i10 → $C_6H_5O_2$|i21	1.5E+11	1.7E+12	7.5E+12
$C_6H_5O_2$|i10 → $C_6H_5O_2$|i23	9.3E+10	1.0E+12	4.5E+12
$C_6H_5O_2$|i11 → $C_6H_5O_2$|i10	4.0E+08	7.3E+09	4.2E+10
$C_6H_5O_2$|i11 → $C_6H_5O_2$|i32	5.3E+08	6.5E+09	2.9E+10
$C_6H_5O_2$|i11 → C_5H_5 + CO_2	9.5E+09	7.1E+10	2.4E+11
$C_6H_5O_2$|i17 → C_5H_5O + CO	9.2E+12	1.2E+13	1.5E+13
$C_6H_5O_2$|i17 → $C_6H_5O_2$|i23	2.4E+10	1.5E+11	4.7E+11
$C_6H_5O_2$|i20 → $C_6H_5O_2$|i1	1.4E+01	1.9E+03	3.5E+04
$C_6H_5O_2$|i20 → $C_6H_5O_2$|i37	8.2E+10	2.6E+11	5.3E+11
$C_6H_5O_2$|i20 → $C_6H_5O_2$|i21	4.1E+12	5.6E+12	6.8E+12
$C_6H_5O_2$|i21 → $C_6H_5O_2$|i10	1.3E+12	2.4E+12	3.6E+12
$C_6H_5O_2$|i21 → $C_6H_5O_2$|i20	2.4E+09	7.8E+09	1.6E+10
$C_6H_5O_2$|i21 → $C_6H_5O_2$|i23	6.0E+11	1.2E+12	1.9E+12
$C_6H_5O_2$|i23 → $C_6H_5O_2$|i10	8.0E+11	2.4E+12	4.6E+12
$C_6H_5O_2$|i23 → $C_6H_5O_2$|i21	6.0E+11	2.0E+12	4.0E+12
$C_6H_5O_2$|i23 → $C_6H_5O_2$|i17	3.0E+08	3.6E+09	1.6E+10
$C_6H_5O_2$|i32 → $C_6H_5O_2$|i11	1.4E+12	3.0E+12	4.6E+12
$C_6H_5O_2$|i32 → $C_4H_3O_2$ + C_2H_2	1.8E+11	3.1E+12	1.8E+13

Reaction	1500 K	2000 K	2500 K
$C_6H_5O_2|i37 \rightarrow C_6H_5O_2|i20$	9.4E+05	5.0E+07	5.6E+08
$C_6H_5O_2|i37 \rightarrow C_6H_4O_2 + H$	1.9E+07	1.3E+09	1.7E+10
$C_6H_5O|i3 \rightarrow C_6H_5O|i4$	5.1E+06	3.8E+08	5.1E+09
$C_6H_5O|i4 \rightarrow C_6H_5O|i3$	6.6E+11	1.2E+12	1.8E+12
$C_6H_5O|i4 \rightarrow C_6H_5O|i5$	2.3E+11	6.2E+11	1.1E+12
$C_6H_5O|i5 \rightarrow C_6H_5O|i4$	8.9E+08	6.3E+09	2.0E+10
$C_6H_5O|i5 \rightarrow C_5H_5 + CO$	1.0E+13	1.8E+13	2.5E+13

Table 3.32.   High-pressure rate coefficients (in s^{-1}) of the elementary reactions in the $1\text{-}C_{10}H_7 + O_2$ reaction system.

Reaction	1500 K	2000 K	2500 K
$1\text{-}C_{10}H_7O_2|i1 \rightarrow 1\text{-}C_{10}H_7 + O_2$	9.8E+08	4.0E+10	3.6E+11
$1\text{-}C_{10}H_7O_2|i1 \rightarrow 1\text{-}C_{10}H_7O_2|i1'$	3.3E+12	4.0E+12	4.7E+12
$1\text{-}C_{10}H_7O_2|i1 \rightarrow 1\text{-}C_{10}H_7O + O$	8.5E+09	1.2E+11	5.9E+11
$1\text{-}C_{10}H_7O_2|i1 \rightarrow 1\text{-}C_{10}H_7O_2|i8$	1.5E+10	1.0E+11	3.3E+11
$1\text{-}C_{10}H_7O_2|i1' \rightarrow 1\text{-}C_{10}H_7O_2|i1$	6.6E+12	5.6E+12	5.0E+12
$1\text{-}C_{10}H_7O|i3 \rightarrow 1\text{-}C_{10}H_7O|i4$	2.1E+05	3.2E+07	6.4E+08
$1\text{-}C_{10}H_7O|i4 \rightarrow 1\text{-}C_{10}H_7O|i3$	4.4E+12	4.5E+12	4.6E+12
$1\text{-}C_{10}H_7O|i4 \rightarrow 1\text{-}C_{10}H_7O|i5$	4.9E+12	5.2E+12	5.4E+12
$1\text{-}C_{10}H_7O|i5 \rightarrow 1\text{-}C_{10}H_7O|i4$	4.2E+07	6.4E+08	3.3E+09
$1\text{-}C_{10}H_7O|i5 \rightarrow C_9H_7 + CO$	4.9E+12	8.6E+12	1.2E+13
$1\text{-}C_{10}H_7O_2|i1' \rightarrow 1\text{-}C_{10}H_7 + O_2$	1.4E+10	3.1E+11	1.8E+12
$1\text{-}C_{10}H_7O_2|i8 \rightarrow 1\text{-}C_{10}H_7O_2|i1$	2.0E+11	6.6E+11	1.4E+12
$1\text{-}C_{10}H_7O_2|i8 \rightarrow 1\text{-}C_{10}H_7O_2|i10$	2.4E+11	7.7E+11	1.6E+12
$1\text{-}C_{10}H_7O_2|i8 \rightarrow 1\text{-}C_{10}H_7O_2|i10'$	4.8E+11	1.6E+12	3.1E+12
$1\text{-}C_{10}H_7O_2|i10 \rightarrow 1\text{-}C_{10}H_7O_2|i8$	6.5E+01	3.5E+04	1.5E+06
$1\text{-}C_{10}H_7O_2|i10 \rightarrow 1\text{-}C_{10}H_7O_2|i21$	6.3E+09	1.3E+11	7.8E+11
$1\text{-}C_{10}H_7O_2|i10 \rightarrow 1\text{-}C_{10}H_7O_2|i11$	3.4E+07	6.5E+08	3.8E+09
$1\text{-}C_{10}H_7O_2|i21 \rightarrow 1\text{-}C_{10}H_7O_2|i10$	1.2E+12	2.1E+12	2.9E+12
$1\text{-}C_{10}H_7O_2|i21 \rightarrow 1\text{-}C_{10}H_7O_2|i20$	2.0E+11	2.2E+11	2.3E+11
$1\text{-}C_{10}H_7O_2|i20 \rightarrow 1\text{-}C_{10}H_7O_2|i21$	3.4E+12	5.4E+12	7.1E+12

Reaction	1500 K	2000 K	2500 K
$1\text{-}C_{10}H_7O_2|i20 \rightarrow 1\text{-}C_{10}H_7O_2|i37$	3.1E+10	1.3E+11	3.2E+11
$1\text{-}C_{10}H_7O_2|i20 \rightarrow 1\text{-}C_{10}H_7O_2|i39$	1.4E+10	7.9E+10	2.2E+11
$1\text{-}C_{10}H_7O_2|i20 \rightarrow C_{10}H_6O_2 + H$	3.8E+11	2.0E+12	5.4E+12
$1\text{-}C_{10}H_7O_2|i37 \rightarrow 1\text{-}C_{10}H_7O_2|i20$	3.8E+06	1.4E+08	1.3E+09
$1\text{-}C_{10}H_7O_2|i37 \rightarrow C_{10}H_6O_2 + H$	2.5E+08	7.6E+09	6.0E+10
$1\text{-}C_{10}H_7O_2|i39 \rightarrow 1\text{-}C_{10}H_7O_2|i20$	6.8E+04	1.1E+07	2.4E+08
$1\text{-}C_{10}H_7O_2|i39 \rightarrow C_{10}H_6O_2 + H$	1.2E+06	1.9E+08	4.1E+09
$1\text{-}C_{10}H_7O_2|i11 \rightarrow 1\text{-}C_{10}H_7O_2|i10$	5.4E+10	2.4E+11	5.8E+11
$1\text{-}C_{10}H_7O_2|i11 \rightarrow 1\text{-}C_{10}H_7O_2|i13$	3.4E+11	9.6E+11	1.8E+12
$1\text{-}C_{10}H_7O_2|i11 \rightarrow C_9H_7 + CO_2$	1.8E+11	6.7E+11	1.5E+12
$1\text{-}C_{10}H_7O_2|i13 \rightarrow 1\text{-}C_{10}H_7O_2|i11$	1.3E+10	4.4E+10	9.2E+10
$1\text{-}C_{10}H_7O_2|i13 \rightarrow C_9H_7 + CO_2$	3.8E+10	1.9E+11	5.1E+11
$1\text{-}C_{10}H_7O_2|i10' \rightarrow 1\text{-}C_{10}H_7O_2|i8$	1.1E+01	6.4E+03	3.0E+05
$1\text{-}C_{10}H_7O_2|i10' \rightarrow 1\text{-}C_{10}H_7O_2|i23'$	6.2E+08	1.2E+10	7.1E+10
$1\text{-}C_{10}H_7O_2|i10' \rightarrow 1\text{-}C_{10}H_7O_2|i11'$	3.5E+06	6.8E+07	4.1E+08
$1\text{-}C_{10}H_7O_2|i23' \rightarrow 1\text{-}C_{10}H_7O_2|i10'$	1.7E+12	3.5E+12	5.4E+12
$1\text{-}C_{10}H_7O_2|i23' \rightarrow 1\text{-}C_{10}H_7O_2|i17'$	9.5E+09	4.7E+10	1.2E+11
$1\text{-}C_{10}H_7O_2|i17' \rightarrow 1\text{-}C_{10}H_7O_2|i23'$	1.3E+10	1.1E+11	3.7E+11
$1\text{-}C_{10}H_7O_2|i17' \rightarrow 1\text{-}C_9H_7O + CO$	1.3E+13	1.8E+13	2.1E+13
$1\text{-}C_{10}H_7O_2|i11' \rightarrow 1\text{-}C_{10}H_7O_2|i10'$	3.8E+10	1.8E+11	4.4E+11
$1\text{-}C_{10}H_7O_2|i11' \rightarrow 1\text{-}C_{10}H_7O_2|i12'$	3.3E+12	4.7E+12	5.8E+12
$1\text{-}C_{10}H_7O_2|i12' \rightarrow 1\text{-}C_{10}H_7O_2|i11'$	1.5E+11	2.2E+11	2.8E+11
$1\text{-}C_{10}H_7O_2|i12' \rightarrow C_9H_7 + CO_2$	4.3E+12	4.6E+12	4.9E+12

Table 3.33. High-pressure rate coefficients (in s^{-1}) of the elementary reactions in the $2\text{-}C_{10}H_7 + O_2$ reaction system.

Reaction	1500 K	2000 K	2500 K
$2\text{-}C_{10}H_7O_2|i1 \rightarrow 2\text{-}C_{10}H_7 + O_2$	1.0E+09	4.6E+10	4.3E+11
$2\text{-}C_{10}H_7O_2|i1 \rightarrow 2\text{-}C_{10}H_7O_2|i1'$	2.7E+12	3.6E+12	4.4E+12
$2\text{-}C_{10}H_7O_2|i1 \rightarrow 2\text{-}C_{10}H_7O + O$	8.9E+09	1.7E+11	9.9E+11
$2\text{-}C_{10}H_7O_2|i1 \rightarrow 2\text{-}C_{10}H_7O_2|i8$	7.2E+09	6.0E+10	2.2E+11

$2\text{-}C_{10}H_7O_2|i1' \rightarrow 2\text{-}C_{10}H_7O_2|i1$	3.2E+12	4.0E+12	4.6E+12
$2\text{-}C_{10}H_7O|i3 \rightarrow 2\text{-}C_{10}H_7O|i4$	1.4E+07	7.0E+08	7.2E+09
$2\text{-}C_{10}H_7O|i4 \rightarrow 2\text{-}C_{10}H_7O|i3$	2.0E+12	3.0E+12	3.7E+12
$2\text{-}C_{10}H_7O|i4 \rightarrow 2\text{-}C_{10}H_7O|i5$	8.5E+11	1.7E+12	2.6E+12
$2\text{-}C_{10}H_7O|i4 \rightarrow 2\text{-}C_{10}H_7O|i5'$	3.2E+10	1.8E+11	5.2E+11
$2\text{-}C_{10}H_7O|i5 \rightarrow 2\text{-}C_{10}H_7O|i4$	3.0E+08	2.8E+09	1.1E+10
$2\text{-}C_{10}H_7O|i5 \rightarrow C_9H_7 + CO$	4.9E+12	8.6E+12	1.2E+13
$2\text{-}C_{10}H_7O|i5' \rightarrow 2\text{-}C_{10}H_7O|i4$	4.8E+09	2.1E+10	5.3E+10
$2\text{-}C_{10}H_7O|i5' \rightarrow C_9H_7 + CO$	3.4E+12	5.5E+12	7.4E+12
$2\text{-}C_{10}H_7O_2|i8 \rightarrow 2\text{-}C_{10}H_7 + O_2$	1.1E+11	1.5E+12	7.0E+12
$2\text{-}C_{10}H_7O_2|i8 \rightarrow 2\text{-}C_{10}H_7O_2|i1$	6.9E+11	1.7E+12	3.0E+12
$2\text{-}C_{10}H_7O_2|i8 \rightarrow 2\text{-}C_{10}H_7O_2|i10$	2.6E+11	8.2E+11	1.6E+12
$2\text{-}C_{10}H_7O_2|i8 \rightarrow 2\text{-}C_{10}H_7O_2|i10'$	2.6E+11	8.2E+11	1.6E+12
$2\text{-}C_{10}H_7O_2|i10 \rightarrow 2\text{-}C_{10}H_7O_2|i8$	6.1E+01	4.1E+04	2.1E+06
$2\text{-}C_{10}H_7O_2|i10 \rightarrow 2\text{-}C_{10}H_7O_2|i21$	1.7E+11	2.0E+12	8.3E+12
$2\text{-}C_{10}H_7O_2|i10 \rightarrow 2\text{-}C_{10}H_7O_2|i23$	2.5E+11	1.8E+12	5.8E+12
$2\text{-}C_{10}H_7O_2|i10 \rightarrow 2\text{-}C_{10}H_7O_2|i11$	4.7E+08	5.9E+09	2.7E+10
$2\text{-}C_{10}H_7O_2|i21 \rightarrow 2\text{-}C_{10}H_7O_2|i10$	8.0E+11	1.6E+12	2.5E+12
$2\text{-}C_{10}H_7O_2|i21 \rightarrow 2\text{-}C_{10}H_7O_2|i22$	2.0E+12	2.5E+12	2.7E+12
$2\text{-}C_{10}H_7O_2|i21 \rightarrow 2\text{-}C_{10}H_7O_2|i20$	1.8E+07	2.1E+08	8.9E+08
$2\text{-}C_{10}H_7O_2|i22 \rightarrow 2\text{-}C_{10}H_7O_2|i21$	1.1E+12	1.5E+12	1.8E+12
$2\text{-}C_{10}H_7O_2|i22 \rightarrow 2\text{-}C_{10}H_7O_2|i23$	9.7E+11	1.9E+12	3.0E+12
$2\text{-}C_{10}H_7O_2|i23 \rightarrow 2\text{-}C_{10}H_7O_2|i22$	2.0E+12	4.4E+12	7.1E+12
$2\text{-}C_{10}H_7O_2|i23 \rightarrow 2\text{-}C_{10}H_7O_2|i17$	1.4E+09	9.8E+09	3.1E+10
$2\text{-}C_{10}H_7O_2|i23 \rightarrow 2\text{-}C_{10}H_7O_2|i10$	1.3E+12	2.1E+12	2.7E+12
$2\text{-}C_{10}H_7O_2|i23 \rightarrow 2\text{-}C_{10}H_7O_2|i17$	2.1E+10	1.6E+11	5.7E+11
$2\text{-}C_{10}H_7O_2|i23 \rightarrow 2\text{-}C_{10}H_7O_2|i10$	1.1E+13	1.6E+13	2.0E+13
$2\text{-}C_{10}H_7O_2|i17 \rightarrow 2\text{-}C_{10}H_7O_2|i23$	2.7E+12	3.5E+12	4.0E+12
$2\text{-}C_{10}H_7O_2|i17 \rightarrow 2\text{-}C_9H_7O + CO$	1.5E+11	4.1E+11	7.4E+11

Reaction			
$2\text{-}C_{10}H_7O_2|i20 \rightarrow 2\text{-}C_{10}H_7O_2|i21$	2.6E+10	1.2E+11	2.8E+11
$2\text{-}C_{10}H_7O_2|i20 \rightarrow 2\text{-}C_{10}H_7O_2|i37$	9.4E+03	2.1E+06	5.5E+07
$2\text{-}C_{10}H_7O_2|i20 \rightarrow 2\text{-}C_{10}H_7O_2|i39$	5.9E+07	1.6E+10	4.8E+11
$2\text{-}C_{10}H_7O_2|i37 \rightarrow 2\text{-}C_{10}H_7O_2|i20$	2.3E+02	2.5E+05	1.7E+07
$2\text{-}C_{10}H_7O_2|i37 \rightarrow C_{10}H_6O_2 + H$	2.5E+04	2.3E+07	1.4E+09
$2\text{-}C_{10}H_7O_2|i39 \rightarrow 2\text{-}C_{10}H_7O_2|i20$	6.3E+08	9.8E+09	5.1E+10
$2\text{-}C_{10}H_7O_2|i39 \rightarrow C_{10}H_6O_2 + H$	1.2E+11	4.5E+11	1.0E+12
$2\text{-}C_{10}H_7O_2|i11 \rightarrow 2\text{-}C_{10}H_7O_2|i10$	7.8E+07	2.7E+09	2.3E+10
$2\text{-}C_{10}H_7O_2|i11 \rightarrow 2\text{-}C_{10}H_7O_2|i12$	8.1E+11	8.2E+11	8.2E+11
$2\text{-}C_{10}H_7O_2|i11 \rightarrow 2\text{-}C_{10}H_7O_2|i13$	4.3E+12	4.6E+12	4.9E+12
$2\text{-}C_{10}H_7O_2|i12 \rightarrow 2\text{-}C_{10}H_7O_2|i11$	1.7E+10	3.7E+10	5.8E+10
$2\text{-}C_{10}H_7O_2|i12 \rightarrow C_9H_7 + CO_2$	6.3E+11	8.3E+11	9.8E+11
$2\text{-}C_{10}H_7O_2|i12 \rightarrow 2\text{-}C_{10}H_7O_2|i32$	2.1E+11	7.8E+11	1.7E+12
$2\text{-}C_{10}H_7O_2|i13 \rightarrow 2\text{-}C_{10}H_7O_2|i11$	6.3E+11	1.6E+12	2.8E+12
$2\text{-}C_{10}H_7O_2|i13 \rightarrow C_9H_7 + CO_2$	1.5E+09	1.9E+10	8.5E+10
$2\text{-}C_{10}H_7O_2|i32 \rightarrow 2\text{-}C_{10}H_7O_2|i12$	3.9E+08	7.2E+09	4.1E+10
$2\text{-}C_{10}H_7O_2|i32 \rightarrow 2\text{-}C_{10}H_7O_2|i30$	8.5E+08	3.9E+09	9.8E+09
$2\text{-}C_{10}H_7O_2|i32 \rightarrow 2\text{-}C_{10}H_7O_2|i30'$	7.1E+07	7.2E+09	1.2E+11
$2\text{-}C_{10}H_7O_2|i30 \rightarrow 2\text{-}C_{10}H_7O_2|i31$	8.5E+08	4.1E+09	1.1E+10
$2\text{-}C_{10}H_7O_2|i30' \rightarrow 2\text{-}C_{10}H_7O_2|i32$	2.2E+07	1.6E+09	2.2E+10
$2\text{-}C_{10}H_7O_2|i30' \rightarrow C_8H_5O_2 + C_2H_2$	1.3E+02	6.6E+04	2.9E+06
$2\text{-}C_{10}H_7O_2|i10' \rightarrow 2\text{-}C_{10}H_7O_2|i8$	4.3E+11	3.0E+12	9.7E+12
$2\text{-}C_{10}H_7O_2|i10' \rightarrow 2\text{-}C_{10}H_7O_2|i23'$	6.4E+11	4.1E+12	1.3E+13
$2\text{-}C_{10}H_7O_2|i10' \rightarrow 2\text{-}C_{10}H_7O_2|i21'$	1.5E+09	1.3E+10	4.9E+10
$2\text{-}C_{10}H_7O_2|i10' \rightarrow 2\text{-}C_{10}H_7O_2|i11'$	9.2E+11	1.6E+12	2.1E+12
$2\text{-}C_{10}H_7O_2|i21' \rightarrow 2\text{-}C_{10}H_7O_2|i10'$	2.5E+12	3.5E+12	4.2E+12
$2\text{-}C_{10}H_7O_2|i21' \rightarrow 2\text{-}C_{10}H_7O_2|i22'$	1.7E+10	3.3E+10	4.9E+10
$2\text{-}C_{10}H_7O_2|i21' \rightarrow 2\text{-}C_{10}H_7O_2|i20'$	1.4E+12	2.2E+12	3.0E+12
$2\text{-}C_{10}H_7O_2|i22' \rightarrow 2\text{-}C_{10}H_7O_2|i21'$	2.4E+12	3.6E+12	4.6E+12

2-$C_{10}H_7O_2$|i22' → 2-$C_{10}H_7O_2$|i23'	6.1E+11	1.5E+12	2.6E+12
2-$C_{10}H_7O_2$|i23' → 2-$C_{10}H_7O_2$|i10'	6.0E+06	1.5E+08	1.0E+09
2-$C_{10}H_7O_2$|i23' → 2-$C_{10}H_7O_2$|i17'	4.4E+12	7.5E+12	1.0E+13
2-$C_{10}H_7O_2$|i23' → 2-$C_{10}H_7O_2$|i22'	6.4E+12	8.6E+12	1.0E+13
2-$C_{10}H_7O_2$|i20' → 2-$C_{10}H_7O_2$|i21'	1.5E+10	8.3E+10	2.4E+11
2-$C_{10}H_7O_2$|i20' → 2-$C_{10}H_7O_2$|i37'	1.6E+10	9.1E+10	2.6E+11
2-$C_{10}H_7O_2$|i20' → 2-$C_{10}H_7O_2$|i39'	5.1E+11	2.2E+12	5.4E+12
2-$C_{10}H_7O_2$|i20' → $C_{10}H_6O_2$ + H	1.3E+11	4.8E+11	1.0E+12
2-$C_{10}H_7O_2$|i17' → 2-$C_{10}H_7O_2$|i23'	8.3E+12	1.1E+13	1.4E+13
2-$C_{10}H_7O_2$|i17' → 2-C_9H_7O + CO	3.2E+08	4.4E+09	2.1E+10
2-$C_{10}H_7O_2$|i37' → 2-$C_{10}H_7O_2$|i20'	5.5E+09	6.7E+10	3.0E+11
2-$C_{10}H_7O_2$|i37' → $C_{10}H_6O_2$ + H	2.0E+04	6.6E+06	2.1E+08
2-$C_{10}H_7O_2$|i39' → 2-$C_{10}H_7O_2$|i20'	6.7E+05	1.9E+08	5.7E+09
2-$C_{10}H_7O_2$|i39' → $C_{10}H_6O_2$ + H	1.1E+09	1.5E+10	7.4E+10
2-$C_{10}H_7O_2$|i11' → 2-$C_{10}H_7O_2$|i10'	1.3E+10	9.4E+10	3.1E+11
2-$C_{10}H_7O_2$|i11' → 2-$C_{10}H_7O_2$|i13'	2.6E+09	3.4E+10	1.6E+11
2-$C_{10}H_7O_2$|i11' → C_9H_7 + CO_2	1.1E+11	2.3E+11	3.4E+11
2-$C_{10}H_7O_2$|i13' → 2-$C_{10}H_7O_2$|i11'	3.8E+10	1.9E+11	5.1E+11
2-$C_{10}H_7O_2$|i13' → C_9H_7 + CO_2	5.3E+12	4.7E+12	4.2E+12

An important finding of the RRKM-ME simulations is the fact that collisionally stabilized intermediates were not detected as products in the temperature range of 1500−2500 K and at all studied pressures. The MultiWell calculations performed at four different pressures revealed that the combined yield of phenoxy radical and its decomposition product C_5H_5 + CO as well as the combined yields of 1- or 2-naphthoxy radicals and their decomposition product indenyl + CO, are pressure-independent. The same is true for the branching ratios of all other reaction products. Hence, Figure 3.13 shows plots of the branching ratios only as functions of temperature.

The oxygen atom elimination, leading to phenoxy + O and eventually to C_5H_5 + CO + O, is the dominant reaction channel for the phenyl + O_2 system, with its branching ratio increasing from 0.83 at 1500 K to 0.97 at 2500 K. The second significant channel is pyranyl + CO with the highest yield of 0.10 observed at the lowest temperature of 1500 K. For all other products, including C_5H_5 + CO_2 and 1,2-$C_6H_4O_2$ + H, the branching ratios do not exceed 0.05. The product yields are similar for the 2-naphthyl + O_2 reaction, where the combined branching ratio of the 2-naphthoxy + O/indenyl + CO products increases

from 0.81 at 1500 K to 0.95 at 2500 K. The only slight difference from the phenyl + O_2 system is that the relative yields of the other products are nearly equally distributed at 0.06-0.07 (1500 K), 0.03-0.04 (2000 K), and 0.01-0.02 (2500 K).

The 1-naphthyl + O_2 reaction displays a somewhat distinct behavior. The O atom elimination channel leading to 1-naphthoxy and then to indenyl + CO is still the major channel, with its branching ratio increasing from 0.51 to 0.77 with temperature. However, the contributions of the other channels are more significant than those for the phenyl + O_2 and 2-naphthyl + O_2 reactions; for instance, the branching ratios of 1-benzopyranyl + CO, 1,2-$C_{10}H_6O_2$ + H, and indenyl + CO_2 range from 0.24, 0.14, and 0.11 at 1500 K to 0.13, 0.07, and 0.03 at 2500 K, respectively. The higher yields of these other products formed after an O atom insertion into the aromatic ring in the 1-naphthyl + O_2 reaction correlates well with the relative energy of the transition state for this insertion, -25.5 kcal/mol with respect to the initial reactants, that is substantially lower than the corresponding values for the phenyl + O_2 and 2-naphthyl + O_2 reactions, -18.9 and -20.0 kcal/mol, respectively [31, 75].
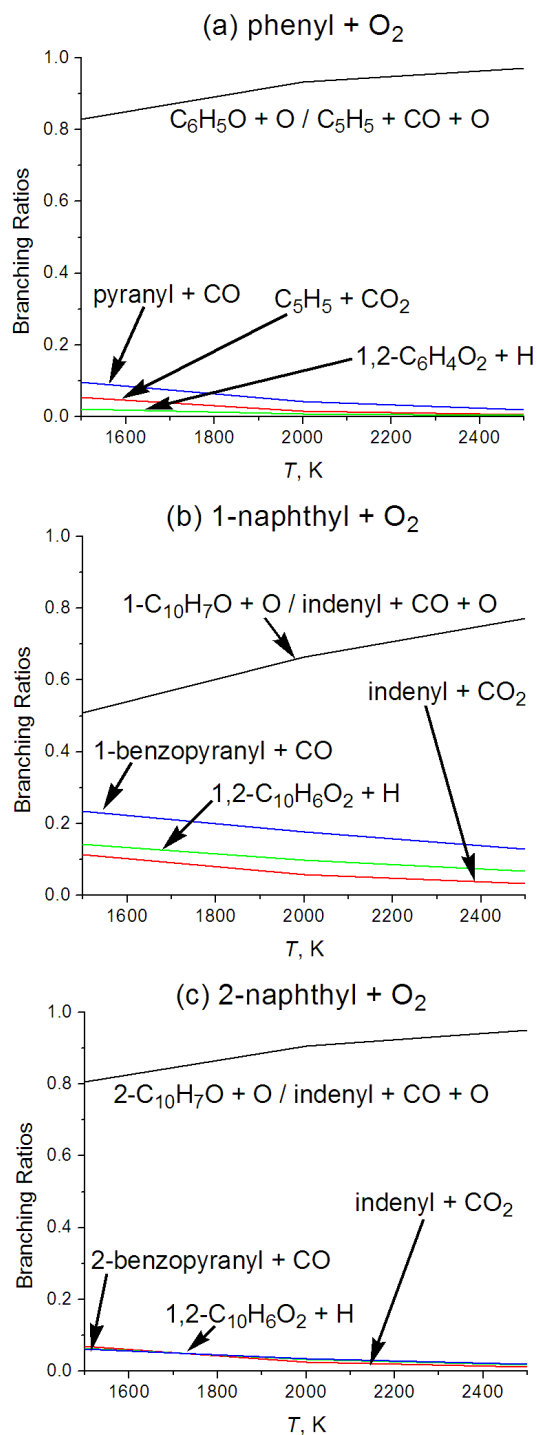
Figure 3.13. Temperature dependence of product branching ratios of the (a) phenyl + O_2, (b) 1-naphthyl + O_2, and (c) 2-naphthyl + O_2 reactions. Combined branching ratios are shown for the C_6H_5O+O/C_5H_5+CO+O, 1-$C_{10}H_7O+O$/indenyl+CO+O, and 1-$C_{10}H_7O+O$/indenyl+CO+O products.

The phenoxy and naphthoxy radicals formed after elimination of an O atom from the initial phenyl peroxy and naphthyl peroxy radical complexes can further dissociate to $C_5H_5 + CO$ or indenyl + CO due to their chemical activation or, alternatively, can be thermally equilibrated by collisions. The equilibrated species may then undergo thermal decomposition but this secondary reaction mechanism was not considered in this analysis. The equilibrated C_6H_5O and $1-/2-C_{10}H_7O$ radicals were counted as final products of the primary reactions.

The MultiWell calculations reveal that the branching ratios of $C_6H_5O + O$ vs. $C_5H_5 + CO + O$ and of $1-/2-C_{10}H_7O + O$ vs. indenyl + CO + O strongly depend both on temperature and pressure. Figure 3.14 shows rate coefficients for the formation of these individual products at different pressures and temperatures, which are computed by multiplying the total rate coefficients with the product branching ratios. In the phenyl + O_2 reaction, at the lowest pressure of 0.01 atm and a temperature of 1500 K, a large fraction of phenoxy radicals equilibrate rather than dissociate and the computed rate coefficients for the formation of the $C_6H_5O + O$ and $C_5H_5 + CO + O$ products are 1.74×10^{-11} and 7.06×10^{-12} cm^3 molecule^{-1} s^{-1}, with their respective branching ratios being 0.59 and 0.24, respectively. However, dissociation becomes more favorable than equilibration with a further temperature increase, and the rate coefficient to produce $C_5H_5 + CO + O$ and its branching ratio rise to 3.90×10^{-11} cm^3 molecule^{-1} s^{-1} and 0.94, respectively. The rate coefficient and branching ratio for the reaction channel leading to $C_6H_5O + O$ drop to 1.33×10^{-12} cm^3 molecule^{-1} s^{-1} and 0.03, respectively. The increase in pressure at constant temperature increases the yield of equilibrated C_6H_5O and accordingly the rate coefficient to form this product. Since the combined branching ratio of the two products is pressure-independent, the pressure increase also reduces the yield and the rate coefficient for $C_5H_5 + CO + O$. Nevertheless, even at the highest pressure of 10 atm and temperature of 2500 K most of phenoxy radicals dissociate and the branching ratio of $C_5H_5 + CO + O$ is still 0.61 vs. 0.36 for equilibrated $C_6H_5O + O$.
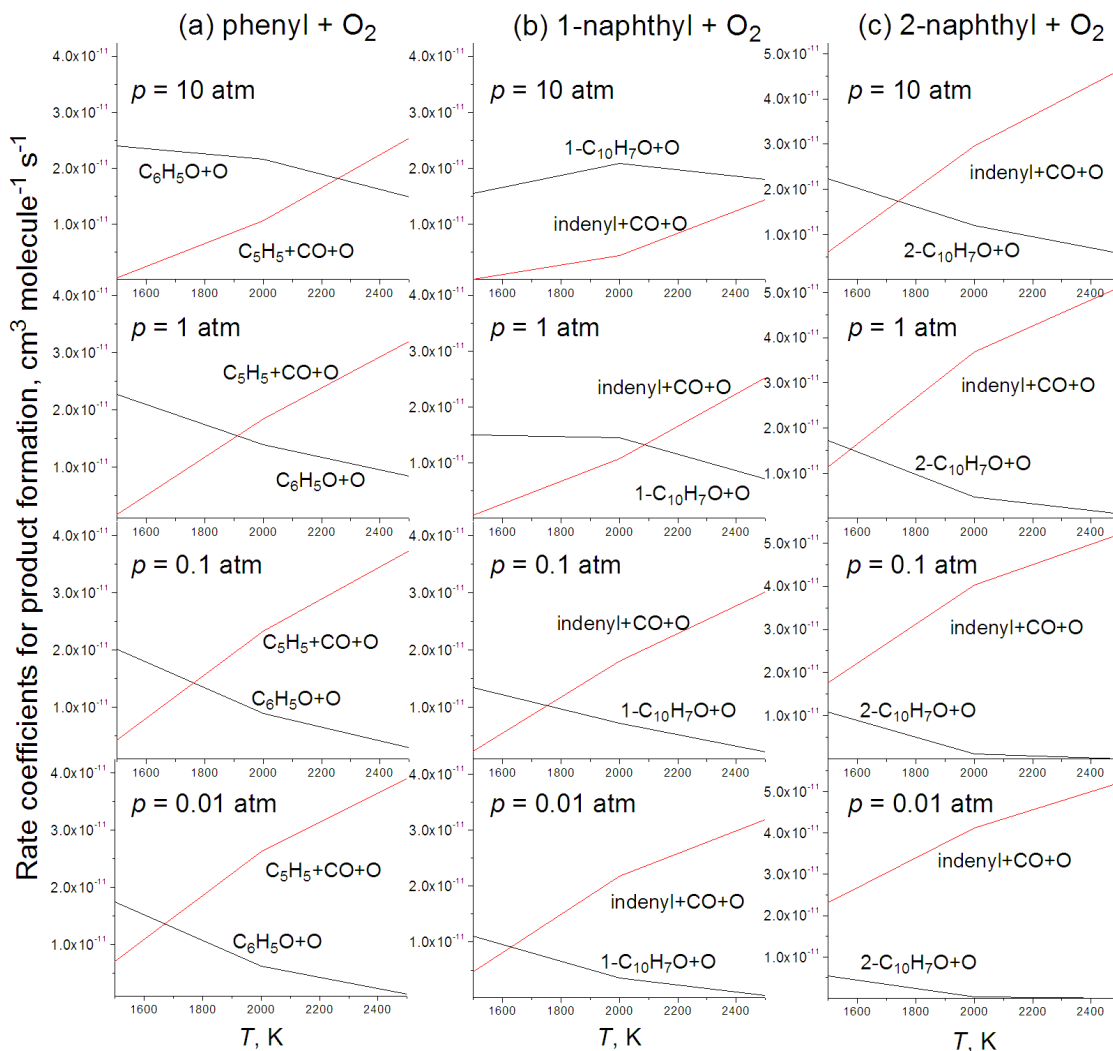
Figure 3.14. Rate coefficients for the formation of the $C_6H_5O + O$ and C_5H_5+CO+O products in the (a) phenyl + O_2 reaction, $1\text{-}C_{10}H_7O + O$ and indenyl + CO + O in the (b) 1-napthyl + O_2 reaction, and $2\text{-}C_{10}H_7O + O$ and indenyl + CO + O in the (c) 2-napthyl + O_2 reaction calculated at different temperatures and pressures.

The 1-naphthyl + O_2 reaction shows similar trends but with two caveats. First, the combined branching ratios of $1\text{-}C_{10}H_7O + O$/indenyl + CO + O are lower than the respective values for $C_6H_5O + O$/$C_5H_5 + CO$ +O and hence, the individual rate coefficients of both 1-naphthoxy and indenyl product channels are lower as compared to those for phenoxy and cyclopentadienyl. Second, the decomposition of chemically-activated 1-naphthoxy radicals to indenyl + CO from the 1-naphthyl + O_2 reaction is generally less favorable than the decomposition of chemically-activated phenoxy radicals from phenyl + O_2. As a result, at the high pressure of 10 atm, which strongly favors the equilibration process, the computed branching ratio of indenyl + CO + O, 0.34, remains lower than the respective value of 0.43 for 1-naphthoxy+O even at the highest temperature of 2500 K.

The 2-naphthyl + O$_2$ reaction exhibits similar trends: the relative yield for the indenyl + CO + O decomposition products and the respective rate coefficient increase with temperature and decrease with pressure, whereas the opposite behavior is observed for the equilibrated 2-naphthoxy product. However, the decomposition process in this system appears to be significantly more favorable. At the lowest pressure of 0.01 atm, least conducive for equilibration, the branching ratio of indenyl + CO + O ranges from 0.66 at 1500 K to 0.95 at 2500 K, with that for equilibrated 2-naphthoxy + O being 0.15 and 0.00, respectively.

The 2-naphthoxy + O product becomes more favorable than indenyl only at the higher pressures of 1 and 10 atm and only at our lowest temperature of 1500 K, whereas at higher temperatures, especially at 2500 K, indenyl remains the dominant product. Again, the differences in the branching ratios of the C$_5$H$_5$ + CO + O and indenyl + CO +O decomposition products can be traced back to the PESs for the fragmentation of phenoxy and 1- and 2-naphthoxy radicals. The critical barriers on their dissociation pathways were computed to be 53.8, 58.2, and 48.3 kcal/mol, respectively [31, 75], clearly indicating that the decomposition process is most favorable for 2-naphthoxy and least favorable for 1-naphthoxy, in line with the observed trends in the branching ratios. In turn, the difference in the barrier heights for the phenoxy and naphthoxy radicals can be attributed to the difference in the relative stability of the bi(tri)cyclic intermediates phenoxy, 1-naphthoxy, and 2-naphthoxy [31, 75], where 1-naphthoxy is destabilized as compared to phenoxy due to the rigidity introduced by the presence of the additional C$_6$ ring next to the rearrangement site, but 2-naphthoxy in contrast is stabilized by extra electronic delocalization owing to the presence of the additional ring away from the rearrangement site.

Based on the results for the phenyl + O$_2$ and naphthyl + O$_2$ reactions, the only reaction pathway considered was the addition of molecular oxygen to the radical site followed by elimination of an oxygen atom and consequent unimolecular decomposition of the oxyradical. The reaction channels involving insertion of one of the oxygen atoms into the aromatic ring followed by decomposition of the resulting intermediate with the PAH$^\bullet$-O$_2$ stoichiometry (here, C$_{16}$H$_9$O$_2$$^\bullet$) are ignored, keeping in mind that they may be responsible for up to 15–24 % of the reaction products in the temperature range of 1500–2500 K. The following tables show calculated temperature- and pressure-dependent rate coefficients for the formation of oxypyrenyl from pyrenyl + O$_2$ (Table 3.34) and high-pressure rate coefficients of the elementary unimolecular reaction steps (Table 3.35).

Table 3.34. Rate coefficient (in cm^3 s^{-1}) of the reaction C$_{16}$H$_9$ + O$_2$ → C$_{16}$H$_9$O + O.

T (K)	P (atm)					
	0.01	0.1	1	10	100	High-P
1000	2.8E-11	2.8E-11	2.8E-11	2.8E-11	2.8E-11	2.8E-11
1250	3.8E-11	4.0E-11	4.0E-11	4.0E-11	4.0E-11	4.0E-11
1500	3.3E-11	3.8E-11	4.7E-11	5.0E-11	5.0E-11	5.0E-11
1750	1.5E-11	2.3E-11	4.2E-11	5.5E-11	5.6E-11	5.6E-11
2000	4.3E-12	1.1E-11	2.5E-11	5.3E-11	6.1E-11	6.3E-11
2250	1.4E-12	4.7E-12	1.3E-11	4.8E-11	6.3E-11	6.6E-11
2500	3.8E-13	1.8E-12	7.0E-12	4.2E-11	6.3E-11	7.0E-11

Table 3.35. High-pressure rate coefficients (in s^{-1}) of the elementary reactions in the C$_{16}$H$_9$ + O$_2$ reaction system.

Reaction	1500 K	2000 K	2500 K
C$_{16}$H$_9$O$_2$|i1 → C$_{16}$H$_9$O + O	1.3E+10	1.6E+11	7.4E+11
C$_{16}$H$_9$O$_2$|i1 → C$_{16}$H$_9$|i1 + O$_2$	8.5E+08	3.8E+10	3.5E+11
C$_{16}$H$_9$O|i1 → C$_{16}$H$_9$O|i2	1.3E+05	2.4E+07	5.5E+08
C$_{16}$H$_9$O|i2 → C$_{16}$H$_9$O|i1	7.6E+07	1.2E+09	6.1E+09
C$_{16}$H$_9$O|i2 → C$_{15}$H$_9$ + CO	7.0E+12	1.3E+13	1.9E+13

Figure 3.15 shows the pressure dependence for the rate coefficient of reaction pyrenyl C$_{16}$H$_9$ + O$_2$ → oxypyrenyl C$_{16}$H$_9$O + O, which becomes significant at temperatures above 1500 K. For instance, at 2500 K and a pressure of 0.01 atm, the rate coefficient of formation of oxypyrenyl + O is over two orders of magnitude lower than the high-pressure limit.

Figure 3.16 compares the high-pressure-limit rate coefficient of reaction pyrenyl + O$_2$ → oxypyrenyl + O to the high-pressure-limit rate coefficients of reactions phenyl + O$_2$ → phenoxy + O, 1-naphthyl + O$_2$ → 1-naphthoxy + O, and 2-naphthyl + O$_2$ → 2-naphthoxy + O. As can be seen from the displayed results, the reactions forming phenoxy + O and 2-naphthoxy + O are 100 and 40 % faster, respectively, than the one forming oxypyrenyl + O. The rate coefficient of the reaction forming 1-naphthoxy + O is within 10 % of that forming oxypyrenyl + O. As the number of rings increases from one to four, the rate of oxidation of the six-member ring decreases by a factor of two. These surface reactions for the oxidation of six-member rings by O$_2$ and their corresponding high-pressure-limit rate coefficients were added to the KMC soot oxidation model.
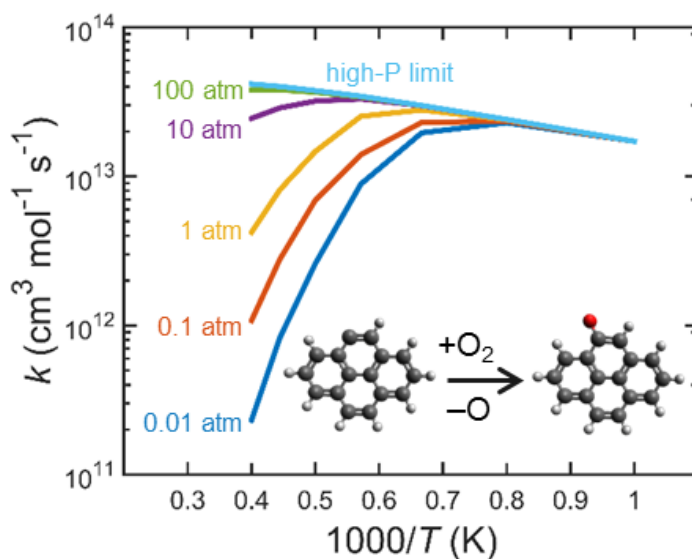
Figure 3.15. Computed rate coefficient for reaction pyrenyl + O_2 → oxypyrenyl + O.
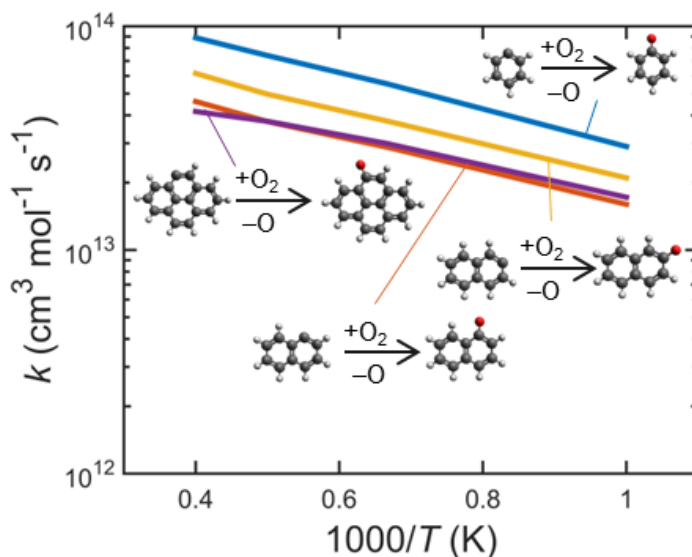
Figure 3.16. Comparison of high-pressure-limit rates coefficients computed for reactions phenyl + O_2 → phenoxy + O, 1-naphthyl + O_2 → 1-naphthoxy + O, 2-naphthyl + O_2 → 2-naphthoxy + O, and pyrenyl + O_2 → oxypyrenyl + O.

3.5 Summary

The energetics and kinetics of oxidation of six-member rings by molecular oxygen were explored in this chapter. The product branching ratios illustrated that the dominant reaction channel in all cases is elimination of the oxygen atom from peroxy complexes formed at the initial O_2 addition step, leading to the phenoxy, naphthoxy, and oxypyrenyl radical

50

products, with its contribution increasing with temperature. Chemically-activated oxyradicals either decompose to form a five-member ring and produce CO, thus completing the conversion of the six-member ring to a five-member ring upon oxidation, or thermally equilibrate, with the relative yields of the two processes strongly depending on temperature and pressure. In the high-pressure-limit, thermal equilibration was favored. The high-pressure-limit rate coefficients for the reactions phenyl + $O_2 \rightarrow$ phenoxy + O, 1-naphthyl + $O_2 \rightarrow$ 1-naphthoxy + O, 2-naphthyl + $O_2 \rightarrow$ 2-naphthoxy + O, and pyrenyl + $O_2 \rightarrow$ oxypyrenyl + O were calculated, and the reactions and rate coefficients were incorporated into the KMC oxidation model.

4 Oxidation of Graphene-Edge Five-Member Rings by Molecular Oxygen

This chapter discusses the results of RRKM-ME calculations of rate coefficients and relative product yields for the reaction in which an embedded five-member ring is oxidized by molecular oxygen. This reaction and its corresponding rate coefficients were added to the detailed oxidation model.

4.1 Introduction

The reactions for the oxidation of six-member rings by O_2 (discussed in Chapter 3) were added to the KMC surface oxidation model along with reactions for thermal decomposition of oxyradicals (reactions $51 - 54$), oxidation of six-member rings by OH (reactions $55 - 59$), as well as O, H, and OH addition and abstraction reactions (reactions $60 - 89$). The newly-developed oxidation model was combined with the detailed surface growth model developed by Whitesides and Frenklach [21, 53]. However, the very initial attempts to examine graphene-edge oxidation with the combined models encountered fundamental problems.

Initial KMC simulations of a pre-grown graphene "sheet" with an excess of molecular oxygen showed that degradation of the graphene moiety quickly comes to a stop. Inspection revealed that the graphene edge becomes "non-reactive" due to accumulation of embedded five-member rings. The initial model did not include direct oxidation of five-member rings based on the presumption of rapid thermal desorption of five-member rings migrating over the graphene edge and, consequently, infrequency of their embedding into the graphene layer. The numerical simulations disproved this assumption. One of the reasons for this is that the source of five-member rings in an oxidative environment is not only acetylene adsorption to a zigzag site or thermal isomerization of six-member-ring complexes, but also oxidation of six-member rings.

Another problem that appeared in the initial KMC simulations was the formation of unrealistic compounds. For instance, starting with a pyrene molecule, the initial oxidation converts one of its six-member rings to an embedded five-member ring,
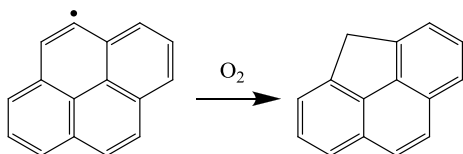
(Step I)

Following the same reaction mechanism leads to the formation of two adjacent five-member rings

$O_2 \longrightarrow$

, (Step II)
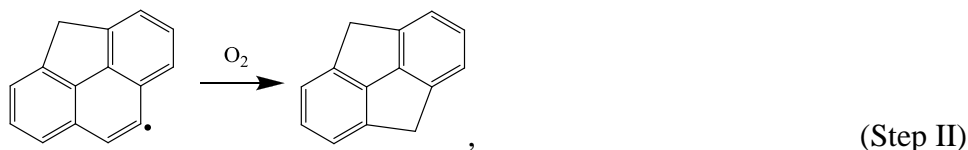
which defies the so-called isolated pentagon rule [77-80].

Thus, the next step towards building a detailed surface oxidation model of soot is to investigate theoretically the mechanism and products of oxidation of five-member rings embedded into a graphene layer, and then compare this reaction to the oxidation of six-member rings.

Previously, Raj et al. [81] investigated the oxidation of embedded five-member rings in their combined experimental and theoretical study of structural effects on the oxidation of soot particles. Experimentally, they found that curved soot particles are oxidized easier than planar ones. In order to explain this observation and to understand the role of the PAH structure in the reactivity towards O_2, these authors carried out theoretical calculations using density functional B3LYP and Hartree–Fock methods of the reaction pathways of 4-pyrenyl and 1-corannulenyl with O_2, using these radicals as models of planar and curved PAHs, respectively. The calculations suggested a mechanism in which the six-member ring of the pyrenyl radical is oxidized by an oxygen molecule and is eventually converted into a five-member ring, similar to the reactions of phenyl and naphthyl radicals with molecular oxygen. The oxidation of a five-member ring with a second O_2 molecule follows and results in the full destruction of the five-member ring with the formation of the phenanthryl radical. The oxidation mechanism of 1-corannulenyl was found to be similar, but with significantly lower activation energies, which explained the experimentally observed higher reactivity of curved PAH structures. However, the energetic parameters computed along the reaction pathways at the B3LYP//HF level may not be reliable, which may significantly influence the evaluation of rate coefficients for the oxidation reactions.

In order to achieve better qualitative and quantitative understanding of oxidation processes of large PAH radicals, particularly embedded five-member rings, I performed a theoretical study of the reaction $C_{15}H_9 + O_2$.

4.2 Potential Energy Surfaces

Mebel calculated the energetics of the $C_{15}H_9 + O_2$ reaction at the G3 level of theory. G3(MP2,CC)//B3LYP/6-311G**. Figures 4.1 and 4.2 show the potential energy diagrams for this reaction.
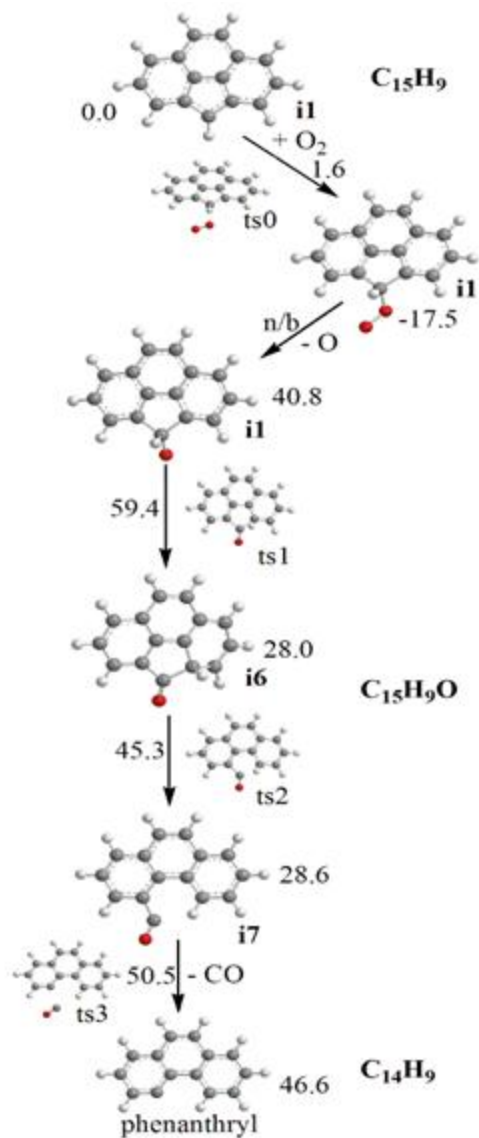
Figure 4.1. Potential energy diagram for the first pathway of the $C_{15}H_9 + O_2$ reaction. Relative energies are given in kcal/mol as calculated at the G3 level.
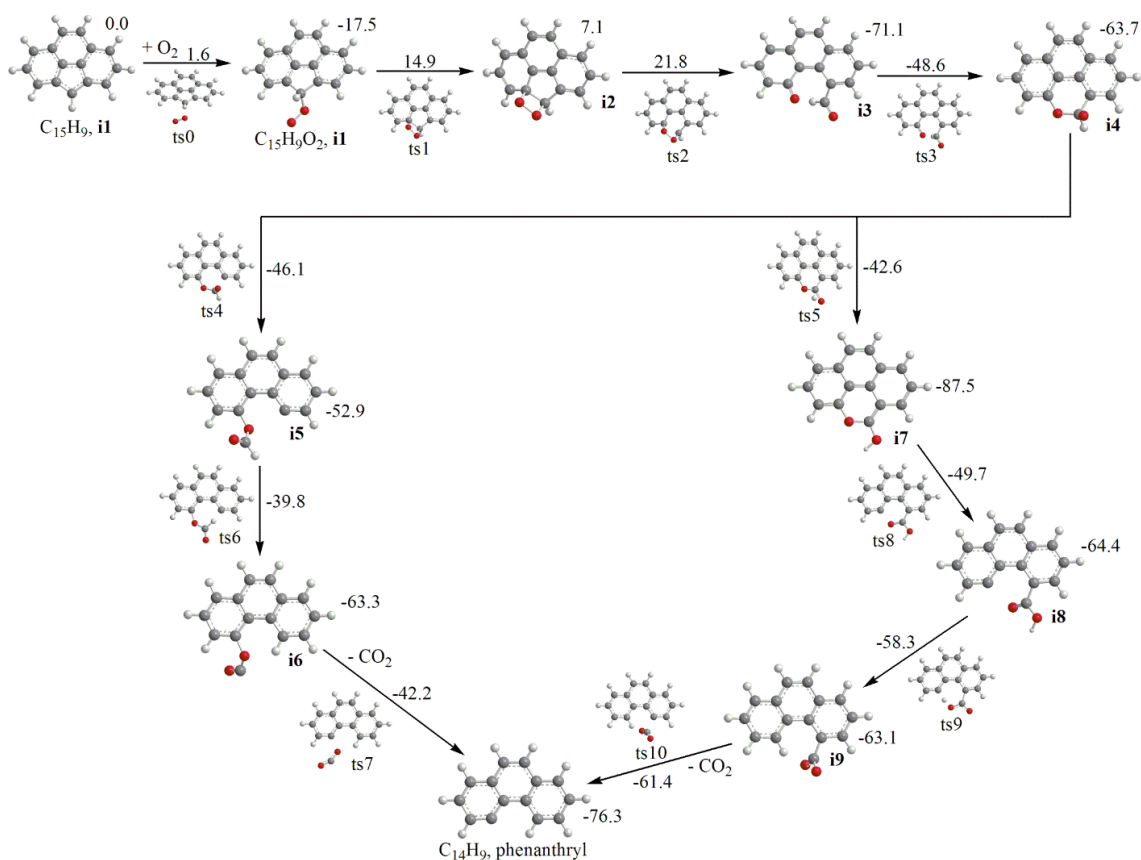
Figure 4.2. Potential energy diagram for the second pathway of the $C_{15}H_9$ + O_2 reaction. Relative energies are given in kcal/mol as calculated at the G3 level.

Unlike the six-member ring oxidation reactions, the association of $C_{15}H_9$ and O_2 to form the initial adduct is not barrierless and proceeds via a transition state located 1.6 kcal/mol above the reactants. The adduct can then undergo dissociation of the $O - O$ bond to form $C_{15}H_9O + O$. The $C_{15}H_9O$ radical can further dissociate to $C_{14}H_9 + CO$ as seen in Figure 4.1. Alternatively, the adduct can follow the second pathway shown in Figure 4.2 to produce phenanthryl $C_{14}H_9 + CO_2$. Further discussion of the potential energy surfaces can be found in [82].

4.3 Reaction Rate Coefficient Calculations

VRC-TST calculations were performed for the barrierless $C_{15}H_9O$ + O association channels. The MEP for this channel was computed at the B3LYP/6-311G** level of theory and scaled to match the oxygen atom elimination energy calculated at the G3(MP2,CC) level. The scaling was done by multiplying the MEP computed at the B3LYP level of theory by the ratio of the bond dissociation energy calculated at the G3 level to that calculated at the B3LYP level.

The RRKM-ME calculations for the $C_{15}H_9 + O_2$ reaction were performed in a similar manner and for the same range of temperatures and pressures as the calculations for the pyrenyl + O_2 reaction presented in Chapter 3. The computed rates coefficients of the $C_{15}H_9$ + O_2 reaction exhibited no dependence on pressure and are displayed in Figure 4.3 as well as in Tables 4.1 and 4.2. As can be seen from these results, the $C_{14}H_9 + CO_2$ formation is much faster that the formation of $C_{15}H_9O + O$ for all temperatures considered here, with the difference between the two increasing with the decrease in temperature. A closer look at these results, displayed as a branching ratio in Figure 4.4, indicates that the CO_2 producing channel is the dominant one at lower and combustion temperatures. This conclusion is consistent with the isolated pentagon rule [77-80] that prohibits formation of two adjacent five-member rings.
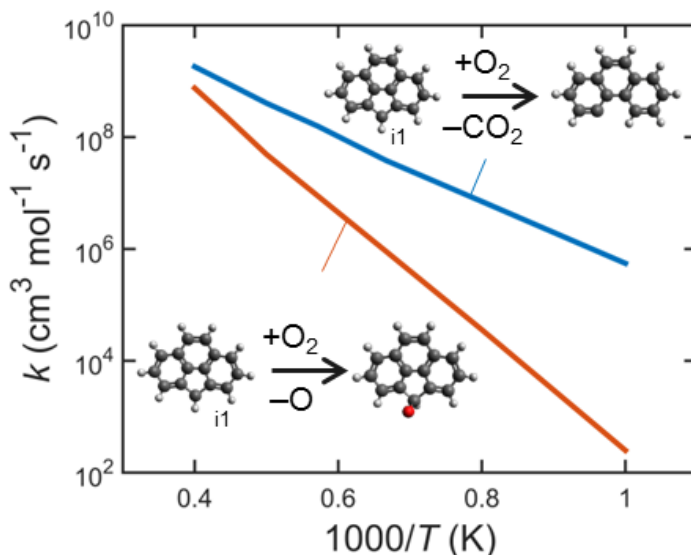
Figure 4.3. Computed rate coefficients for reactions $C_{15}H_9 + O_2 \rightarrow C_{14}H_9 + CO_2$ and $C_{15}H_9 + O_2 \rightarrow C_{15}H_9O + O$.

Table 4.1. Rate coefficient (in cm^3 s^{-1}) of the reaction $C_{15}H_9 + O_2 \rightarrow C_{15}H_9O + O$.

T (K)	k
1000	4.2E-22
1250	6.0E-20
1500	1.5E-18
1750	1.5E-17
2000	8.1E-17
2250	3.8E-16
2500	1.2E-15

Table 4.2. Rate coefficient (in cm^3 s^{-1}) of the reaction $C_{15}H_9 + O_2 \rightarrow C_{14}H_9 + CO_2$.

T (K)	k
1000	9.1E-19
1250	1.2E-17
1500	6.3E-17
1750	2.7E-16
2000	6.8E-16
2250	1.6E-15
2500	3.0E-15
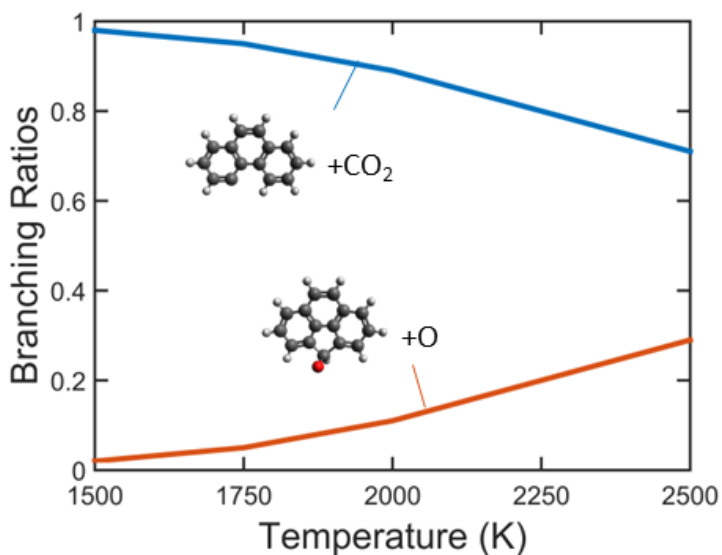
Figure 4.4. Computed product branching ratios of the $C_{15}H_9 + O_2$ reaction.

In Figure 4.5 the calculated values are compared with those of Raj et al. [81, 83] for the high-pressure-limit rate coefficients computed for the oxidation of six- and five-member rings, $C_{16}H_9 + O_2 \rightarrow C_{16}H_9O + O$ and $C_{15}H_9 + O_2 \rightarrow C_{14}H_9 + CO_2$, respectively. The values I computed are about two orders of magnitude higher than those of Raj et al. for the corresponding reactions. Both studies, however, are in agreement that the oxidation of a six-member ring is over four orders of magnitude faster than the oxidation of a five-member ring. Table 4.3 shows the high-pressure rate coefficients for the elementary reactions of the $C_{15}H_9 + O_2$ reaction system.
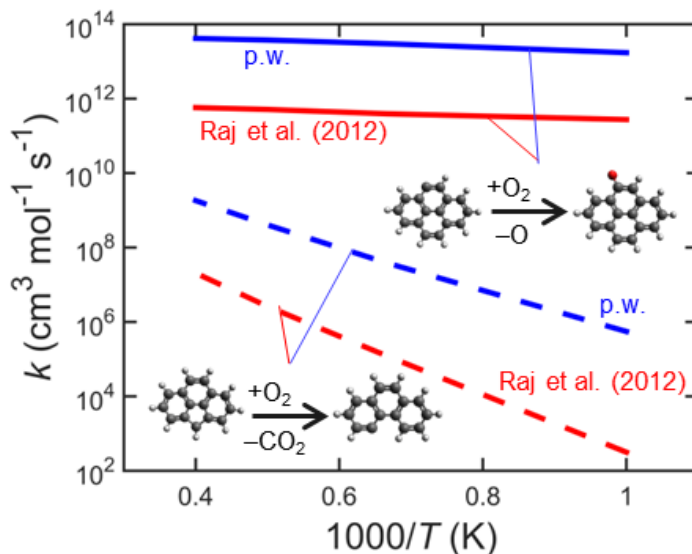
Figure 4.5. Rates Comparison of high-pressure-limit rate coefficients computed in the present study to values reported by Raj et al. [83].

Table 4.3. High-pressure rate coefficients (in s^{-1}) of the elementary reactions in the $C_{15}H_9$ + O_2 reaction system.

Reaction	1500 K	2000 K	2500 K
$C_{15}H_9O_2\|i1 \rightarrow C_{15}H_9O + O$	1.8E+05	3.1E+07	6.7E+08
$C_{15}H_9O_2\|i1 \rightarrow C_{15}H_9 + O_2$	2.3E+11	1.3E+12	3.8E+12
$C_{15}H_9O_2\|i1 \rightarrow C_{15}H_9O_2\|i2$	8.0E+07	1.3E+09	6.9E+09
$C_{15}H_9O\|i10 \rightarrow C_{15}H_9O\|i11$	2.4E+10	1.3E+11	3.7E+11
$C_{15}H_9O\|i11 \rightarrow C_{15}H_9O\|i10$	3.1E+08	5.0E+09	2.7E+10
$C_{15}H_9O\|i11 \rightarrow C_{15}H_9O\|i12$	5.4E+10	2.5E+11	6.3E+11
$C_{15}H_9O\|i12 \rightarrow C_{15}H_9O\|i11$	3.0E+09	1.2E+10	2.9E+10
$C_{15}H_9O\|i12 \rightarrow C_{14}H_9 + CO$	1.6E+11	1.2E+12	3.9E+12
$C_{15}H_9O_2\|i2 \rightarrow C_{15}H_9O_2\|i1$	9.5E+11	1.9E+12	3.0E+12
$C_{15}H_9O_2\|i2 \rightarrow C_{15}H_9O_2\|i3$	1.0E+11	4.0E+11	8.9E+11
$C_{15}H_9O_2\|i3 \rightarrow C_{15}H_9O_2\|i2$	2.3E-02	5.9E+01	6.5E+03
$C_{15}H_9O_2\|i3 \rightarrow C_{15}H_9O_2\|i4$	8.0E+08	5.3E+09	1.7E+10
$C_{15}H_9O_2\|i4 \rightarrow C_{15}H_9O_2\|i3$	1.3E+11	5.3E+11	1.2E+12
$C_{15}H_9O_2\|i4 \rightarrow C_{15}H_9O_2\|i5$	8.4E+10	4.2E+11	1.1E+12
$C_{15}H_9O_2\|i4 \rightarrow C_{15}H_9O_2\|i7$	1.5E+10	1.1E+11	3.4E+11

$C_{15}H_9O_2|i5 \rightarrow C_{15}H_9O_2|i4$	3.0E+10	5.4E+10	7.7E+10
$C_{15}H_9O_2|i5 \rightarrow C_{15}H_9O_2|i6$	4.1E+10	1.4E+11	3.0E+12
$C_{15}H_9O_2|i6 \rightarrow C_{15}H_9O_2|i5$	1.4E+09	1.2E+10	4.3E+10
$C_{15}H_9O_2|i6 \rightarrow C_{14}H_9 + CO_2$	2.7E+11	1.8E+12	5.6E+12
$C_{15}H_9O_2|i7 \rightarrow C_{15}H_9O_2|i4$	1.7E+06	8.1E+07	8.3E+08
$C_{15}H_9O_2|i7 \rightarrow C_{15}H_9O_2|i10$	5.6E+07	1.4E+09	1.0E+10
$C_{15}H_9O_2|i10 \rightarrow C_{15}H_9O_2|i7$	9.6E+09	3.5E+10	7.6E+10
$C_{15}H_9O_2|i10 \rightarrow C_{15}H_9O_2|i9$	1.3E+12	2.7E+12	4.1E+12
$C_{15}H_9O_2|i9 \rightarrow C_{15}H_9O_2|i10$	1.1E+12	1.9E+12	2.7E+12
$C_{15}H_9O_2|i9 \rightarrow C_{14}H_9 + CO_2$	7.0E+12	8.7E+12	9.8E+12

4.4 Summary

The energetics and kinetics for the oxidation of five-member rings by O_2 were investigated. The pathway to form $C_{14}H_9 + CO_2$ proved to be faster than the pathway to produce $C_{15}H_9O$ + O. The rate coefficients for the oxidation of both six- and five-member rings by O_2 were compared to rate coefficients published by Raj et al. [83] and found to be faster by over two orders of magnitude.

The reaction $C_{15}H_9 + O_2 \rightarrow C_{14}H_9 + CO_2$ and its calculated rate coefficient were added to the KMC oxidation model as reaction 90. The next chapter details the results of KMC simulations of graphene-edge oxidation by molecular oxygen that uncover kinetic features of the surface oxidation reaction model.

5 Detailed Kinetic Monte Carlo Simulations of Graphene-Edge Oxidation by Molecular Oxygen

In the previous two chapters, rate coefficients were calculated for elementary oxidation reactions. The reactions were assembled into a detailed model of graphene-edge oxidation by molecular oxygen. This chapter discusses the results of kinetic Monte Carlo (KMC) simulations of graphene-edge evolution in combustion-like environments that utilized the newly established model.

5.1 Introduction

KMC simulations were performed at temperatures of 1500, 2000, and 2500 K. Two scenarios were simulated: one with pure oxidation and one where oxidation competes with growth. In the latter scenario, the graphene layer was first grown from an initial coronene substrate for 5 ms and then O_2 was added to the gaseous environment to simulate oxidation that accompanies growth. The temperature was held constant in each simulation run. The pressure was held constant at 1 atm and the gas-phase composition was held constant with mole fractions $x_{C2H2} = x_{H2} = 0.1$ and $x_H = 0.01$. After O_2 was added, its concentration was also held constant. The pure oxidation scenario was similar to the oxidation-and-growth one, except that when O_2 was added after the initial 5 ms of growth, acetylene was removed, i.e., x_{C2H2} was set to 0. The two scenarios were designed to cover conditions encountered in hydrocarbon flames. The oxidation-and-growth simulations are discussed in Section 5.2, and the pure oxidation simulations are presented in Section 5.3.

For the KMC simulation results presented in this chapter, the model consisted of the first 90 reactions of Table 2.1 (45 growth and 45 oxidation reactions) and their corresponding rate coefficients. The last 14 oxidation reactions were added at a later time and their inclusion into the model is discussed in Chapter 7.

Simulations for each set of initial conditions were repeated 100 times, each with a different starting random seed. The results reported in this chapter are averages over these ensembles of simulations. With the primary focus on factors affecting oxidation, the present simulations all started with the same set of 100 grown substrates.

5.2 Oxidation-and-Growth Simulations

Time evolution of the substrate size and five-member ring fraction for a range of oxygen concentrations are depicted in Figure 5.1 for each temperature. The results computed for the substrate size, shown in the left-hand panels of Figure 5.1, demonstrate that as oxygen is added, oxidation begins to compete with growth, increasingly so with an increase in the amount of oxygen added and an increase in temperature. For instance, at the same level of

O$_2$ added (e.g., $x_{O2} = 1 \times 10^{-3}$), the growth of the graphene layer is only inhibited at 1500 and 2000 K but at 2500 K the layer decreases in size.
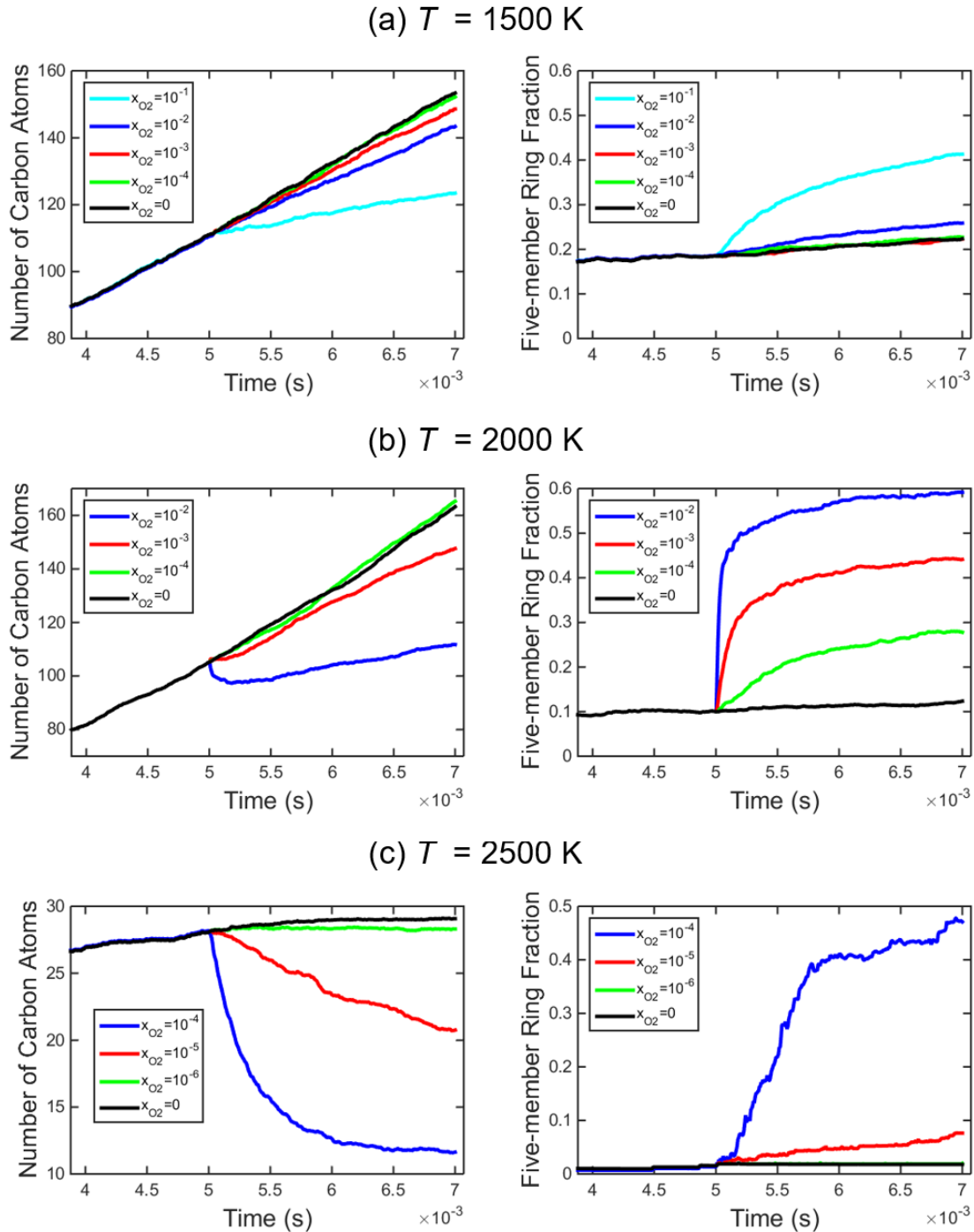
Figure 5.1. Substrate size (left) and five-member ring fraction (right) for the oxidation-and-growth simulations at temperatures (a) 1500 K, (b) 2000 K, and (c) 2500 K.

The computed five-member ring fractions, depicted in the right-hand panels of Figure 5.1, reveal that the addition of O_2 promotes the formation of five-member rings embedded in the graphene layer. To explain this observation, the reaction rates were studied by examining collected reaction statistics. Tables 5.1 – 5.3 show the average number of reaction events that occurred during the 2 ms oxidation-and-growth period for each set of simulations.

Table 5.1. Reaction counts for oxidation-and-growth simulations at 1500 K.

Reaction	x_{O2}				
	0	10^{-4}	10^{-3}	10^{-2}	10^{-1}
1	418.0	421.6	415.5	397.6	305.3
2	392.7	395.5	390.1	370.7	281.4
3	45.6	44.3	45.4	41.1	27.5
4	16.3	16.1	15.9	15.0	11.8
5	31.0	29.9	31.0	28.5	23.3
6	84.9	84.9	84.3	78.3	60.3
7	18.6	18.3	18.4	17.5	13.1
8	101.8	101.0	101.4	93.6	72.8
9	215.9	207.4	206.1	176.9	121.3
10	199.3	199.0	201.7	202.8	221.9
11	198.5	198.4	200.9	201.9	221.4
12	1762.2	1767.3	1777.3	1811.5	1982.0
13	1762.6	1767.6	1777.5	1810.5	1978.5
14	0.0	0.0	0.0	0.0	0.0
15	0.0	0.0	0.0	0.0	0.0
16	0.0	0.0	0.0	0.0	0.0
17	0.0	0.0	0.0	0.0	0.0
18	0.0	0.0	0.0	0.0	0.0
19	0.0	0.0	0.0	0.0	0.0
20	0.0	0.0	0.0	0.0	0.0
21	1.6	1.8	1.5	1.5	0.8
22	0.0	0.0	0.0	0.0	0.0
23	0.1	0.1	0.0	0.1	0.0
24	0.0	0.0	0.0	0.0	0.0
25	0.0	0.0	0.0	0.0	0.0
26	0.7	0.8	0.7	0.6	0.3
27	5.7	6.1	5.9	5.3	2.7
28	6.8	6.6	6.3	5.8	2.7
29	2.0	2.2	2.6	2.8	2.3
30	0.7	0.6	0.7	0.9	0.8
31	2.3	2.3	2.4	3.4	5.3
32	1.3	1.3	1.2	1.6	2.1
33	0.8	1.0	0.9	0.9	0.5

34	0.8	0.6	0.7	0.7	0.4
35	0.4	0.4	0.4	0.6	0.9
36	0.0	0.0	0.0	0.0	0.0
37	0.5	0.5	0.5	0.6	0.6
38	0.0	0.0	0.0	0.0	0.0
39	0.0	0.0	0.0	0.1	0.1
40	0.0	0.0	0.0	0.0	0.0
41	1.0	1.0	0.9	0.8	0.3
42	0.0	0.0	0.0	0.0	0.0
43	0.3	0.3	0.2	0.3	0.1
44	0.0	0.0	0.0	0.0	0.0
45	0.0	0.0	0.0	0.0	0.0
46	0.0	0.1	0.5	3.3	8.2
47	0.0	0.1	1.0	7.2	18.8
48	0.0	0.3	3.6	30.1	130.8
49	0.0	0.3	4.2	33.4	141.3
50	0.0	0.8	7.1	66.4	418.5
51	0.0	0.0	0.1	0.3	0.5
52	0.0	0.0	0.0	0.1	0.3
53	0.0	0.0	0.1	0.7	2.3
54	0.0	0.0	0.0	0.6	2.4
55	0.0	0.0	0.0	0.0	0.0
56	0.0	0.0	0.0	0.0	0.0
57	0.0	0.0	0.0	0.0	0.0
58	0.0	0.0	0.0	0.0	0.0
59	0.0	0.0	0.0	0.0	0.0
60	0.0	0.0	0.0	0.0	0.0
61	0.0	0.0	0.0	0.0	0.0
62	0.0	0.0	0.0	0.0	0.1
63	0.0	0.0	0.0	0.0	0.1
64	0.0	0.0	0.0	0.0	0.2
65	0.0	0.0	0.4	2.9	7.7
66	0.0	0.1	1.0	7.2	18.7
67	0.0	0.3	3.9	30.6	130.3
68	0.0	0.4	3.9	32.4	140.9
69	0.0	0.9	7.2	67.2	424.2
70	0.0	0.0	0.0	0.0	0.0
71	0.0	0.0	0.0	0.0	0.0
72	0.0	0.0	0.0	0.0	0.0
73	0.0	0.0	0.0	0.0	0.0
74	0.0	0.0	0.0	0.0	0.0
75	0.0	0.0	0.0	0.1	0.2
76	0.0	0.0	0.1	0.3	0.5
77	0.0	0.0	0.1	0.8	3.3
78	0.0	0.0	0.1	0.7	3.4

79	0.0	0.0	0.2	1.5	10.9
80	0.0	0.0	0.0	0.1	0.1
81	0.0	0.0	0.0	0.1	0.2
82	0.0	0.0	0.0	0.3	1.6
83	0.0	0.0	0.1	0.4	1.5
84	0.0	0.0	0.1	0.7	5.4
85	0.0	0.0	0.4	3.0	7.7
86	0.0	0.1	0.9	7.0	18.5
87	0.0	0.3	3.7	30.0	129.5
88	0.0	0.3	4.0	32.1	137.7
89	0.0	0.8	7.1	66.4	418.5
90	0.0	0.0	0.0	0.1	1.0

Table 5.2. Reaction counts for oxidation-and-growth simulations at 2000 K.

| Reaction | x_{O2} | | | |
	0	10^{-4}	10^{-3}	10^{-2}
1	1933.5	1483.6	945.3	740.1
2	1901.0	1423.1	873.1	670.2
3	502.2	353.8	178.0	94.2
4	220.4	165.9	105.8	81.2
5	548.3	393.1	221.2	145.5
6	385.1	276.8	135.2	73.2
7	185.7	132.1	65.5	35.8
8	695.4	492.4	244.9	131.8
9	198.0	134.1	61.4	26.1
10	16.8	92.9	283.5	388.6
11	16.5	92.0	281.2	386.3
12	38.5	210.0	637.1	895.6
13	37.9	207.1	632.5	888.6
14	0.0	0.0	0.0	0.0
15	0.1	0.1	0.0	0.0
16	0.1	0.4	0.3	0.7
17	0.0	0.2	0.2	0.3
18	0.0	0.0	0.0	0.0
19	0.0	0.0	0.0	0.0
20	0.0	0.0	0.0	0.0
21	11.8	6.8	1.7	0.7
22	0.0	0.1	0.1	0.1
23	10.1	5.0	1.2	0.7
24	20.7	12.6	5.2	4.5
25	5.6	3.3	1.3	1.2
26	27.7	16.2	6.7	5.8
27	16.7	19.1	12.2	5.2
28	4.8	5.1	2.9	1.0

29	0.1	0.9	0.9	1.4
30	1.8	5.6	6.6	3.6
31	1.3	13.1	21.8	21.5
32	1.0	4.1	7.8	9.6
33	0.3	0.3	0.9	0.8
34	0.3	0.8	2.3	2.3
35	1.1	4.1	7.2	11.3
36	0.0	0.0	0.0	0.0
37	0.1	0.6	0.7	0.5
38	0.0	0.0	0.0	0.0
39	0.0	0.0	0.0	0.0
40	0.0	0.0	0.1	0.0
41	2.0	2.9	1.9	0.6
42	0.0	0.0	0.0	0.0
43	0.6	0.7	0.4	0.2
44	0.0	0.0	0.0	0.0
45	0.0	0.0	0.0	0.0
46	0.0	0.0	0.1	0.2
47	0.0	0.1	0.2	0.5
48	0.0	2.7	6.6	10.2
49	0.0	3.0	6.6	11.1
50	0.0	5.9	31.4	141.3
51	0.0	0.0	0.1	0.2
52	0.0	0.1	0.2	0.4
53	0.0	2.3	5.4	9.2
54	0.0	2.4	5.5	8.5
55	0.0	0.0	0.0	0.0
56	0.0	0.0	0.0	0.0
57	0.0	0.0	0.0	0.0
58	0.0	0.0	0.0	0.0
59	0.0	0.0	0.0	0.0
60	0.0	0.0	0.0	0.0
61	0.0	0.0	0.0	0.1
62	0.0	0.2	0.3	0.7
63	0.0	0.2	0.5	0.6
64	0.0	2.6	13.2	59.9
65	0.0	0.0	0.0	0.0
66	0.0	0.1	0.0	0.2
67	0.0	0.5	1.6	2.3
68	0.0	0.8	1.5	2.4
69	0.0	8.6	44.8	201.7
70	0.0	0.0	0.0	0.0
71	0.0	0.0	0.0	0.0
72	0.0	0.0	0.0	0.1
73	0.0	0.0	0.0	0.0

74	0.0	0.1	0.6	2.7
75	0.0	0.0	0.0	0.0
76	0.0	0.0	0.0	0.0
77	0.0	0.0	0.1	0.2
78	0.0	0.1	0.1	0.1
79	0.0	0.5	2.5	11.0
80	0.0	0.0	0.0	0.0
81	0.0	0.0	0.0	0.0
82	0.0	0.0	0.1	0.2
83	0.0	0.0	0.1	0.1
84	0.0	0.5	2.3	10.5
85	0.0	0.0	0.0	0.0
86	0.0	0.0	0.0	0.1
87	0.0	0.4	1.2	1.7
88	0.0	0.4	1.1	1.8
89	0.0	5.8	30.7	138.7
90	0.0	0.0	0.0	0.1

Table 5.3. Reaction counts for oxidation-and-growth simulations at 2500 K.

	x_{O2}			
Reaction	0	10^{-6}	10^{-5}	10^{-4}
1	1828.1	1803.7	1654.3	1139.5
2	1827.8	1803.2	1654.6	1137.8
3	383.6	371.8	305.0	105.7
4	311.5	308.6	284.1	195.4
5	641.0	628.9	557.9	320.4
6	162.1	155.8	128.0	43.8
7	120.3	116.9	95.2	33.4
8	427.3	412.7	340.7	119.5
9	4.1	4.4	5.4	1.3
10	0.1	0.9	9.2	46.9
11	0.1	0.9	9.2	46.8
12	0.2	1.0	8.6	44.3
13	0.2	0.5	6.0	39.0
14	0.0	0.0	0.0	0.0
15	0.0	0.0	0.0	0.0
16	0.0	0.1	0.7	1.1
17	0.0	0.1	0.5	0.8
18	0.0	0.0	0.0	0.0
19	0.0	0.0	0.0	0.0
20	0.0	0.0	0.0	0.0
21	6.7	6.2	4.7	1.6
22	0.0	0.0	0.0	0.1
23	8.5	8.0	6.3	1.8

24	64.2	63.3	59.6	46.6
25	18.4	18.4	16.8	13.5
26	84.6	83.7	77.7	59.3
27	0.2	0.3	0.3	0.9
28	0.0	0.0	0.0	0.0
29	0.0	0.0	0.2	0.2
30	0.0	0.0	0.0	0.1
31	0.0	0.1	0.5	1.1
32	0.0	0.0	0.1	0.3
33	0.0	0.0	0.0	0.0
34	0.0	0.0	0.0	0.0
35	0.0	0.1	0.1	1.2
36	0.0	0.0	0.0	0.0
37	0.0	0.0	0.0	0.0
38	0.0	0.0	0.0	0.0
39	0.0	0.0	0.0	0.0
40	0.0	0.0	0.0	0.0
41	0.0	0.0	0.0	0.1
42	0.0	0.0	0.0	0.0
43	0.0	0.0	0.0	0.1
44	0.0	0.0	0.0	0.0
45	0.0	0.0	0.0	0.0
46	0.0	0.0	0.0	0.5
47	0.0	0.0	0.2	0.7
48	0.0	0.1	0.5	1.5
49	0.0	0.1	0.8	2.0
50	0.0	0.0	0.2	0.4
51	0.0	0.0	0.0	0.5
52	0.0	0.0	0.2	0.7
53	0.0	0.1	0.6	1.8
54	0.0	0.1	0.7	1.7
55	0.0	0.0	0.0	0.0
56	0.0	0.0	0.0	0.0
57	0.0	0.0	0.0	0.0
58	0.0	0.0	0.0	0.0
59	0.0	0.0	0.0	0.0
60	0.0	0.0	0.0	0.0
61	0.0	0.0	0.0	0.0
62	0.0	0.0	0.0	0.0
63	0.0	0.0	0.0	0.0
64	0.0	0.0	1.0	1.6
65	0.0	0.0	0.0	0.0
66	0.0	0.0	0.0	0.0
67	0.0	0.0	0.0	0.0
68	0.0	0.0	0.0	0.0

69	0.0	0.0	1.0	1.8
70	0.0	0.0	0.0	0.0
71	0.0	0.0	0.0	0.0
72	0.0	0.0	0.0	0.0
73	0.0	0.0	0.0	0.0
74	0.0	0.0	0.1	0.3
75	0.0	0.0	0.0	0.0
76	0.0	0.0	0.0	0.0
77	0.0	0.0	0.0	0.0
78	0.0	0.0	0.0	0.0
79	0.0	0.0	0.0	0.0
80	0.0	0.0	0.0	0.0
81	0.0	0.0	0.0	0.0
82	0.0	0.0	0.0	0.0
83	0.0	0.0	0.0	0.0
84	0.0	0.0	0.1	0.2
85	0.0	0.0	0.0	0.0
86	0.0	0.0	0.0	0.0
87	0.0	0.0	0.0	0.0
88	0.0	0.0	0.0	0.0
89	0.0	0.0	0.0	0.1
90	0.0	0.0	0.0	0.0

Analysis of the computed reaction fluxes indicated that the increase in the five-member rings is primarily due to their formation via thermal decomposition of oxyradicals (reactions 51–54). Excluding oxidation of five-member from the model results in faster saturation of the graphene edge with five-member rings, which prevents the graphene edge from further degradation (or growth).

The KMC results obtained in this oxidation-and-growth simulations revealed two major, competing pathways for an oxyradical originating in O_2 reaction with a surface radical. In the first pathways, the oxyradical undergoes thermal decomposition to form a five-member ring and expel CO—the actual oxidation step. In the second one, a neighboring-site H adds to the oxyradical forming OH, to which another H atom adds to expel H_2O and regenerate a new aromatic radical site—a pathways recycling the aromatic-radical site. Figure 5.2 shows a schematic diagram of the two pathways and Figure 5.3 quantifies the competition between these two pathways by comparing numbers of reaction events for the attack of O_2 on a radical site (reactions 46–50), thermal decomposition of an oxyradical (reactions 51–54), and regeneration of an aromatic radical site (reactions 85–89). For all three temperatures, the number of oxyradicals formed increases with an increase in oxygen concentration. At 1500 K, the regeneration pathway is dominant over the thermal-decomposition pathway. As the temperature increases to 2000 K, thermal decomposition begins to compete with regeneration, and at 2500 K thermal decomposition is the dominant pathway. This switch is a result of thermal decomposition being a higher activation-energy process than regeneration.
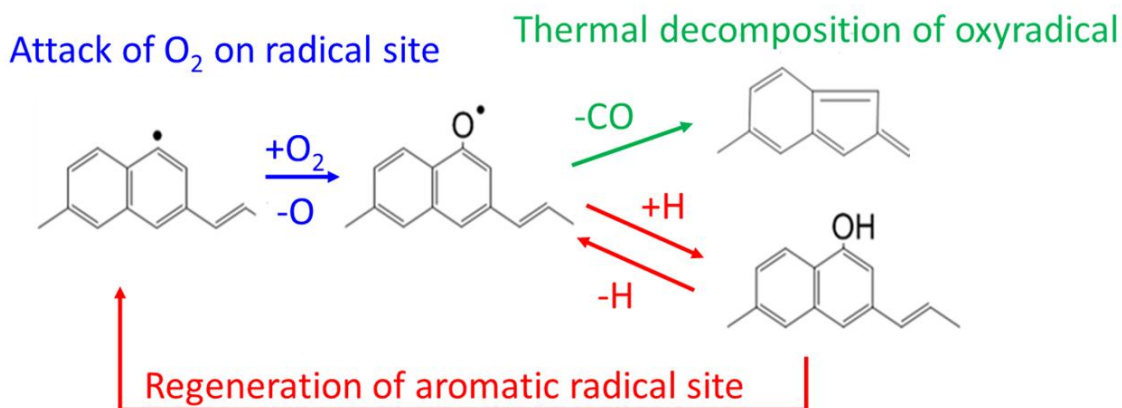
Figure 5.2. Diagram of two major pathways: Thermal decomposition of oxyradicals (green) and regeneration of an aromatic radical site (red).

Carbon is removed from the graphene edge either by thermal desorption (reactions 5, 7, 17, 25, and 45) or by oxidation (reactions 51–54). For all three temperatures studied, the reaction statistics show that as the concentration of oxygen increases, the frequency of oxidation reactions increases while the frequency of thermal desorption reactions decreases, indicating that competition exists between the two types of reactions. Although the frequency of thermal desorption decreased with an increasing oxygen concentration, the thermal desorption pathway still remained dominant over the oxidation pathway for all oxygen concentrations and temperatures tested. This result indicates that when growth reactions (3, 4, 26, 27, 33, 34, 35, 39, 42, and 44) added carbon atoms to the graphene layer, they were more likely to be removed by thermal desorption than oxidation, even for the highest oxygen concentrations.
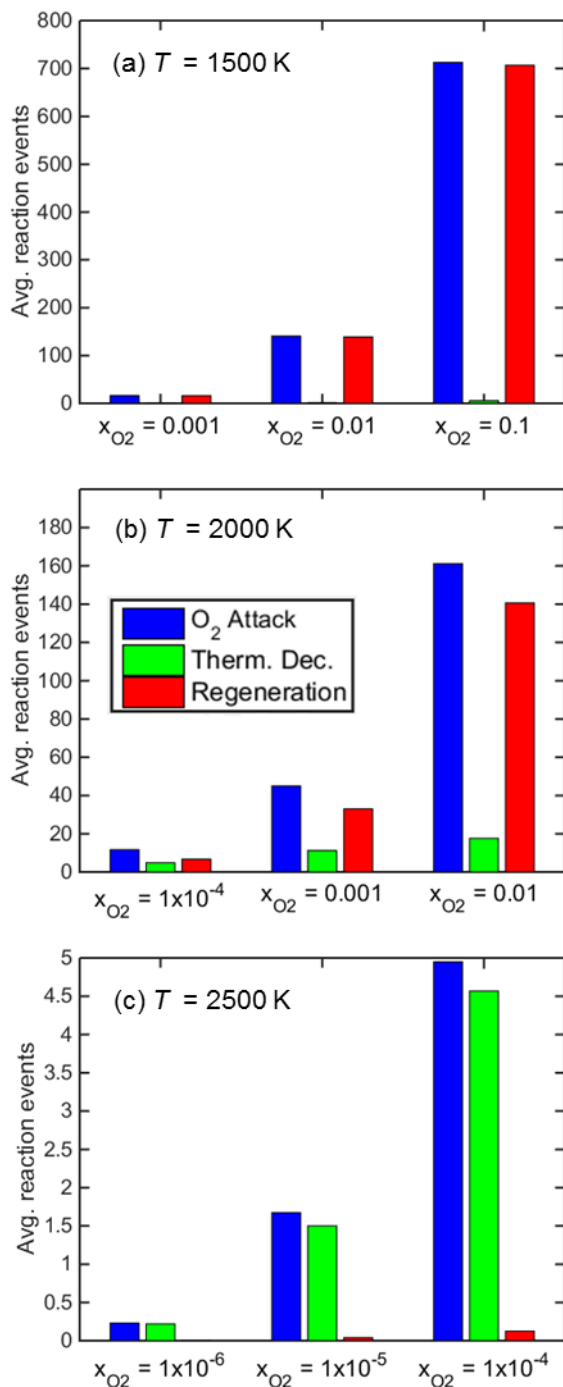
Figure 5.3. Reaction-event counts for O_2 attack on a radical site (blue), thermal decomposition of an oxyradical (green), and regeneration of an aromatic radical (red) for the oxidation-and-growth simulations.

Given that Chapter 4 was devoted to finding pathways and rate coefficients for the oxidation of five-member rings by O_2, a particular interest of the KMC simulations was to investigate the frequency of reaction 90, $C_{15}H_9 + O_2 \rightarrow C_{15}H_9O + O$. However, reaction

statistics revealed that reaction 90 occurs rather infrequently. For instance, at 1500 K and $x_{O2} = 0.1$, reaction 90 occurred 1.0 times, on average, per simulation, as compared to 23 and 13 counts for reactions 5 and 7, respectively. For lower O_2 concentrations, it did not happen. At 2000 K, reaction 90 occurred only 0.1 times per simulation with the highest O_2 concentration, and at 2500 K it did not occur at all.

5.3 Pure Oxidation Simulations

5.3.1 Principal Oxidation Pathways

This set of KMC simulations was performed at exactly the same conditions as the previous one, except that acetylene was removed from the gaseous environment at the time oxygen was added. Tables 5.4 – 5.6 show the reaction statistics collected for this set of simulations.

Table 5.4. Reaction counts for pure oxidation simulations at 1500 K.

| Reaction | x_{O2} | | | | |
	0	10^{-4}	10^{-3}	10^{-2}	10^{-1}
1	643.8	635.8	629.1	525.6	382.0
2	633.5	625.6	615.3	498.5	346.9
3	0.0	0.0	0.0	0.0	0.0
4	0.0	0.0	0.0	0.0	0.0
5	2.3	2.4	2.2	2.2	2.4
6	8.9	9.3	9.2	9.2	10.0
7	1.9	1.8	1.8	2.1	1.9
8	11.0	11.5	11.3	11.2	12.1
9	29.2	29.5	26.2	25.4	30.5
10	60.6	62.4	64.5	103.4	159.0
11	60.6	62.4	64.5	103.4	159.0
12	539.7	553.5	574.1	910.3	1428.9
13	539.2	553.1	573.0	907.3	1424.8
14	0.0	0.0	0.0	0.0	0.0
15	0.0	0.0	0.0	0.0	0.0
16	0.0	0.0	0.0	0.0	0.0
17	0.0	0.0	0.0	0.0	0.0
18	0.0	0.0	0.0	0.0	0.0
19	0.0	0.0	0.0	0.0	0.0
20	0.0	0.0	0.0	0.0	0.0
21	0.1	0.1	0.1	0.1	0.1
22	0.0	0.0	0.0	0.0	0.0
23	0.0	0.0	0.0	0.0	0.1
24	0.0	0.0	0.0	0.0	0.0
25	0.0	0.0	0.0	0.0	0.0
26	0.0	0.0	0.0	0.0	0.0

27	0.0	0.0	0.0	0.0	0.0
28	0.2	0.2	0.2	0.2	0.2
29	2.7	2.8	2.5	4.4	4.5
30	2.6	2.7	4.7	5.1	3.1
31	6.2	6.1	6.9	13.4	18.8
32	2.8	2.6	3.3	5.2	7.7
33	0.0	0.0	0.0	0.0	0.0
34	0.0	0.0	0.0	0.0	0.0
35	0.0	0.0	0.0	0.0	0.0
36	0.0	0.0	0.0	0.0	0.0
37	0.0	0.0	0.0	0.0	0.0
38	0.0	0.0	0.0	0.0	0.0
39	0.0	0.0	0.0	0.0	0.0
40	0.0	0.0	0.0	0.0	0.0
41	0.1	0.1	0.1	0.1	0.0
42	0.0	0.0	0.0	0.0	0.0
43	0.1	0.0	0.0	0.0	0.0
44	0.0	0.0	0.0	0.0	0.0
45	0.0	0.0	0.0	0.0	0.0
46	0.0	0.1	0.8	4.3	5.1
47	0.0	0.1	1.9	10.3	13.6
48	0.0	1.3	13.4	77.4	122.8
49	0.0	1.5	13.2	77.8	126.0
50	0.0	1.5	14.9	105.1	520.4
51	0.0	0.0	0.0	0.3	0.3
52	0.0	0.0	0.0	0.1	0.2
53	0.0	0.0	0.2	1.4	2.6
54	0.0	0.0	0.3	1.3	2.1
55	0.0	0.0	0.0	0.0	0.0
56	0.0	0.0	0.0	0.0	0.0
57	0.0	0.0	0.0	0.0	0.0
58	0.0	0.0	0.0	0.0	0.0
59	0.0	0.0	0.0	0.0	0.0
60	0.0	0.0	0.0	0.0	0.0
61	0.0	0.0	0.0	0.0	0.0
62	0.0	0.0	0.0	0.0	0.0
63	0.0	0.0	0.0	0.1	0.1
64	0.0	0.0	0.0	0.0	0.1
65	0.0	0.1	0.8	4.1	5.0
66	0.0	0.1	1.9	10.4	13.3
67	0.0	1.5	13.9	77.0	122.9
68	0.0	1.4	12.9	77.6	124.6
69	0.0	1.4	15.1	106.6	526.0
70	0.0	0.0	0.0	0.0	0.0
71	0.0	0.0	0.0	0.0	0.0

72	0.0	0.0	0.0	0.0	0.0
73	0.0	0.0	0.0	0.0	0.0
74	0.0	0.0	0.0	0.0	0.0
75	0.0	0.0	0.0	0.1	0.1
76	0.0	0.0	0.0	0.3	0.2
77	0.0	0.0	0.4	2.0	3.1
78	0.0	0.1	0.5	2.1	3.4
79	0.0	0.0	0.4	2.8	12.6
80	0.0	0.0	0.0	0.0	0.0
81	0.0	0.0	0.0	0.2	0.2
82	0.0	0.0	0.1	1.0	1.5
83	0.0	0.0	0.1	1.0	1.6
84	0.0	0.1	0.2	1.3	7.1
85	0.0	0.1	0.8	4.0	4.8
86	0.0	0.1	1.8	10.3	13.3
87	0.0	1.4	13.1	75.8	122.3
88	0.0	1.4	13.0	76.7	121.8
89	0.0	1.5	14.9	105.1	520.2
90	0.0	0.0	0.0	0.0	0.1

Table 5.5. Reaction counts for pure oxidation simulations at 2000 K.

	x_{O_2}			
Reaction	0	10^{-4}	10^{-3}	10^{-2}
1	1735.9	1527.1	879.3	771.8
2	1731.0	1444.1	830.9	738.8
3	0.0	0.0	0.0	0.0
4	0.0	0.0	0.0	0.0
5	0.0	2.3	4.3	3.8
6	0.0	1.1	2.6	2.8
7	0.0	0.6	1.2	1.2
8	0.0	1.6	4.4	4.2
9	0.0	0.3	0.7	0.3
10	7.6	176.3	302.5	335.3
11	7.6	176.3	302.5	335.2
12	18.8	405.7	703.3	759.6
13	18.8	401.3	695.2	752.1
14	0.0	0.0	0.0	0.0
15	0.0	0.1	0.1	0.0
16	0.0	0.6	1.3	1.1
17	0.0	0.2	0.6	0.7
18	0.0	0.0	0.0	0.0
19	0.0	0.0	0.0	0.0
20	0.0	0.0	0.0	0.0
21	0.0	0.1	0.2	0.2

22	0.0	0.0	0.1	0.0
23	0.0	0.1	0.1	0.2
24	0.0	0.1	0.1	0.1
25	0.0	0.0	0.0	0.0
26	0.0	0.0	0.0	0.0
27	0.0	0.0	0.0	0.0
28	0.0	0.0	0.0	0.0
29	0.0	1.6	2.3	1.8
30	2.6	32.0	6.0	5.0
31	1.5	33.1	27.1	16.7
32	0.6	15.2	12.1	7.8
33	0.0	0.0	0.0	0.0
34	0.0	0.0	0.0	0.0
35	0.0	0.0	0.0	0.0
36	0.0	0.0	0.0	0.0
37	0.0	0.0	0.0	0.0
38	0.0	0.0	0.0	0.0
39	0.0	0.0	0.0	0.0
40	0.0	0.0	0.0	0.0
41	0.0	0.0	0.0	0.0
42	0.0	0.0	0.0	0.0
43	0.0	0.0	0.1	0.1
44	0.0	0.0	0.0	0.0
45	0.0	0.0	0.0	0.0
46	0.0	0.1	0.3	0.1
47	0.0	0.2	0.7	0.6
48	0.0	3.0	3.7	3.8
49	0.0	2.3	3.4	4.0
50	0.0	5.0	9.7	29.3
51	0.0	0.1	0.2	0.1
52	0.0	0.2	0.6	0.5
53	0.0	2.2	3.3	3.2
54	0.0	2.0	3.0	3.2
55	0.0	0.0	0.0	0.0
56	0.0	0.0	0.0	0.0
57	0.0	0.0	0.0	0.0
58	0.0	0.0	0.0	0.0
59	0.0	0.0	0.0	0.0
60	0.0	0.0	0.0	0.0
61	0.0	0.0	0.2	0.2
62	0.0	0.1	0.3	0.3
63	0.0	0.1	0.3	0.3
64	0.0	1.8	4.4	13.7
65	0.0	0.0	0.1	0.0
66	0.0	0.0	0.3	0.3

67	0.0	0.8	0.5	0.9
68	0.0	0.5	0.8	1.1
69	0.0	6.8	14.1	43.1
70	0.0	0.0	0.0	0.0
71	0.0	0.0	0.0	0.0
72	0.0	0.0	0.0	0.0
73	0.0	0.0	0.0	0.0
74	0.0	0.1	0.3	0.7
75	0.0	0.0	0.0	0.0
76	0.0	0.0	0.1	0.0
77	0.0	0.0	0.0	0.0
78	0.0	0.0	0.1	0.0
79	0.0	0.4	0.8	1.9
80	0.0	0.0	0.0	0.0
81	0.0	0.0	0.0	0.1
82	0.0	0.1	0.0	0.0
83	0.0	0.0	0.1	0.0
84	0.0	0.4	0.8	1.9
85	0.0	0.0	0.1	0.0
86	0.0	0.0	0.1	0.1
87	0.0	0.7	0.4	0.6
88	0.0	0.4	0.5	0.7
89	0.0	4.9	9.4	28.6
90	0.0	0.0	0.0	0.0

Table 5.6. Reaction counts for pure oxidation simulations at 2500 K.

	x_{O_2}			
Reaction	0	10^{-6}	10^{-5}	10^{-4}
1	1963.5	1947.6	1749.0	1154.3
2	1964.5	1948.5	1749.1	1156.7
3	0.0	0.0	0.0	0.0
4	0.0	0.0	0.0	0.0
5	1.1	1.3	3.6	6.2
6	0.3	0.4	0.7	0.9
7	0.1	0.1	0.5	0.8
8	0.3	0.5	1.8	2.9
9	0.0	0.0	0.0	0.0
10	0.0	1.8	12.0	47.0
11	0.0	1.8	12.0	47.0
12	0.0	1.9	11.4	44.4
13	0.0	1.5	8.5	39.4
14	0.0	0.0	0.0	0.0
15	0.0	0.0	0.0	0.0
16	0.0	0.1	0.7	1.0

17	0.0	0.1	0.5	0.9
18	0.0	0.0	0.0	0.0
19	0.0	0.0	0.0	0.0
20	0.0	0.0	0.0	0.0
21	0.0	0.0	0.0	0.0
22	0.0	0.0	0.0	0.0
23	0.0	0.0	0.0	0.0
24	0.0	0.0	0.3	0.9
25	0.0	0.0	0.1	0.3
26	0.0	0.0	0.0	0.0
27	0.0	0.0	0.0	0.0
28	0.0	0.0	0.0	0.0
29	0.0	0.0	0.2	0.3
30	0.0	0.0	0.1	0.0
31	0.0	0.4	1.4	0.6
32	0.0	0.1	0.6	0.2
33	0.0	0.0	0.0	0.0
34	0.0	0.0	0.0	0.0
35	0.0	0.0	0.0	0.0
36	0.0	0.0	0.0	0.0
37	0.0	0.0	0.0	0.0
38	0.0	0.0	0.0	0.0
39	0.0	0.0	0.0	0.0
40	0.0	0.0	0.0	0.0
41	0.0	0.0	0.0	0.0
42	0.0	0.0	0.0	0.0
43	0.0	0.0	0.0	0.0
44	0.0	0.0	0.0	0.0
45	0.0	0.0	0.0	0.0
46	0.0	0.0	0.1	0.3
47	0.0	0.0	0.2	0.6
48	0.0	0.1	0.8	1.3
49	0.0	0.1	0.6	1.2
50	0.0	0.0	0.1	0.2
51	0.0	0.0	0.1	0.3
52	0.0	0.0	0.2	0.6
53	0.0	0.1	0.6	1.2
54	0.0	0.1	0.8	1.3
55	0.0	0.0	0.0	0.0
56	0.0	0.0	0.0	0.0
57	0.0	0.0	0.0	0.0
58	0.0	0.0	0.0	0.0
59	0.0	0.0	0.0	0.0
60	0.0	0.0	0.0	0.0
61	0.0	0.0	0.0	0.0

62	0.0	0.0	0.0	0.0
63	0.0	0.0	0.0	0.0
64	0.0	0.1	0.6	1.1
65	0.0	0.0	0.0	0.0
66	0.0	0.0	0.0	0.0
67	0.0	0.0	0.0	0.0
68	0.0	0.0	0.0	0.0
69	0.0	0.1	0.7	1.1
70	0.0	0.0	0.0	0.0
71	0.0	0.0	0.0	0.0
72	0.0	0.0	0.0	0.0
73	0.0	0.0	0.0	0.0
74	0.0	0.0	0.1	0.2
75	0.0	0.0	0.0	0.0
76	0.0	0.0	0.0	0.0
77	0.0	0.0	0.0	0.0
78	0.0	0.0	0.0	0.0
79	0.0	0.0	0.0	0.0
80	0.0	0.0	0.0	0.0
81	0.0	0.0	0.0	0.0
82	0.0	0.0	0.0	0.0
83	0.0	0.0	0.0	0.0
84	0.0	0.0	0.1	0.2
85	0.0	0.0	0.0	0.0
86	0.0	0.0	0.0	0.0
87	0.0	0.0	0.0	0.0
88	0.0	0.0	0.0	0.0
89	0.0	0.0	0.0	0.0
90	0.0	0.0	0.0	0.0

Figure 5.4 displays the time evolution of the substrate size and five-member ring fraction for each temperature and for a range of oxygen concentrations. There is no growth to compete with oxidation in these simulations, so the addition of any amount of oxygen leads to a decrease in the size of the graphene layer. Other than that, the results displayed in Figure 5.4 are similar to those of the discussed above oxidation-and-growth case. Also similar are the major competition pathways of thermal decomposition and regeneration, as shown in Figure 5.2 and exemplified by reaction-event counts in Figure 5.5, as well as the relative frequency of reaction 90.

In the pure oxidation simulations, the frequency of thermal-desorption reactions was over an order of magnitude lower than in the oxidation-and-growth cases because acetylene was not present in the gaseous environment during oxidation and hence lower occurrence on the graphene edge of lone adsorbates able to desorb. Unlike for the oxidation-and-growth cases, at 1500 K the oxidation pathway became dominant over thermal desorption for the highest oxygen concentration, $x_{O_2} = 0.1$. At 2000 K, oxidation dominated thermal

desorption for $x_{O2} > 10^{-4}$. Still, similar to the oxidation-and-growth cases, at 2500 K, the thermal desorption reactions were dominant over the oxidation ones for all concentrations of oxygen studied.

Similarly to the oxidation-and-growth case, the graphene edge became "non-reactive" quicker when the five-member-ring oxidation was excluded from the simulation. Such "non-reactive" sites are illustrated in Figure 5.6, which displays two snapshots from an oxidation-only KMC simulation at 2000 K and $x_{O2} = 0.001$. The snapshot shown on the left-hand side of the figure is taken at a simulation time of 5 ms, at the instant when C_2H_2 is removed from and O_2 is added to the gaseous environment. The green box exemplifies that before the oxidizer is added, the edge consists of six-member rings with a "free" corner thus enabling a zipper oxidation [35, 36]. The right-hand side of the figure depicts a structure formed after 1.8 ms of the oxidation period. The red pentagons drawn over the structure highlight some of the five-member rings of the graphene edge. If not removed, the highlighted five-member rings prevent further oxidation from occurring. As seen earlier in Section 5.2, even when the five-member-ring oxidation reaction is included, its rate is relatively low and hence may not prevent the buildup of five-member rings.
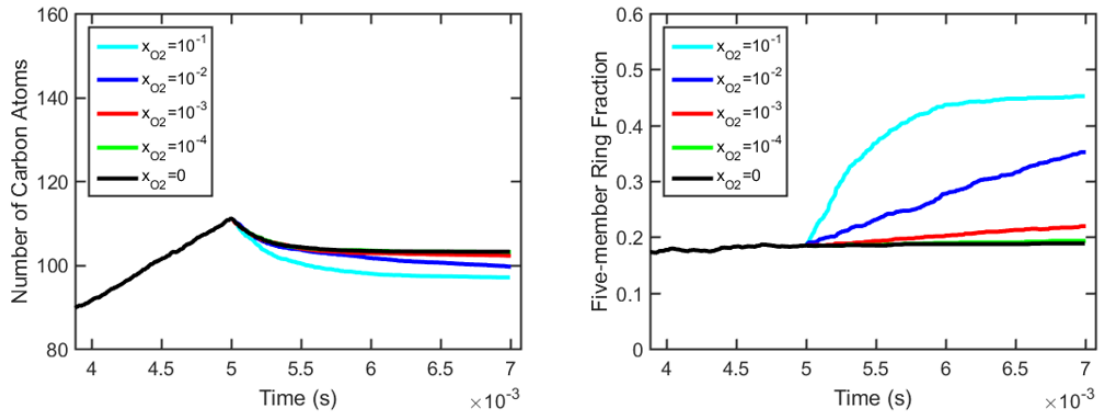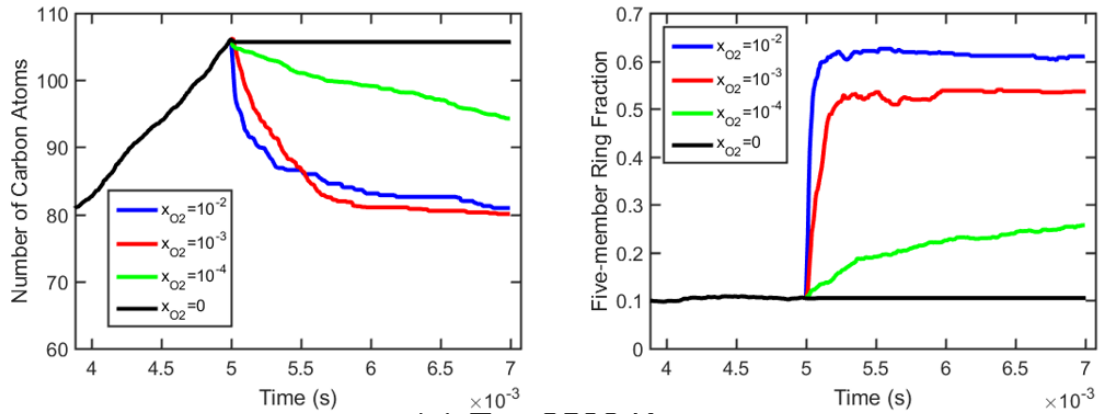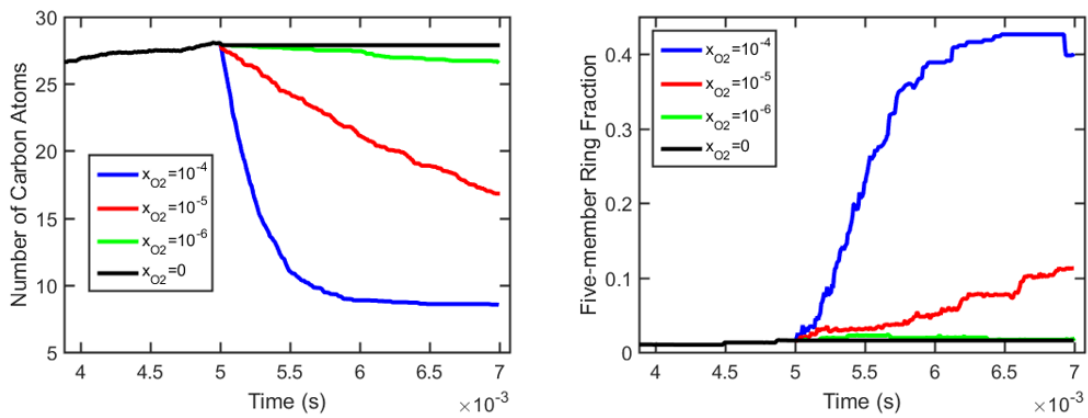
Figure 5.4. Substrate size (left) and five-member ring fraction (right) for the oxidation-only simulations at temperatures (a) 1500 K, (b) 2000 K, and (c) 2500 K.
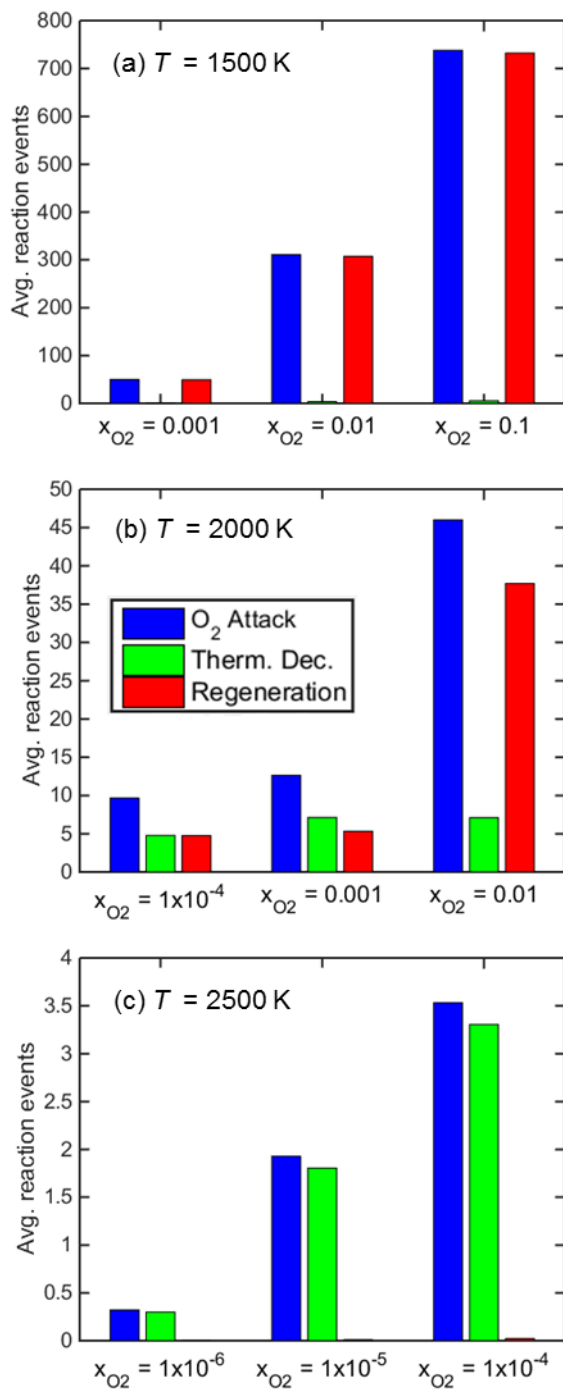
Figure 5.5. Reaction-event counts for O_2 attack on a radical site (blue), thermal decomposition of an oxyradical (green), and regeneration of an aromatic radical site (red) for the oxidation-only simulations.

(a) $t = 5$ ms   (b) $t = 6.8$ ms
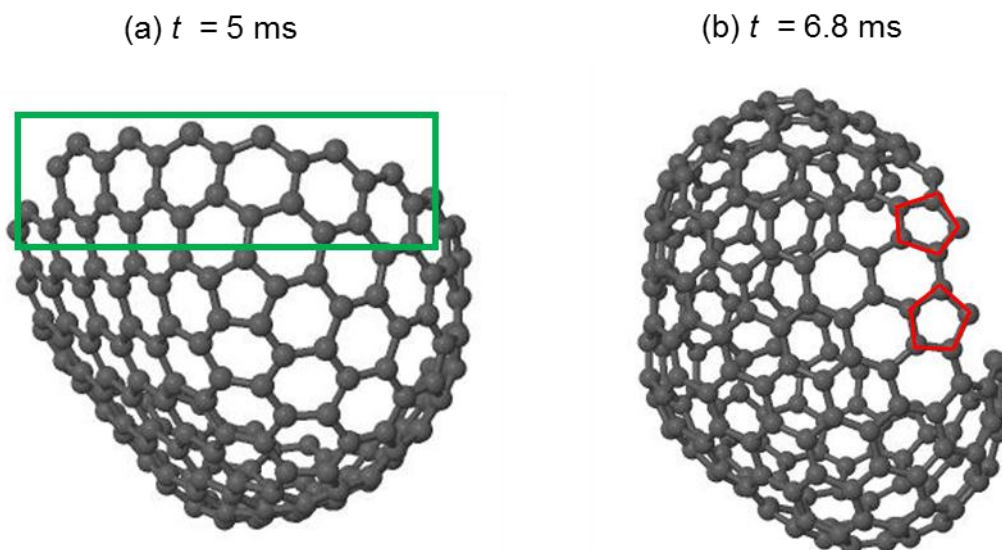
Figure 5.6.   Representative structures seen in the oxidation-only simulations. The displayed snapshot are from a KMC simulation at 2000 K and $x_{O_2} = 0.001$: (a) at the end of the growth period and just before the onset of oxidation, (b) after 1.8 ms of the oxidation. The H atoms saturating the edge carbon atoms are not shown for clarity.

5.3.2 Effect of Regeneration on the Rate of Oxidation

In the previous subsection, the oxidation and regeneration pathways were said to compete for oxyradicals formed by the attack of O_2 on surface radical sites. While the relative rates of the two pathways switch dramatically in the temperature range studied, the influence of the regenerative pathway on the overall, bulk oxidation rate is not very large. Table 5.7 reports the bulk oxidation rates obtained in additional KMC runs, performed at the same conditions as those in Section 5.3.1 but with regeneration pathways excluded from the simulations.

Table 5.7. Oxidation rates (C-atom/ms) computed with and without regeneration pathway included.

Temperature (K)	1500			2000			2500		
x_{O_2}	10^{-3}	10^{-2}	10^{-1}	10^{-4}	10^{-3}	10^{-2}	10^{-6}	10^{-5}	10^{-4}
With	24.5	26.6	36.4	15.3	45.0	54.1	7.0	10.2	49.7
Without	27.2	29.8	36.4	18.6	53.8	54.1	7.0	10.2	49.7

At 1500 K, the initial oxidation rates increase by up to 12 % when regeneration was excluded. In spite of the dominant pathway for oxyradicals at 1500 K being the regeneration pathway, excluding the regeneration reactions leads only to a marginal increase in the frequency of oxidation of six- and five-member rings and hence only a

marginal increase in the oxidation rates. In other words, at these conditions the fast regeneration reactions simply recycle the aromatic oxyradicals. The results at 2000 K are similar to those at 1500 K with the oxidation rates increasing by up to 21 % for the simulations without regeneration. At 2500 K, there is no change in the oxidation rates when regeneration reactions are excluded, because the oxidation pathway is already completely dominant over the regeneration pathway at this high temperature. The reaction event counts for these simulations are presented in Tables 5.8 – 5.10.

The fact that regeneration does not affect greatly the bulk oxidation rate may help in developing reduced models of soot oxidation at flame conditions.

Table 5.8. Reaction counts for pure oxidation simulations without regeneration pathway at 1500 K.

Reaction	x_{O_2}				
	0	10^{-4}	10^{-3}	10^{-2}	10^{-1}
1	643.8	572.5	388.3	306.2	301.8
2	633.5	553.6	361.9	286.7	282.4
3	0.0	0.0	0.0	0.0	0.0
4	0.0	0.0	0.0	0.0	0.0
5	2.3	2.3	2.7	2.3	2.5
6	8.9	9.5	9.6	9.8	8.3
7	1.9	1.9	1.9	2.3	2.0
8	11.0	11.6	12.0	11.9	10.7
9	29.2	29.4	22.9	17.3	11.4
10	60.6	78.2	101.6	87.3	80.6
11	60.6	78.2	101.5	87.3	80.6
12	539.7	689.5	904.6	772.7	718.0
13	539.2	688.0	897.8	771.4	717.1
14	0.0	0.0	0.0	0.0	0.0
15	0.0	0.0	0.0	0.0	0.0
16	0.0	0.0	0.0	0.0	0.0
17	0.0	0.0	0.0	0.0	0.0
18	0.0	0.0	0.0	0.0	0.0
19	0.0	0.0	0.0	0.0	0.0
20	0.0	0.0	0.0	0.0	0.0
21	0.1	0.1	0.0	0.1	0.1
22	0.0	0.0	0.0	0.0	0.0
23	0.0	0.0	0.0	0.0	0.0
24	0.0	0.0	0.0	0.0	0.0
25	0.0	0.0	0.0	0.0	0.0
26	0.0	0.0	0.0	0.0	0.0
27	0.0	0.0	0.0	0.0	0.0
28	0.2	0.2	0.1	0.1	0.1
29	2.7	3.2	3.8	3.6	3.7

30	2.6	3.3	2.1	0.2	0.8
31	6.2	9.2	10.5	5.9	5.8
32	2.8	4.2	4.8	2.8	2.5
33	0.0	0.0	0.0	0.0	0.0
34	0.0	0.0	0.0	0.0	0.0
35	0.0	0.0	0.0	0.0	0.0
36	0.0	0.0	0.0	0.0	0.0
37	0.0	0.0	0.1	0.0	0.0
38	0.0	0.0	0.0	0.0	0.0
39	0.0	0.0	0.0	0.0	0.0
40	0.0	0.0	0.0	0.0	0.0
41	0.1	0.1	0.1	0.0	0.1
42	0.0	0.0	0.0	0.0	0.0
43	0.1	0.0	0.0	0.0	0.0
44	0.0	0.0	0.0	0.0	0.0
45	0.0	0.0	0.0	0.0	0.0
46	0.0	0.0	0.1	0.2	0.1
47	0.0	0.2	0.3	0.3	0.3
48	0.0	0.8	1.9	2.1	2.3
49	0.0	0.9	1.9	1.5	1.0
50	0.0	1.2	5.1	7.2	7.8
51	0.0	0.0	0.1	0.2	0.1
52	0.0	0.1	0.3	0.2	0.2
53	0.0	0.6	1.5	0.6	0.3
54	0.0	0.6	1.2	1.1	0.9
90	0.0	0.0	0.0	0.0	0.0

Table 5.9. Reaction counts for pure oxidation simulations without regeneration pathway at 2000 K.

	x_{O_2}			
Reaction	0	10^{-4}	10^{-3}	10^{-2}
1	1735.9	1441.2	808.5	763.0
2	1731.0	1376.3	772.6	717.1
3	0.0	0.0	0.0	0.0
4	0.0	0.0	0.0	0.0
5	0.0	2.7	3.5	2.5
6	0.0	1.7	2.9	2.0
7	0.0	0.7	1.2	0.8
8	0.0	2.3	4.1	2.6
9	0.0	0.6	0.5	0.4
10	7.6	163.5	322.6	336.5
11	7.6	163.4	322.5	336.4
12	18.8	375.5	733.1	764.3
13	18.8	371.3	726.1	759.0

14	0.0	0.0	0.0	0.0
15	0.0	0.0	0.0	0.0
16	0.0	0.7	1.0	0.7
17	0.0	0.2	0.6	0.4
18	0.0	0.0	0.0	0.0
19	0.0	0.0	0.0	0.0
20	0.0	0.0	0.0	0.0
21	0.0	0.1	0.1	0.0
22	0.0	0.0	0.1	0.0
23	0.0	0.1	0.1	0.0
24	0.0	0.1	0.1	0.0
25	0.0	0.0	0.1	0.0
26	0.0	0.0	0.0	0.0
27	0.0	0.0	0.0	0.0
28	0.0	0.0	0.0	0.0
29	0.0	1.5	1.7	1.4
30	2.6	21.3	3.7	8.7
31	1.5	30.6	21.0	27.8
32	0.6	13.8	11.1	11.7
33	0.0	0.0	0.0	0.0
34	0.0	0.0	0.0	0.0
35	0.0	0.0	0.0	0.0
36	0.0	0.0	0.0	0.0
37	0.0	0.0	0.0	0.0
38	0.0	0.0	0.0	0.0
39	0.0	0.0	0.0	0.0
40	0.0	0.0	0.0	0.0
41	0.0	0.0	0.0	0.0
42	0.0	0.0	0.0	0.0
43	0.0	0.0	0.0	0.0
44	0.0	0.0	0.0	0.0
45	0.0	0.0	0.0	0.0
46	0.0	0.1	0.3	0.0
47	0.0	0.1	0.3	0.1
48	0.0	2.4	3.5	2.8
49	0.0	1.8	2.6	2.6
50	0.0	4.5	4.8	74.7
51	0.0	0.1	0.3	0.1
52	0.0	0.1	0.3	0.1
53	0.0	2.3	3.1	3.2
54	0.0	2.0	3.2	2.5
90	0.0	0.0	0.0	0.0

Table 5.10.   Reaction counts for pure oxidation simulations without regeneration pathway at 2500 K.

Reaction	x_{O_2}			
	0	10^{-6}	10^{-5}	10^{-4}
1	1963.5	1948.3	1747.2	1159.1
2	1964.5	1947.2	1746.7	1161.0
3	0.0	0.0	0.0	0.0
4	0.0	0.0	0.0	0.0
5	1.1	1.3	3.6	6.2
6	0.3	0.4	0.7	1.0
7	0.1	0.1	0.5	0.8
8	0.3	0.5	1.8	3.0
9	0.0	0.0	0.0	0.1
10	0.0	1.8	12.0	47.0
11	0.0	1.8	12.0	47.0
12	0.0	1.9	11.4	44.4
13	0.0	1.5	8.5	39.5
14	0.0	0.0	0.0	0.0
15	0.0	0.0	0.0	0.0
16	0.0	0.1	0.7	1.0
17	0.0	0.1	0.5	0.9
18	0.0	0.0	0.0	0.0
19	0.0	0.0	0.0	0.0
20	0.0	0.0	0.0	0.0
21	0.0	0.0	0.0	0.0
22	0.0	0.0	0.0	0.0
23	0.0	0.0	0.0	0.0
24	0.0	0.0	0.3	0.9
25	0.0	0.0	0.1	0.3
26	0.0	0.0	0.0	0.0
27	0.0	0.0	0.0	0.0
28	0.0	0.0	0.0	0.0
29	0.0	0.0	0.2	0.3
30	0.0	0.0	0.1	0.0
31	0.0	0.4	1.4	0.6
32	0.0	0.1	0.6	0.2
33	0.0	0.0	0.0	0.0
34	0.0	0.0	0.0	0.0
35	0.0	0.0	0.0	0.0
36	0.0	0.0	0.0	0.0
37	0.0	0.0	0.0	0.0
38	0.0	0.0	0.0	0.0
39	0.0	0.0	0.0	0.0
40	0.0	0.0	0.0	0.0

41	0.0	0.0	0.0	0.0
42	0.0	0.0	0.0	0.0
43	0.0	0.0	0.0	0.0
44	0.0	0.0	0.0	0.0
45	0.0	0.0	0.0	0.0
46	0.0	0.0	0.1	0.3
47	0.0	0.0	0.2	0.6
48	0.0	0.1	0.8	1.3
49	0.0	0.1	0.6	1.2
50	0.0	0.0	0.1	0.2
51	0.0	0.0	0.1	0.3
52	0.0	0.0	0.2	0.6
53	0.0	0.1	0.6	1.2
54	0.0	0.1	0.8	1.3
90	0.0	0.0	0.0	0.0

5.3.3 Reactivity of Graphene Edges with Embedded Five-Member Rings

The results of Section 5.3.1 indicate that accumulation of five-member rings at the graphene edge leads to its reduced reactivity. This is manifested by the decaying rates of graphene-edge oxidation. Indeed, as can be seen in Figure 5.4, the profiles of the substrate size during the oxidation are non-linear in time, implying time-varying—decaying—rates of oxidation. Since the gaseous environment is maintained unchanged during an individual simulation, the only varying property affecting the rate of oxidation is the edge density of reactive sites and their reactivity towards oxidation.

The notion that incorporation of five-member rings into graphene edges makes it less reactive is counter intuitive at first, as five-member rings are usually considered to be less stable [21, 81, 84]. To explain the computed behavior, one must consider the morphology of the graphene edge. Fundamentally, a graphene edge can be in two forms, armchair and zigzag. At combustion conditions it is presumed that all edge sites are saturated with H atoms and reaction is initiated by abstracting an H atom forming a surface radical [11, 13, 14, 85]. Left to growth only, a finite-size armchair edge evolves quickly into zigzag edges [15]. Zigzag edges can also grow, rate-limited by surface nucleation occurring either at edge corners or though chemisorbed and migrating five-member rings [21], both slower than the growth of armchair edges (via the HACA mechanism [11, 85], for example).

Oxidation is essentially controlled by decomposition of surface oxyradicals. A six-member-ring oxyradical decomposes by expelling CO and forming a five-member ring [26]. Recent theoretical studies of elementary reactions concluded that inner zigzag oxyradical sites decompose much slower, if at all, than corner zigzag and armchair sites at combustion conditions [35, 36]. These results imply that armchair-edge oxidation should proceed as random removal of individual edge sites while that of zigzag edges as a zipper-type reaction process. Literature is rather conflicting on comparison of armchair and zigzag oxidation reactivity. For instance, the early microscopy work of Thomas and

Hughes [86] reported slightly higher recession rates of zigzag than armchair edges, yet more recent consensus is that armchair carbon atoms are more reactive than zigzag ones [87]. Also, the close proximity in numerical measures of reactivity (e.g., those observed by Thomas and Hughes) for the two edges could be consistent with the theoretical predictions that the oxidation (and growth [53]) rates of armchair and corner zigzag sites are close to each other, and the difference in experimentally observed edge evolution is due to cooperative phenomena of elementary reaction steps and edge geometry.

Returning to the present simulations, graphene edges formed in the growth period are both zigzag and armchair, as illustrated in Figure 5.7a. When the oxidation period begins, the zigzag sites remain largely intact and the armchair sites convert into five-member rings, as can be seen by comparison between the edge fragment enclosed in the green box in Figure 5.7a with the corresponding red-marked edge fragment in Figure 5.7b.
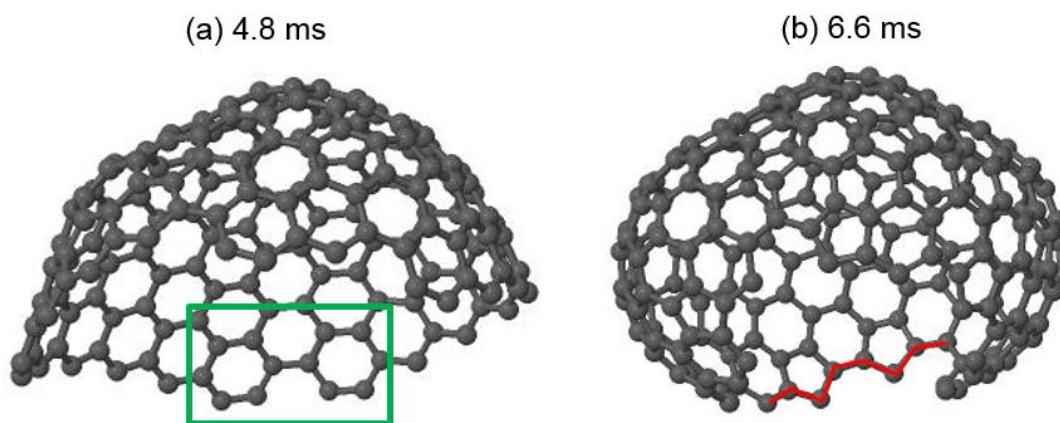
Figure 5.7. Graphene structures obtained in a KMC simulation at 2000 K and $x_{O_2} = 0.001$ (a) toward the end of the growth period, just before the onset of oxidation, and (b) after 1.6 ms of oxidation. The H atoms saturating the edge carbon atoms are not shown for clarity.

While the emerged red-marked fragment with embedded five-member rings is not a zigzag edge fragment, it is also not an armchair. Analysis of oxidation pathways for such embedded five-member rings yielded rates substantially higher than those of inner zigzag sites [36] but much (over four orders of magnitude) lower than those for six-member rings of an armchair edge [81, 82].

The phenomenon of decreasing oxidative reactivity of soot over time has been observed experimentally. In a study by Vander Wal and co-workers [88], soot samples were collected from diesel particulate filters after different kinds of engine testing, and the nanostructure of primary particles within the aggregates was observed using HRTEM imaging. They found that samples with longer exposure to oxidation conditions had a higher fraction of densified particles than samples collected over limited-time low-load conditions. The authors [88] explained that the densification occurred because oxidation preferentially removed amorphous carbon relative to graphitic carbon causing a decrease in the number of reactive edge-site carbon atoms relative to the number of more stable

basal-plane carbon atoms and, hence, a decrease in oxidative reactivity.   Similar observations were reported by Jaramillo et al. [89] and Fang and Lance [90].

In the present KMC simulations, a similar decrease was observed in the ratio of reactive edge sites to basal-plane carbon atoms during oxidation, as evidenced by the computed ratios depicted in Figure 5.8.
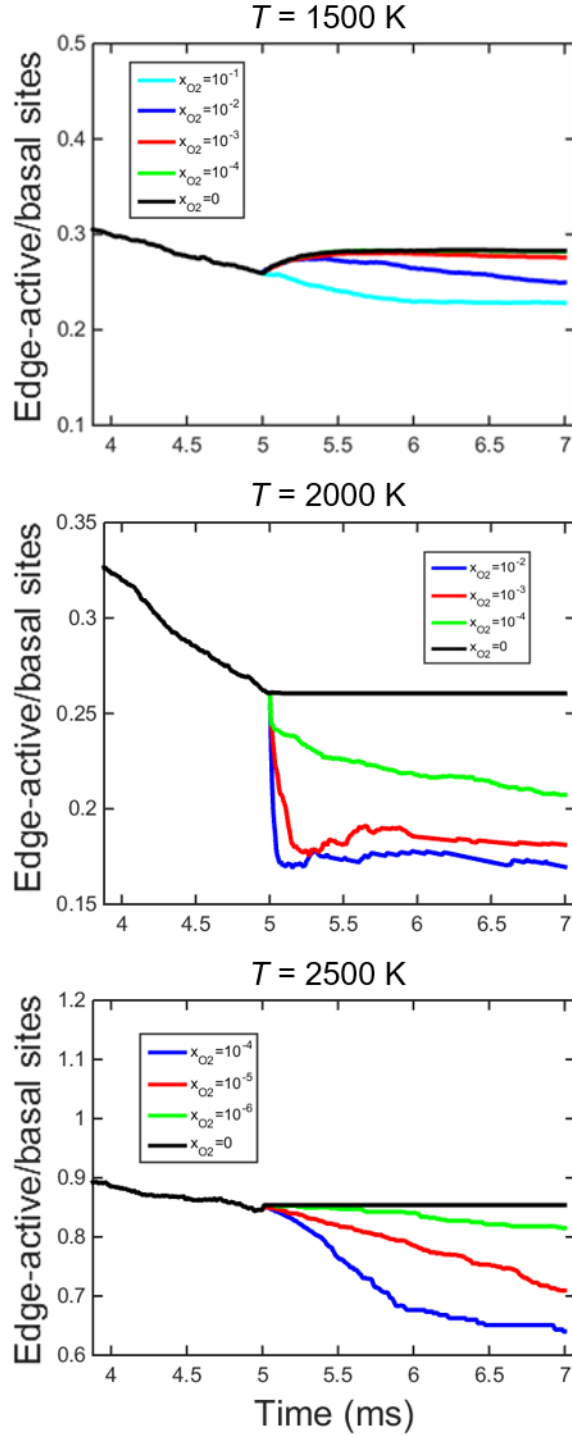
Figure 5.8. C_{edge}-H/C_{basal} site ratio versus time.

At all temperatures the ratio is decreasing during the growth period of the simulation. This is readily understood: carbon addition reactions reproduce edge sites while incorporating the carbon atoms of the preceding reactive sites into the basal plane. One would expect a reverse outcome in oxidation: removal of peripheral edge carbons would leave behind reactive sites while decreasing the number of inner, basal-plane carbons. However, the simulations showed that the C_{edge}-H/C_{basal} site ratio is decreased during oxidation. The results at 1500 K, displaying an initial increase in this site ratio, may seem contradictory to this assessment. A closer examination, adding an annealing period between growth an oxidation (see Section 5.3.4), revealed that the rise in the site ratio is due to thermal desorption of carbon, but the oxidation keeps decreasing it, as demonstrated in Figure 5.9. The reason for the site ratio decrease, as explained above, is the formation of five-member rings that accumulate and create less-reactive zigzag edges. These considerations lead me to conclude that the observed decrease in reactivity over time seen in my results is in accord with the phenomena observed in experiment [88-90].
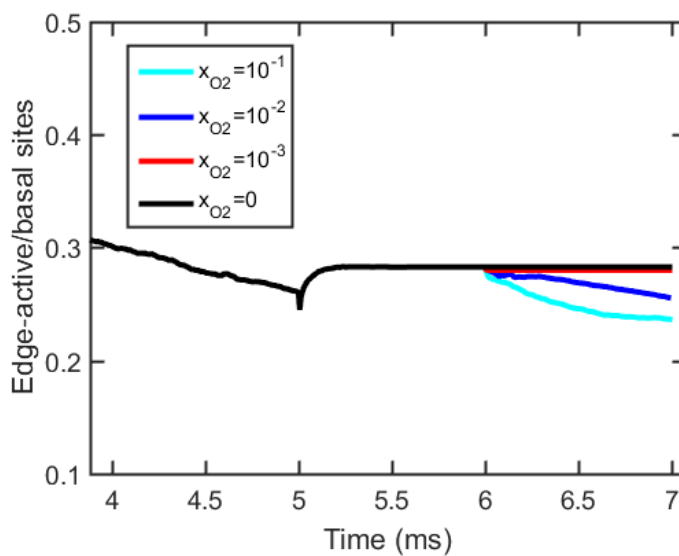
Figure 5.9. C_{edge}-H/C_{basal} site ratio computed at the same conditions as those of upper left corner of Figure 5.4 with the addition of 1 ms annealing period between growth and oxidation.

5.3.4 Effect of Graphene Curvature on the Rate of Oxidation

In an earlier experimental study, Vander Wal and Tomasek [91] investigated the dependence of oxidation rates on particle nanostructure. Soot was synthesized using three different fuels (acetylene, benzene, and ethanol) to achieve different nanostructures. Burnout rates were measured for the initial stage of oxidation, when less than 25 % of the initial mass was lost. The authors [91] found that the burnout rates for ethanol- and benzene-derived soot were higher than those for acetylene-derived soot by nearly a factor of five. Fringe lattice analysis revealed that the fringe length distribution of benzene-derived soot indicated shorter, unaligned graphene segments, which is indicative of a high ratio of edge-site carbon atoms to basal-plane carbon atoms and, therefore, higher reactivity.

However, ethanol-derived soot had longer graphene segments, like acetylene-derived soot but still had much higher burnout rates. Examination of the HRTEM images showed that ethanol-derived soot had much greater curvature than acetylene-derived soot. Vander Wal and Tomasek conjectured that a higher degree of curvature increases the imposed bond strain between C-C bonds thereby decreasing their resistance toward oxidation and thus explained why the ethanol-derived soot had higher burnout rates than the acetylene-derived soot despite having a similar fringe length distribution.

My numerical prediction that incorporation of five-member rings into graphene edges causes the decay in the oxidation rate could be seemingly perceived as contradictory to the experimentally derived conclusion of Vander Wal and Tomasek [91] that graphene curvature increases the oxidation rate of soot. Yet, further analysis revealed not only that there is no controversy but identified an additional feature of the graphene oxidation.

This next set of tests was performed by starting oxidation with graphene structures of differing curvature. Such two different nanostructures were obtained in KMC simulations of graphene growth at two different temperatures, 1500 and 2000 K. The degree of curvature was quantified by the five-member ring fraction, f_{R5}. The substrates grown at 1500 K had an average f_{R5} of 0.18, while those grown at 2000 K had an average f_{R5} of 0.10, thus indicating a higher degree of curvature for the substrates grown at 1500 K. Figure 5.10 illustrates the differences in curvature by showing representative structures after 5 ms of growth at each temperature.
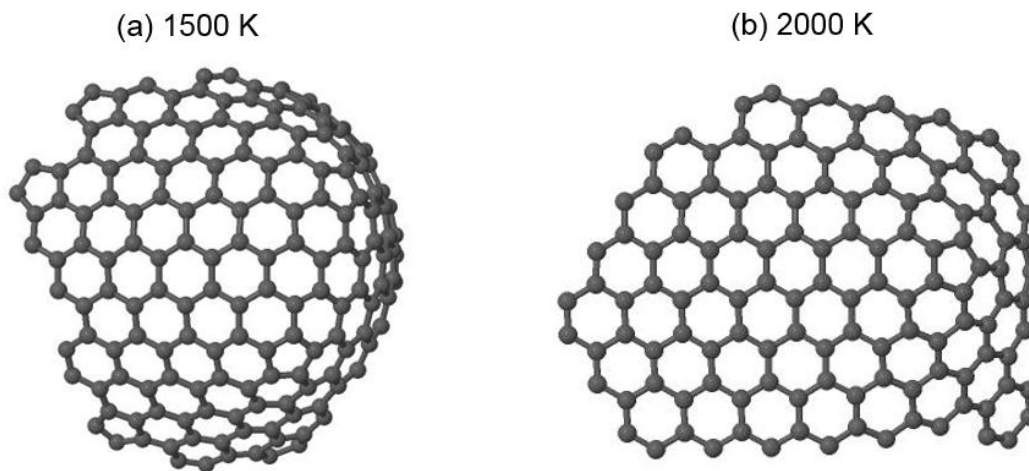
(a) 1500 K   (b) 2000 K

Figure 5.10. Snapshots of substrates grown at (a) 1500 K and (b) 2000 K at 5 ms. The H atoms saturating the edge carbon atoms are not shown for clarity.

The two graphene structures were subjected to oxidation at different oxygen concentrations, each substrate at three different temperatures: 1500, 2000, and 2500 K. The KMC simulations were now performed in three stages: growth, annealing, and oxidation. Like in prior simulations, the graphene sheet was grown for 5 ms starting with an initial coronene substrate. After that, the grown graphene structure underwent an annealing period for 1

ms, during which C_2H_2 and H were removed from the gaseous environment and O_2 was not yet added. The purpose of the annealing period was to allow for radical sites that existed at 5 ms to thermally decompose. At 6 ms, molecular oxygen and atomic hydrogen were added to the gaseous environment for 2 ms of oxidation. The temperature and pressure remained unchanged throughout the simulation. To stay closer to the experimental procedure of Vander Wal and Tomasek [91], I examined here the initial rates of oxidation. The obtained results are reported in Table 5.11. (It is noted here that the experimental results of Vander Wal and Tomasek [91] were carried out close to 1000 K, well below 1500 K, the intended lower bound of the temperature range for our mechanism. As a test, to confirm my comparison, I performed simulations at 1000 K as well as at a lower H-atom concentration, $x_H = 1\times10^{-3}$ [Tables 5.12 and 5.13]; and the results obtained were similar, qualitatively, to those reported in Table 5.11).

Table 5.11 Initial oxidation rates (C-atom/ms) for substrates with different curvature.

Oxidation T (K)		1500			2000			2500		
x_{O_2}		10^{-3}	10^{-2}	10^{-1}	10^{-4}	10^{-3}	10^{-2}	10^{-6}	10^{-5}	10^{-4}
Growth T (K)	f_{R5}									
1500	0.18	24.5	26.6	36.4	48.8	77.6	82.1	42.2	44.3	59.7
2000	0.10	6.4	9.1	21.2	15.3	45.0	54.1	9.3	10.7	29.0

Table 5.12. Initial oxidation rates (C-atom/ms) for substrates with different curvature for oxidation at 1000 K.

	x_{O_2}	10^{-3}	10^{-2}	10^{-1}
Growth T (K)	f_{R5}			
1500	0.18	4.0	4.2	8.1
2000	0.10	3.7	3.8	6.0

Table 5.13. Initial oxidation rates (C-atom/ms) for substrates with different curvature for $x_H = 1\times10^{-3}$ during oxidation.

Oxidation T (K)		1500			2000			2500		
	x_{O_2}	10^{-3}	10^{-2}	10^{-1}	10^{-4}	10^{-3}	10^{-2}	10^{-6}	10^{-5}	10^{-4}
Growth T (K)	f_{R5}									
1500	0.18	20.9	25.9	26.0	46.2	52.5	55.7	41.1	43.3	46.5
2000	0.10	5.5	8.9	15.3	14.6	29.3	33.6	9.1	9.4	23.0

Inspection of the results reported in Table 5.11 indicates that in all nine cases tested the oxidation rates were higher, by a factor of 1.5 to 4.6, for graphene with larger starting curvature. This comparison shows that our KMC model does reproduce the phenomenon seen in the experiments of Vander Wal and Tomasek [91]. Then how can it be that the same mechanistic feature—incorporation of five-member rings into a growing edge of graphene—explains both the decay of the oxidation rate in time and the faster initial oxidation of a more curved graphene?

In search for answers I turned to analysis of the underlying reaction statistics. The average reaction counts during oxidation are presented in Tables 5.14 – 5.19.

Table 5.14. Reaction counts for KMC simulations grown from coronene at 1500 K and oxidized at 1500 K.

	x_{O_2}		
Reaction	10^{-3}	10^{-2}	10^{-1}
1	313.8	293.2	215.8
2	308.5	282.7	197.5
3	0.0	0.0	0.0
4	0.0	0.0	0.0
5	1.7	1.7	2.2
6	7.4	7.3	7.3
7	1.4	1.6	1.6
8	8.7	8.5	8.6
9	22.3	22.9	18.5
10	33.4	44.4	71.5
11	33.4	44.4	71.5
12	298.5	388.0	651.8
13	297.6	386.0	647.8
14	0.0	0.0	0.0
15	0.0	0.0	0.0
16	0.0	0.0	0.0

17	0.0	0.0	0.0
18	0.0	0.0	0.0
19	0.0	0.0	0.0
20	0.0	0.0	0.0
21	0.0	0.0	0.0
22	0.0	0.0	0.0
23	0.0	0.0	0.0
24	0.0	0.0	0.0
25	0.0	0.0	0.0
26	0.0	0.0	0.0
27	0.0	0.0	0.0
28	0.2	0.2	0.2
29	0.7	1.3	2.2
30	2.4	2.9	2.7
31	3.5	5.5	8.8
32	1.4	2.3	4.1
33	0.0	0.0	0.0
34	0.0	0.0	0.0
35	0.0	0.0	0.0
36	0.0	0.0	0.0
37	0.0	0.0	0.0
38	0.0	0.0	0.0
39	0.0	0.0	0.0
40	0.0	0.0	0.0
41	0.1	0.1	0.1
42	0.0	0.0	0.0
43	0.1	0.1	0.1
44	0.0	0.0	0.0
45	0.1	0.1	0.2
46	0.3	1.8	4.3
47	0.9	5.4	12.3
48	6.6	50.9	131.9
49	6.5	51.3	124.7
50	7.8	64.5	350.2
51	0.0	0.1	0.3
52	0.0	0.0	0.2
53	0.2	0.8	1.9
54	0.2	0.9	2.6
55	0.0	0.0	0.0
56	0.0	0.0	0.0
57	0.0	0.0	0.0
58	0.0	0.0	0.0
59	0.0	0.0	0.0
60	0.0	0.0	0.0
61	0.0	0.0	0.0

62	0.0	0.0	0.0
63	0.0	0.0	0.0
64	0.0	0.0	0.2
65	0.3	1.7	4.0
66	0.9	5.4	12.2
67	6.1	50.3	132.7
68	6.8	51.6	122.7
69	8.0	65.2	355.9
70	0.0	0.0	0.0
71	0.0	0.0	0.0
72	0.0	0.0	0.0
73	0.0	0.0	0.0
74	0.0	0.0	0.0
75	0.0	0.0	0.1
76	0.0	0.1	0.3
77	0.2	1.2	3.2
78	0.1	1.2	3.1
79	0.2	1.4	9.7
80	0.0	0.0	0.0
81	0.0	0.0	0.2
82	0.1	0.6	1.6
83	0.1	0.6	1.6
84	0.1	0.7	4.2
85	0.3	1.6	4.0
86	0.9	5.3	12.2
87	6.4	49.9	130.5
88	6.4	50.7	121.7
89	7.8	64.6	350.2
90	0.0	0.0	0.0

Table 5.15. Reaction counts for KMC simulations grown from coronene at 1500 K and oxidized at 2000 K.

	x_{O_2}		
Reaction	10^{-4}	10^{-3}	10^{-2}
1	835.9	637.2	529.4
2	797.0	586.9	483.6
3	0.0	0.0	0.0
4	0.0	0.0	0.0
5	2.6	3.4	3.4
6	1.7	2.1	1.7
7	0.6	1.1	0.5
8	2.5	3.0	2.7
9	0.4	0.4	0.2
10	115.5	210.2	236.7

11	115.5	210.2	236.7
12	262.8	482.8	541.5
13	259.3	476.7	536.0
14	0.0	0.0	0.0
15	0.1	0.1	0.1
16	0.4	0.8	0.5
17	0.2	0.3	0.2
18	0.0	0.0	0.0
19	0.0	0.0	0.0
20	0.0	0.0	0.0
21	0.0	0.0	0.0
22	0.0	0.0	0.0
23	0.0	0.0	0.0
24	0.1	0.1	0.0
25	0.0	0.0	0.0
26	0.0	0.0	0.0
27	0.0	0.0	0.0
28	0.0	0.0	0.0
29	0.6	1.4	1.1
30	14.0	16.0	13.6
31	17.2	22.3	21.1
32	7.9	10.2	8.9
33	0.0	0.0	0.0
34	0.0	0.0	0.0
35	0.0	0.0	0.0
36	0.0	0.0	0.0
37	0.0	0.0	0.0
38	0.0	0.0	0.0
39	0.0	0.0	0.0
40	0.0	0.0	0.0
41	0.3	0.3	0.2
42	0.0	0.0	0.0
43	0.0	0.0	0.1
44	0.0	0.0	0.0
45	0.0	0.0	0.0
46	0.1	0.2	0.1
47	0.2	0.4	0.3
48	1.6	3.5	3.3
49	1.7	2.8	3.1
50	1.7	8.4	48.5
51	0.1	0.2	0.1
52	0.1	0.3	0.3
53	1.4	2.7	2.3
54	1.4	2.5	2.9
55	0.0	0.0	0.0

Reaction			
56	0.0	0.0	0.0
57	0.0	0.0	0.0
58	0.0	0.0	0.0
59	0.0	0.0	0.0
60	0.0	0.0	0.0
61	0.0	0.0	0.0
62	0.1	0.2	0.2
63	0.1	0.2	0.4
64	0.7	3.0	22.5
65	0.0	0.0	0.0
66	0.1	0.1	0.0
67	0.3	0.8	0.9
68	0.4	0.7	0.9
69	2.4	11.6	71.4
70	0.0	0.0	0.0
71	0.0	0.0	0.0
72	0.0	0.0	0.0
73	0.0	0.0	0.0
74	0.0	0.1	1.1
75	0.0	0.0	0.0
76	0.0	0.0	0.0
77	0.0	0.0	0.0
78	0.0	0.0	0.0
79	0.1	0.7	3.7
80	0.0	0.0	0.0
81	0.0	0.0	0.0
82	0.0	0.1	0.1
83	0.0	0.0	0.0
84	0.2	0.6	3.3
85	0.0	0.0	0.0
86	0.0	0.1	0.0
87	0.2	0.6	0.6
88	0.3	0.5	0.7
89	1.7	8.3	47.7
90	0.0	0.0	0.0

Table 5.16. Reaction counts for KMC simulations grown from coronene at 1500 K and oxidized at 2500 K.

	x_{O_2}		
Reaction	10^{-6}	10^{-5}	10^{-4}
1	1694.8	1658.2	1335.0
2	1664.2	1619.9	1269.3
3	0.0	0.0	0.0
4	0.0	0.0	0.0

5	2.1	2.2	3.3
6	0.4	0.4	0.6
7	0.3	0.3	0.6
8	0.6	0.7	1.7
9	0.0	0.0	0.1
10	115.5	134.3	270.3
11	115.6	134.4	270.3
12	108.9	125.2	250.8
13	108.2	123.9	246.1
14	0.0	0.0	0.0
15	0.1	0.0	0.1
16	0.1	0.2	0.5
17	0.1	0.1	0.6
18	0.0	0.0	0.0
19	0.0	0.0	0.0
20	0.0	0.0	0.0
21	0.0	0.0	0.0
22	0.0	0.0	0.0
23	0.0	0.0	0.0
24	0.1	0.1	0.1
25	0.0	0.0	0.0
26	0.0	0.0	0.0
27	0.0	0.0	0.0
28	0.0	0.0	0.0
29	0.0	0.1	0.1
30	17.1	20.1	26.9
31	10.4	13.4	27.1
32	5.5	7.0	12.9
33	0.0	0.0	0.0
34	0.0	0.0	0.0
35	0.0	0.0	0.0
36	0.0	0.0	0.0
37	0.0	0.0	0.0
38	0.0	0.0	0.0
39	0.0	0.0	0.0
40	0.0	0.0	0.0
41	0.2	0.2	0.2
42	0.0	0.0	0.0
43	0.0	0.0	0.0
44	0.0	0.0	0.0
45	0.0	0.0	0.0
46	0.0	0.0	0.0
47	0.0	0.0	0.2
48	0.1	0.4	1.9
49	0.0	0.3	1.8

50	0.0	0.4	2.8
51	0.0	0.0	0.0
52	0.0	0.0	0.2
53	0.1	0.3	1.7
54	0.0	0.4	2.0
55	0.0	0.0	0.0
56	0.0	0.0	0.0
57	0.0	0.0	0.0
58	0.0	0.0	0.0
59	0.0	0.0	0.0
60	0.0	0.0	0.0
61	0.0	0.0	0.0
62	0.0	0.0	0.0
63	0.0	0.0	0.0
64	0.0	2.5	17.1
65	0.0	0.0	0.0
66	0.0	0.0	0.0
67	0.0	0.0	0.0
68	0.0	0.0	0.0
69	0.0	2.5	17.8
70	0.0	0.0	0.0
71	0.0	0.0	0.0
72	0.0	0.0	0.0
73	0.0	0.0	0.0
74	0.0	0.3	2.3
75	0.0	0.0	0.0
76	0.0	0.0	0.0
77	0.0	0.0	0.0
78	0.0	0.0	0.0
79	0.0	0.0	0.1
80	0.0	0.0	0.0
81	0.0	0.0	0.0
82	0.0	0.0	0.0
83	0.0	0.0	0.0
84	0.0	0.4	2.3
85	0.0	0.0	0.0
86	0.0	0.0	0.0
87	0.0	0.0	0.0
88	0.0	0.0	0.0
89	0.0	0.1	0.5
90	0.0	0.0	0.0

Table 5.17. Reaction counts for KMC simulations grown from coronene at 2000 K and oxidized at 1500 K.

Reaction	x_{O_2}		
	10^{-3}	10^{-2}	10^{-1}
1	331.9	295.9	221.3
2	328.6	283.3	200.7
3	0.0	0.0	0.0
4	0.0	0.0	0.0
5	0.5	0.6	0.8
6	1.9	1.8	2.4
7	0.4	0.3	0.3
8	2.3	2.2	2.9
9	8.0	6.9	8.2
10	7.1	21.4	50.0
11	7.1	21.4	50.0
12	63.3	185.5	452.3
13	62.7	183.7	449.1
14	0.0	0.0	0.0
15	0.0	0.0	0.0
16	0.0	0.0	0.0
17	0.0	0.0	0.0
18	0.0	0.0	0.0
19	0.0	0.0	0.0
20	0.0	0.0	0.0
21	0.0	0.0	0.0
22	0.0	0.0	0.0
23	0.0	0.0	0.0
24	0.0	0.0	0.0
25	0.0	0.0	0.0
26	0.0	0.0	0.0
27	0.0	0.0	0.0
28	0.0	0.0	0.0
29	0.2	0.7	0.9
30	2.3	4.4	4.4
31	1.3	4.8	9.2
32	0.6	1.9	3.6
33	0.0	0.0	0.0
34	0.0	0.0	0.0
35	0.0	0.0	0.0
36	0.0	0.0	0.0
37	0.0	0.0	0.0
38	0.0	0.0	0.0
39	0.0	0.0	0.0
40	0.0	0.0	0.0

41	0.1	0.1	0.1
42	0.0	0.0	0.0
43	0.0	0.0	0.0
44	0.0	0.0	0.0
45	0.0	0.1	0.1
46	0.1	0.6	2.0
47	0.3	1.0	4.1
48	8.5	58.5	117.0
49	8.4	59.7	120.0
50	11.6	93.2	525.2
51	0.0	0.0	0.1
52	0.0	0.0	0.0
53	0.1	1.1	2.2
54	0.2	1.1	2.1
55	0.0	0.0	0.0
56	0.0	0.0	0.0
57	0.0	0.0	0.0
58	0.0	0.0	0.0
59	0.0	0.0	0.0
60	0.0	0.0	0.0
61	0.0	0.0	0.0
62	0.0	0.0	0.1
63	0.0	0.0	0.0
64	0.0	0.1	0.2
65	0.1	0.6	1.9
66	0.3	1.0	4.2
67	8.5	59.6	117.1
68	8.3	58.6	118.8
69	11.7	95.0	531.9
70	0.0	0.0	0.0
71	0.0	0.0	0.0
72	0.0	0.0	0.0
73	0.0	0.0	0.0
74	0.0	0.0	0.0
75	0.0	0.0	0.1
76	0.0	0.0	0.1
77	0.2	1.6	2.9
78	0.2	1.7	3.0
79	0.3	2.6	12.9
80	0.0	0.0	0.1
81	0.0	0.0	0.0
82	0.1	0.7	1.4
83	0.1	0.6	1.6
84	0.1	0.9	6.6
85	0.1	0.6	1.9

86	0.3	1.0	4.2
87	8.3	58.1	116.0
88	8.3	58.0	117.1
89	11.6	93.3	525.4
90	0.0	0.0	0.0

Table 5.18. Reaction counts for KMC simulations grown from coronene at 2000 K and oxidized at 2000 K.

	x_{O_2}		
Reaction	10^{-4}	10^{-3}	10^{-2}
1	873.8	572.3	502.1
2	835.6	532.8	469.6
3	0.0	0.0	0.0
4	0.0	0.0	0.0
5	1.1	2.3	2.4
6	0.7	1.2	1.8
7	0.3	0.6	0.5
8	1.0	2.3	2.9
9	0.1	0.1	0.1
10	62.4	138.6	175.0
11	62.4	138.6	175.1
12	141.5	315.2	403.7
13	139.0	309.9	398.4
14	0.0	0.0	0.0
15	0.1	0.1	0.1
16	0.2	0.8	0.9
17	0.1	0.3	0.3
18	0.0	0.0	0.0
19	0.0	0.0	0.0
20	0.0	0.0	0.0
21	0.0	0.0	0.0
22	0.0	0.0	0.0
23	0.0	0.0	0.0
24	0.1	0.1	0.0
25	0.0	0.0	0.0
26	0.0	0.0	0.0
27	0.0	0.0	0.0
28	0.0	0.0	0.0
29	0.7	1.8	1.8
30	18.0	12.6	10.3
31	12.3	16.2	14.0
32	6.3	7.7	5.3
33	0.0	0.0	0.0
34	0.0	0.0	0.0

35	0.0	0.0	0.0
36	0.0	0.0	0.0
37	0.0	0.0	0.0
38	0.0	0.0	0.0
39	0.0	0.0	0.0
40	0.0	0.0	0.0
41	0.2	0.1	0.2
42	0.0	0.0	0.0
43	0.1	0.1	0.0
44	0.0	0.0	0.0
45	0.0	0.0	0.0
46	0.0	0.1	0.0
47	0.1	0.3	0.3
48	1.6	2.7	2.7
49	1.6	2.3	2.5
50	3.0	11.5	54.0
51	0.0	0.1	0.0
52	0.1	0.3	0.3
53	1.4	2.2	1.9
54	1.4	2.3	2.5
55	0.0	0.0	0.0
56	0.0	0.0	0.0
57	0.0	0.0	0.0
58	0.0	0.0	0.0
59	0.0	0.0	0.0
60	0.0	0.0	0.0
61	0.0	0.0	0.0
62	0.1	0.3	0.1
63	0.0	0.1	0.3
64	1.3	4.2	22.1
65	0.0	0.0	0.0
66	0.0	0.0	0.1
67	0.3	0.4	0.6
68	0.3	0.5	0.8
69	4.3	16.0	75.4
70	0.0	0.0	0.0
71	0.0	0.0	0.0
72	0.0	0.0	0.0
73	0.0	0.0	0.0
74	0.0	0.4	0.7
75	0.0	0.0	0.0
76	0.0	0.0	0.0
77	0.0	0.0	0.1
78	0.0	0.0	0.0
79	0.3	1.1	3.7

80	0.0	0.0	0.0
81	0.0	0.0	0.0
82	0.0	0.1	0.0
83	0.0	0.0	0.0
84	0.2	0.9	4.6
85	0.0	0.0	0.0
86	0.0	0.0	0.0
87	0.2	0.3	0.6
88	0.2	0.3	0.3
89	3.0	11.2	53.4
90	0.0	0.0	0.0

Table 5.19. Reaction counts for KMC simulations grown from coronene at 2000 K and oxidized at 2500 K.

	x_{O_2}		
Reaction	10^{-6}	10^{-5}	10^{-4}
1	1713.4	1647.8	1388.1
2	1694.9	1618.7	1318.9
3	0.0	0.0	0.0
4	0.0	0.0	0.0
5	0.4	0.7	2.2
6	0.1	0.1	0.5
7	0.0	0.1	0.5
8	0.1	0.3	1.5
9	0.0	0.0	0.0
10	25.6	43.6	155.6
11	25.6	43.6	155.5
12	23.6	40.8	151.2
13	23.4	39.7	146.3
14	0.0	0.0	0.0
15	0.0	0.0	0.0
16	0.0	0.2	0.7
17	0.0	0.1	0.4
18	0.0	0.0	0.0
19	0.0	0.0	0.0
20	0.0	0.0	0.0
21	0.0	0.0	0.0
22	0.0	0.0	0.0
23	0.0	0.0	0.0
24	0.0	0.0	0.0
25	0.0	0.0	0.0
26	0.0	0.0	0.0
27	0.0	0.0	0.0
28	0.0	0.0	0.0

29	0.0	0.0	0.1
30	12.4	17.4	35.7
31	4.3	8.3	22.1
32	2.4	3.9	10.5
33	0.0	0.0	0.0
34	0.0	0.0	0.0
35	0.0	0.0	0.0
36	0.0	0.0	0.0
37	0.0	0.0	0.0
38	0.0	0.0	0.0
39	0.0	0.0	0.0
40	0.0	0.0	0.0
41	0.2	0.2	0.3
42	0.0	0.0	0.0
43	0.0	0.0	0.1
44	0.0	0.0	0.0
45	0.0	0.0	0.0
46	0.0	0.0	0.1
47	0.0	0.0	0.3
48	0.0	0.5	1.8
49	0.0	0.3	2.0
50	0.1	0.6	4.0
51	0.0	0.0	0.1
52	0.0	0.0	0.3
53	0.0	0.4	1.8
54	0.0	0.4	2.0
55	0.0	0.0	0.0
56	0.0	0.0	0.0
57	0.0	0.0	0.0
58	0.0	0.0	0.0
59	0.0	0.0	0.0
60	0.0	0.0	0.0
61	0.0	0.0	0.0
62	0.0	0.0	0.0
63	0.0	0.0	0.0
64	0.3	3.1	22.8
65	0.0	0.0	0.0
66	0.0	0.0	0.0
67	0.0	0.0	0.0
68	0.0	0.0	0.0
69	0.3	3.3	24.3
70	0.0	0.0	0.0
71	0.0	0.0	0.0
72	0.0	0.0	0.0
73	0.0	0.0	0.0

74	0.1	0.4	3.3
75	0.0	0.0	0.0
76	0.0	0.0	0.0
77	0.0	0.0	0.0
78	0.0	0.0	0.0
79	0.0	0.0	0.2
80	0.0	0.0	0.0
81	0.0	0.0	0.0
82	0.0	0.0	0.0
83	0.0	0.0	0.0
84	0.0	0.4	2.7
85	0.0	0.0	0.0
86	0.0	0.0	0.0
87	0.0	0.0	0.0
88	0.0	0.0	0.0
89	0.0	0.2	0.7
90	0.0	0.0	0.0

In the KMC model, in addition to carbon being removed from the graphene edge by oxidation, reactions 51–54 and 90, it is also eliminated by thermal desorption.

In these simulation tests, the frequency of oxidation reactions 51–54 was approximately the same for substrates grown at 1500 and 2000 K. However, the thermal desorption reactions, primarily reactions 5 and 7, occurred between two to four times as often for the substrates grown at 1500 K as for those grown at 2000 K during the first 0.2 ms of oxidation (Figure 5.11). Therefore, it is the thermal desorption that accounts for the difference in the oxidation rates.

Further examination of the data displayed in Figure 5.11 shows that the difference in frequency of thermal desorption reactions between the two sets of substrates is much smaller after the initial 0.2 ms of oxidation for all simulations conditions. This suggests that the difference in oxidation rates between substrates with different curvature occurs primarily at the beginning of oxidation and happens because substrates with higher curvature form a larger number of sites that can potentially desorb.
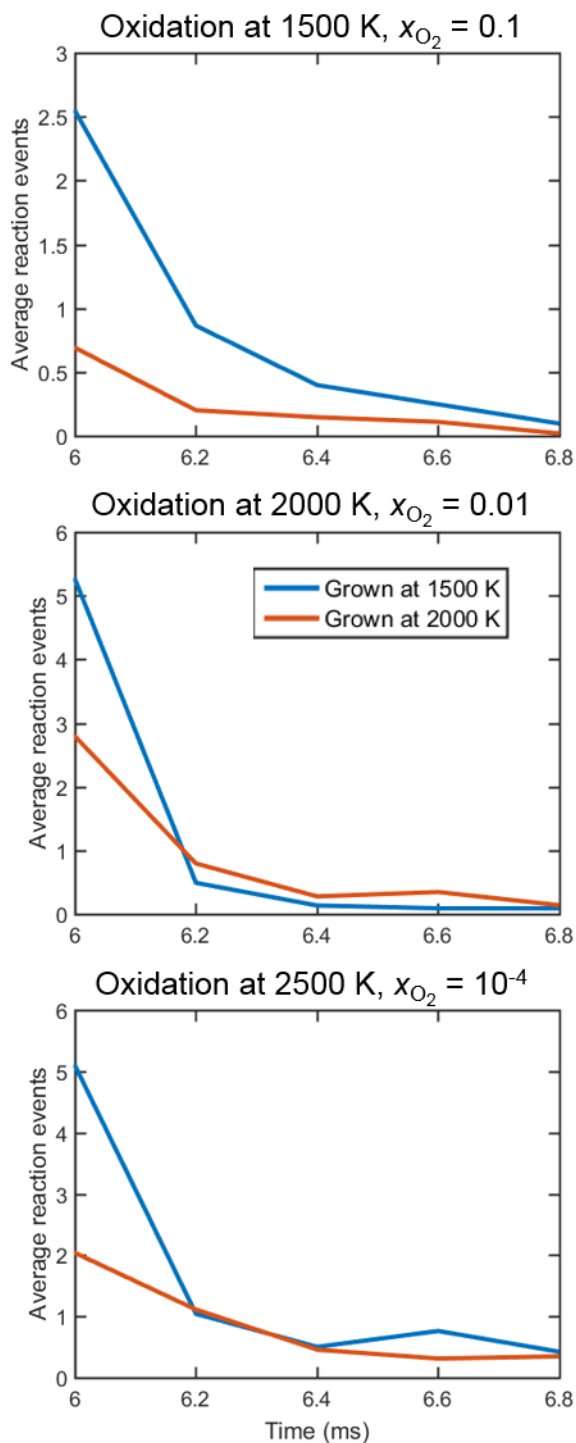
Figure 5.11. Event counts for thermal desorption reactions versus time for substrates oxidized at three sets of conditions.

The reaction count statistics indicate that the metric of curvature is more complex than simply knowing the fraction of five-member rings in the graphene sheet. Five-member rings can affect oxidation differently, depending on their location in the graphene sheet, i.e., if they are on an edge or embedded. The time evolution of the different types of five-

member rings is plotted in Figure 5.12. Inspection of these results indicates that at the beginning of oxidation substrates grown at 1500 K have a higher number of free five-member rings (red lines in Figure 5.12) that can be thermally desorbed compared to substrates grown at 2000 K, thus explaining the difference in the reaction counts presented earlier. As oxidation progresses, the free five-member rings are thermally desorbed and their number decreases close to zero for the substrates grown at both temperatures. The number of five-member rings at armchair sites (blue lines) increases for both substrates due to thermal decomposition of oxyradicals to form five-member rings. These latter five-member rings form zigzag edges that lead to a decrease in oxidative reactivity. The number of bay-capped five-member rings (black lines) decrease only slightly for the substrates at both temperatures and do not seem to affect the oxidation rate.
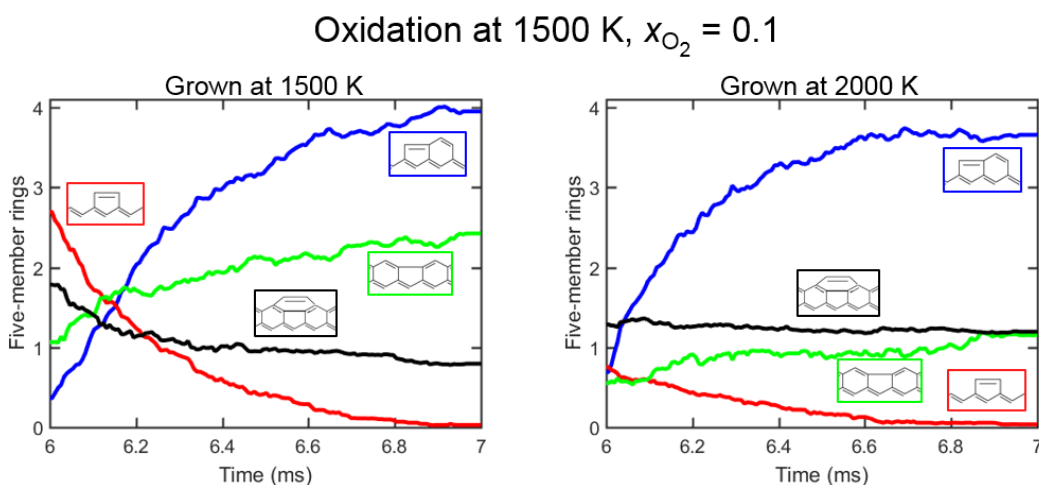
Figure 5.12. Number of five-member rings versus time for substrates grown at 1500 (left) or 2000 K (right), and oxidized at 1500 K with $x_{O_2} = 0.1$.

Thus, while the total number of five-member rings increases during oxidation for the substrates grown at 1500 and 2000 K, their individual histories vary and have different effects on the oxidation rate. Analysis of the graphene-edge site distribution over time further supports this conclusion. Figure 5.13 displays population of pertinent edge sites at several instances of reaction; the sites are identified in Figure 5.14. Tables 5.20 – 5.27 display the values for the fraction of sites. Inspection of these results indicates that the fraction of free-edge sites decreases during the oxidation stage for both substrates. The substrates grown at 1500 K have a significant fraction of free-edge-5 sites, five-member rings that thermally desorb, which is evidenced by a substantial decrease in these sites during the annealing period. By contrast, such five-member rings barely appear on substrates grown at 2000 K. This discrepancy in free-edge-5 sites further illuminates that a higher oxidation rate of more curved graphene is due to the presence of five-member rings that can thermally desorb. At the same time, the total number of zigzag sites, the sum of zigzag and zigzag-5 sites, increases as oxidation progresses at both temperatures. Accumulation of such less-reactive-to-oxidation sites causes the decrease in the oxidation rate over time. These distinct aspects of graphene edge morphology reconcile the two seemingly contradictory conclusions about curvature effects on oxidation rates.
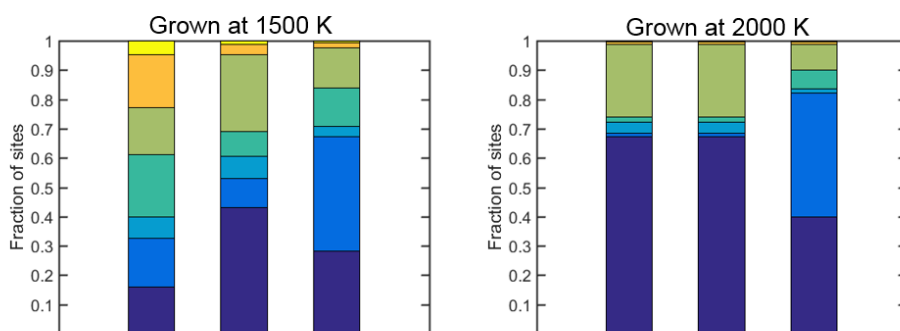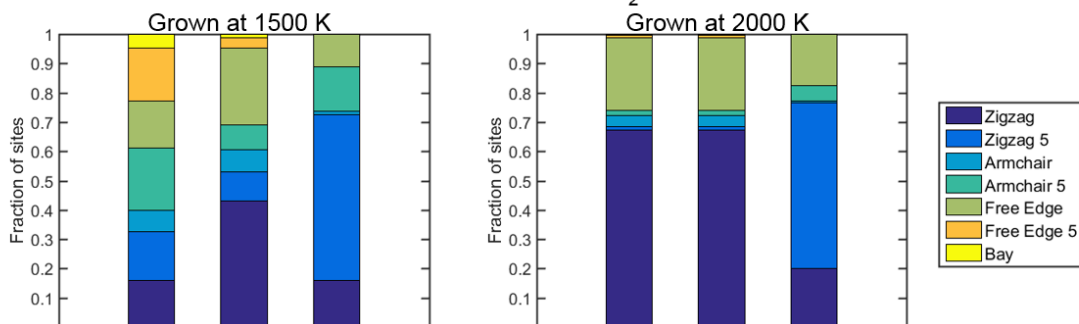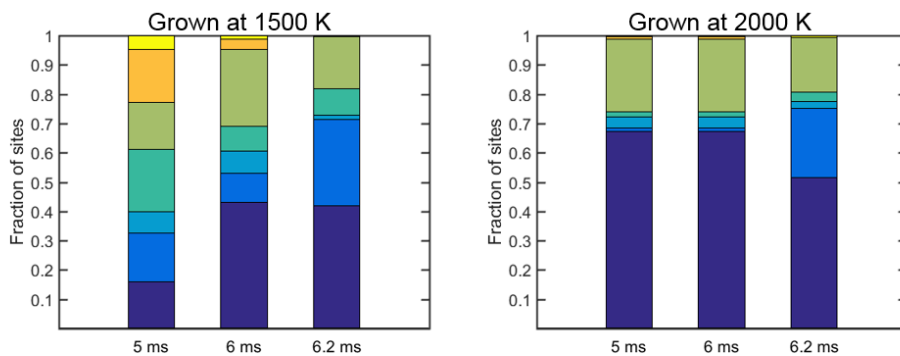
Figure 5.13. Site distribution at 5 ms (start of annealing), 6 ms (start of oxidation), and 6.2 ms (after 0.2 ms of oxidation) for substrates grown and oxidized under different conditions.
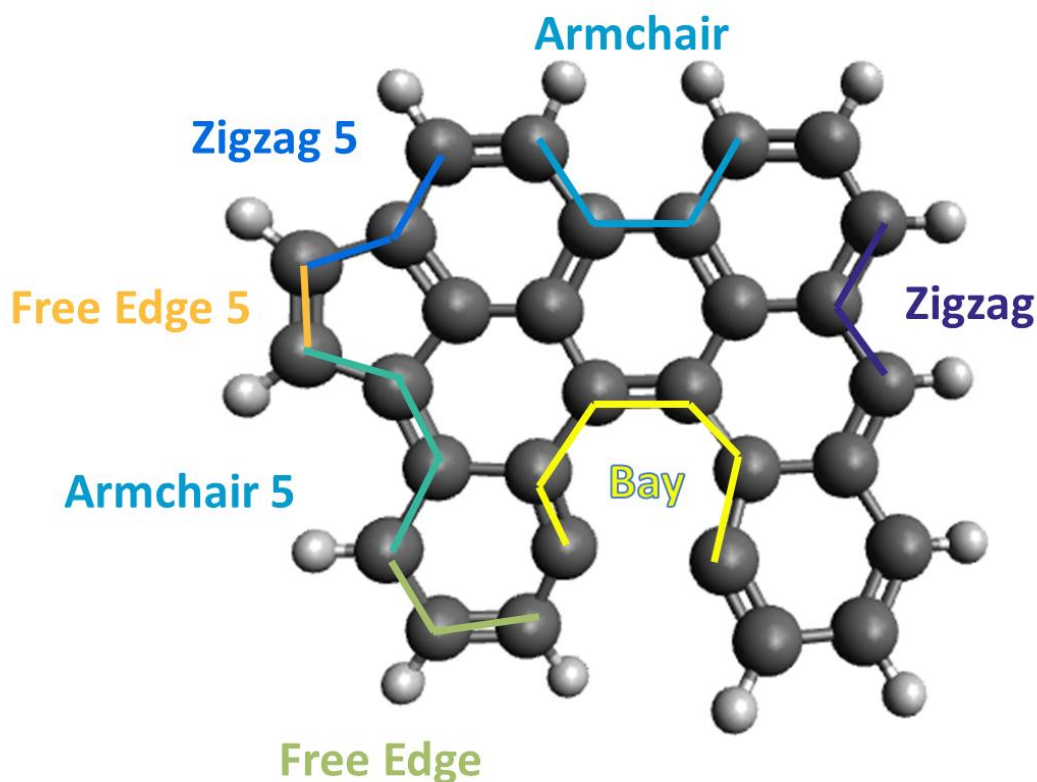
Figure 5.14. Diagram of sites used in Figure 5.13.

Table 5.20. Site distribution at the start of annealing and start of oxidation for substrates grown at 1500 K.

t (ms)	x_{O_2}	Fraction of sites						
		ac	ac5	zz	zz5	fe	fe5	bay
5	0.0E+00	0.07	0.22	0.17	0.17	0.15	0.18	0.04
6	0.0E+00	0.07	0.08	0.45	0.10	0.26	0.03	0.01

Table 5.21. Site distribution after 0.2 ms for substrates grown at 1500 K and oxidized at 1500 K.

t (ms)	x_{O_2}	Fraction of sites						
		ac	ac5	zz	zz5	fe	fe5	bay
6.2	1.0E-03	0.08	0.06	0.47	0.09	0.28	0.01	0.01
6.2	1.0E-02	0.07	0.07	0.44	0.16	0.24	0.01	0.01
6.2	1.0E-01	0.04	0.13	0.28	0.39	0.14	0.02	0.01

Table 5.22. Site distribution after 0.2 ms for substrates grown at 1500 K and oxidized at 2000 K.

		Fraction of sites						
t (ms)	x_{O_2}	ac	ac5	zz	zz5	fe	fe5	bay
6.2	1.0E-04	0.05	0.06	0.47	0.21	0.22	0.00	0.01
6.2	1.0E-03	0.01	0.12	0.24	0.51	0.12	0.00	0.00
6.2	1.0E-02	0.01	0.15	0.16	0.57	0.11	0.00	0.00

Table 5.23. Site distribution after 0.2 ms for substrates grown at 1500 K and oxidized at 2500 K.

		Fraction of sites						
t (ms)	x_{O_2}	ac	ac5	zz	zz5	fe	fe5	bay
6.2	1.0E-06	0.07	0.03	0.55	0.07	0.28	0.00	0.01
6.2	1.0E-05	0.06	0.04	0.54	0.09	0.26	0.00	0.01
6.2	1.0E-04	0.02	0.09	0.42	0.29	0.18	0.00	0.01

Table 5.24. Site distribution at the start of annealing and start of oxidation for substrates grown at 2000 K.

		Fraction of sites						
t (ms)	x_{O_2}	ac	ac5	zz	zz5	fe	fe5	bay
5	0.0E+00	0.03	0.01	0.69	0.01	0.24	0.01	0.00
6	0.0E+00	0.03	0.01	0.69	0.01	0.24	0.01	0.00

Table 5.25. Site distribution after 0.2 ms for substrates grown at 2000 K and oxidized at 1500 K.

		Fraction of sites						
t (ms)	x_{O_2}	ac	ac5	zz	zz5	fe	fe5	bay
6.2	1.0E-03	0.04	0.01	0.69	0.02	0.24	0.00	0.00
6.2	1.0E-02	0.03	0.03	0.60	0.15	0.20	0.00	0.00
6.2	1.0E-01	0.02	0.06	0.40	0.42	0.09	0.01	0.00

Table 5.26. Site distribution after 0.2 ms for substrates grown at 2000 K and oxidized at 2000 K.

		Fraction of sites						
t (ms)	x_{O_2}	ac	ac5	zz	zz5	fe	fe5	bay
6.2	1.0E-04	0.03	0.03	0.59	0.17	0.19	0.00	0.00
6.2	1.0E-03	0.00	0.05	0.26	0.52	0.17	0.00	0.00
6.2	1.0E-02	0.01	0.05	0.20	0.57	0.17	0.00	0.00

Table 5.27. Site distribution after 0.2 ms for substrates grown at 2000 K and oxidized at 2500 K.

t (ms)	x_{O_2}	Fraction of sites						
		ac	ac5	zz	zz5	fe	fe5	bay
6.2	1.0E-06	0.03	0.01	0.71	0.01	0.24	0.00	0.00
6.2	1.0E-05	0.03	0.01	0.68	0.04	0.24	0.00	0.00
6.2	1.0E-04	0.02	0.03	0.51	0.24	0.19	0.00	0.01

5.4 Summary

The Kinetic Monte-Carlo simulations of the graphene-edge evolution in combustion-like environments revealed that oxidation by molecular oxygen exhibits two principal pathways: thermal decomposition of oxyradicals and regeneration of aromatic radical sites. Their competition is temperature dependent, with former dominating at higher and the latter at lower temperatures. Yet, the overall oxidation rate at the conditions tested is not substantially affected by presence or absence of the regeneration pathway. This may help in developing reduced models of soot oxidation at flame conditions.

The overall oxidation rate of the graphene substrate was computed to be time dependent, with reactivity decreasing over time as the ratio of reactive edge sites decreases relative to the number of basal-plane carbon atoms. At the same time, the oxidation rate was found to be higher for graphene with a higher initial curvature. Both results are in accord with experimental observations [88, 91]. Analysis showed that distinct aspects of graphene-edge morphology are responsible for curvature either raising or reducing the oxidative reactivity of the graphene edge.

6 Oxidation of Graphene-Edge Five-Member Rings by Atomic Oxygen

The KMC simulations discussed in the previous chapter modeled oxidation in an environment where O_2 was the only oxidizer. The simulations were able to reproduce qualitative graphene-edge oxidation behavior. The next step for the model was to quantitatively match experimentally measured soot oxidation rates in gas phase environments where other oxidizers like OH and O could play a role in the oxidation process. In this chapter, a pathway to oxidize embedded five-member rings via a reaction with O is discussed. The rate coefficients for this reaction were calculated and the reaction was added to the KMC model.

6.1 Introduction

In Chapter 4, the $C_{15}H_9 + O_2$ reaction system was investigated in order to find oxidation pathways for embedded five-member rings. While two pathways were found that produced $C_{14}H_9 + CO_2$ and $C_{15}H_9O + O$, both pathways were found to have rate coefficients that were substantially lower than the rate coefficients for the oxidation of six-member rings. You et al. [92] also explored oxidation pathways for embedded five-member rings, but they did not find any direct pathways for oxidation of five-member rings that were faster than the reactions presented in Chapter 4.

Although no fast pathways for five-member ring oxidation by O_2 have been found, in an evolving oxidative environment, other oxidizers like OH, O, and H_2O might yield faster reactions with embedded five-member rings. In collaboration with Mebel, these alternative pathways for oxidizing five-member rings were investigated. Based on initial quantum chemical calculations performed by Mebel, the oxidation of graphene-edge five-member rings by O was seen as the most promising pathway, so this Chapter will present the results of these calculations.

6.2 Potential Energy Surface

Mebel investigated the energetics of the $C_{15}H_9 + O$ reaction at the G3 level of theory. G3(MP2,CC)//B3LYP/6-311G**. The potential energy diagram is shown in Figure 6.1. The reaction begins with the barrierless association of $C_{15}H_9$ and O, followed by elimation of CO to form phenanthryl $C_{14}H_9$.

The potential along the MEP for addition of O to $C_{15}H_9$ was obtained by performing calculations at two levels of theory: B3LYP/6-311G** and CASPT2(19,14)/aug-cc-pVDZ. The potential computed at the CASPT2 level was found to be less attractive than the potential computed at the B3LYP level and showed a 'submerged' barrier at about -1 kcal/mol.
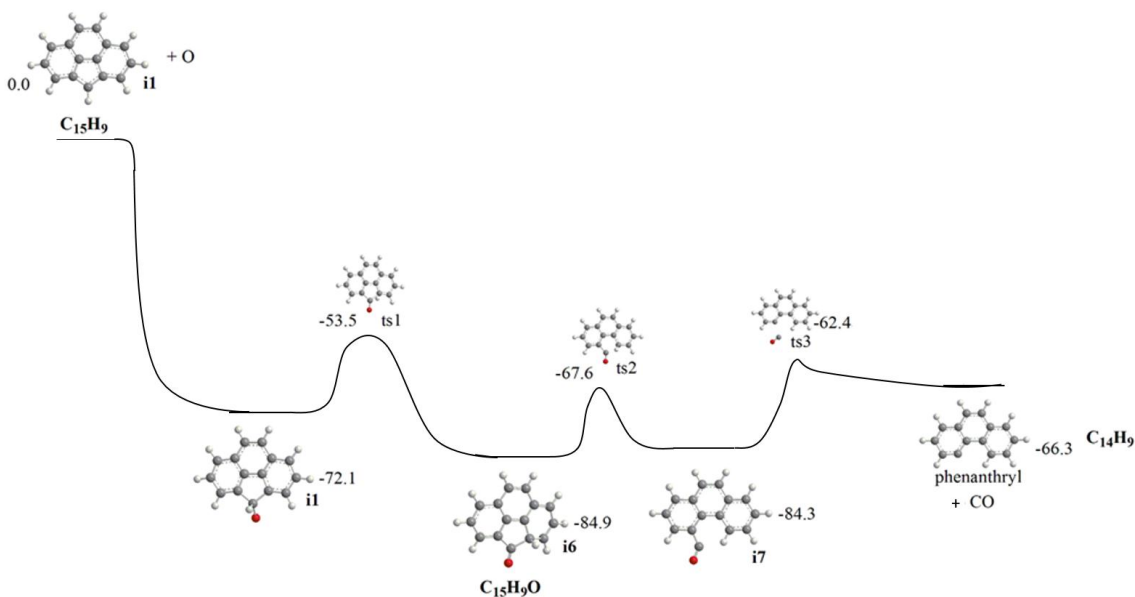
Figure 6.1. Potential energy diagram for $C_{15}H_9$ + O. Potential energies calculated at the G3(MP2,CC) level are shown in kcal/mol relative to $C_{15}H_9$.

6.3 Reaction Rate Coefficient Calculations

VRC-TST calculations of the thermal rate coefficient for the barrierless $C_{15}H_9$ + O association channel were performed using VariFlex following the same procedure as in Chapters 3 and 4. The VRC-TST calculations faced the same artificial limitation of VariFlex as described in Chapter 3 where the bonding length was shorter than the distance from the center of mass of $C_{15}H_9$ to the bonding atom. The surrogate reaction approach was used and C_6H_5 + O → C_6H_5O was selected as the surrogate reaction. Tables 6.1 and 6.2 show the calculated high-pressure-limit canonical rate coefficients at 2500 K as a function of bond length for the surrogate and actual reactions, respectively. The minimum reaction rate was found at a bonding distance of 1.4 Å, and the scaling factor needed to correct the microcanonical rate coefficients was found to be 0.44. The scaled microcanonical rate coefficients were used as inputs for the RRKM-ME computations.

Table 6.1. Canonical rates for phenyl + O → phenoxy at T = 2500 K at the high-pressure limit as a function of bond length.

r (Å)	k (cm^3 mol^{-1} s^{-1})
1.36	2.00E+13
1.40	1.99E+13
1.45	2.11E+13

1.50	2.30E+13
1.60	2.63E+13
1.70	2.97E+13
1.80	3.33E+13
1.90	3.72E+13
2.00	4.13E+13
2.10	4.57E+13
2.20	5.02E+13
2.25	5.24E+13

Table 6.2. Canonical rates for $C_{15}H_9 + O \rightarrow C_{15}H_9O$ at $T = 2500$ K at the high-pressure limit as a function of bond length.

r (Å)	k (cm^3 mol^{-1} s^{-1})
2.25	4.50E+13
2.30	4.71E+13
2.40	5.13E+13
2.50	5.56E+13
2.60	6.02E+13
2.80	7.00E+13
3.00	8.05E+13
3.20	9.16E+13
3.40	1.04E+14
4.00	1.44E+14
5.00	2.25E+14

The rate coefficients of the $C_{15}H_9 + O \rightarrow C_{14}H_9 + CO$ reaction were calculated using the MultiWell code. Figure 6.2 and Table 6.3 show the temperature-dependent rate coefficients for this reaction computed using each of the stretching potentials (B3LYP and CASPT2). The reaction did not exhibit any pressure-dependence over the range of 0.01 to 100 atm. The rate coefficients calculated using the B3LYP potential are higher than those computed using this CASPT2 by 8 %. The B3LYP potential is more attractive than the CASPT2 potential, so it is reasonable that the rate coefficient is slightly higher when the B3LYP potential is used. The choice of level of theory for the stretching potential only made a small difference to the rate coefficient, so the rate coefficient calculated using the

higher level of theory (CASPT2) was selected for the rate of five-member ring oxidation by O for the KMC model. The high-pressure rate coefficients for the elementary steps of the association of $C_{15}H_9 + O$ for calculations using the CASPT2 potential are presented in Table 6.4.

For the concentrations of O_2 and O present in high temperature oxidation of a stoichiometric H_2/O_2 mixture, the rate of five-member ring oxidation by O is faster than the rate of five-member ring oxidation by O_2 by over a factor of 10^4. While oxidation of six-member rings is faster by OH and O_2 than by O, for oxidation of five-member rings, O is the favored oxidizer.
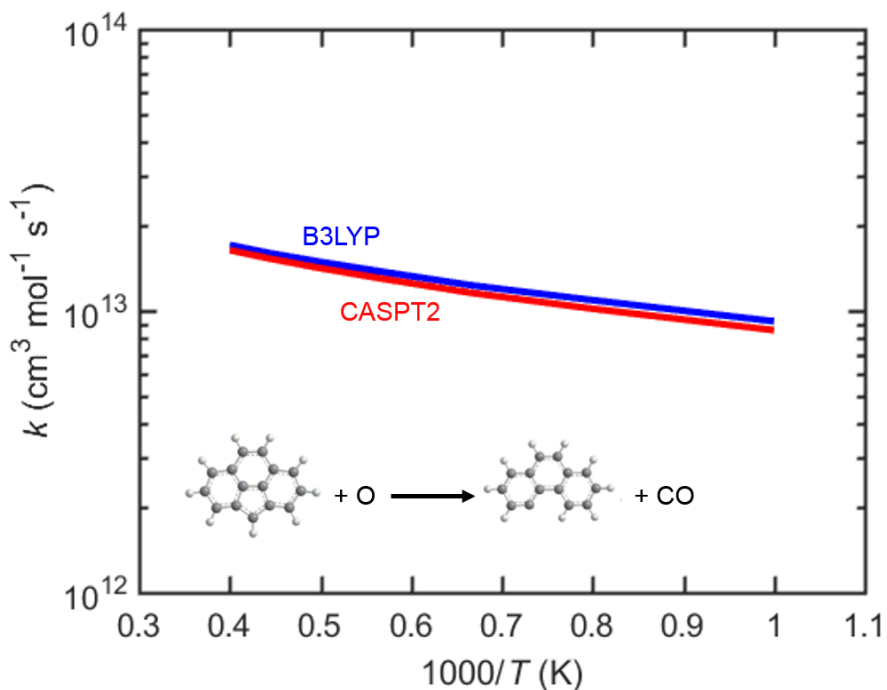
Figure 6.2. Computed rate coefficient for reaction $C_{15}H_9 + O \rightarrow C_{14}H_9 +$ CO.

Table 6.3. Rate coefficient for reaction $C_{15}H_9 + O \rightarrow C_{14}H_9 + CO$ at the two levels of theory for $p = 0.01 - 100$ atm.

	Level of theory	
T (K)	B3LYP	CASPT2
1000	9.2E+12	8.5E+12
1250	1.1E+13	1.0E+13
1500	1.2E+13	1.2E+13
1750	1.4E+13	1.3E+13

2000	1.5E+13	1.4E+13
2250	1.6E+13	1.5E+13
2500	1.7E+13	1.6E+13

Table 6.4. High-pressure rate coefficients (in s^{-1}) of the elementary steps for the association of $C_{15}H_9$ + O.

Reaction	1500 K	2000 K	2500 K
$C_{15}H_9O|i1 \rightarrow C_{15}H_9 + O$	1.6E+04	6.5E+06	2.3E+08
$C_{15}H_9O|i1 \rightarrow C_{15}H_9O|i6$	2.4E+10	1.3E+11	3.7E+11
$C_{15}H_9O|i6 \rightarrow C_{15}H_9O|i1$	3.1E+08	5.0E+09	2.7E+10
$C_{15}H_9O|i6 \rightarrow C_{15}H_9O|i7$	5.4E+10	2.5E+11	6.2E+11
$C_{15}H_9O|i7 \rightarrow C_{15}H_9O|i6$	2.9E+09	1.2E+10	2.9E+10
$C_{15}H_9O|i7 \rightarrow C_{14}H_9 + CO$	8.0E+10	5.8E+11	1.9E+12

6.4 Summary

Oxidation of five-member rings by O was found to be a faster pathway than oxidation of five-member rings by O_2. This reaction was added to the KMC oxidation model which was used for the simulations presented in Chapter 7.

7 KMC Simulations of High-Temperature Oxidation of Soot Particles in an H₂/O₂ Mixture

This chapter discusses how the KMC model developed in the previous chapters was coupled to a gas phase chemistry model, in order to simulate the oxidation of soot particles in an evolving gas phase environment. The new oxidation model was then tested at similar conditions to those used in shock tube experiments performed by Roth et al. [93].

7.1 Introduction

In Chapter 5, KMC simulations of graphene-edge surface oxidation using the newly established detailed oxidation model were shown to reproduce qualitative experimentally observed effects of graphene-edge curvature on the oxidation rate. The next step for testing the model was to test it quantitatively by comparing to experimentally-measured oxidation rates.

While many studies [94-106] have measured the oxidation rates of carbon species including chars, coals, or solid graphite, there have been considerably fewer studies [93, 107-109] directly measuring the oxidation rate of soot, especially at temperatures relevant to combustion. The most recent experiments to measure soot oxidation rates at high temperatures were performed by Paul Roth and co-workers [93, 107, 108]. In these studies, Roth and co-workers conducted shock tube experiments in which soot particles suspended in O_2/H_2/Ar gas mixtures were oxidized at high temperature conditions (1652 – 3130 K). A rapid tuning IR diode laser was employed to measure time-resolved CO/CO_2 concentration profiles and in situ laser light extinction measurements were performed to find particle size and number density. The particles were assumed to be spherical and the size distribution was assumed monodisperse. This allowed them to calculate the total intrinsic surface area per cm³ (a_{pi}). Oxidation rates (g cm⁻² s⁻¹) were calculated by dividing the rate of CO formation by the total intrinsic surface area per cm³. They found that for experiments in which soot particles were dispersed in Ar containing diluted stoichiometric H_2/O_2 mixtures, CO was the main gas phase reaction product.

In order to validate the KMC model of graphene-edge oxidation against their experimental results, I needed to modify the KMC code so that it could account for an evolving gas phase composition, and I needed to couple the surface chemistry to the gas phase chemistry, so that species consumed or produced through surface reactions could be added or subtracted from the gas phase.

7.2 Coupling of Surface and Gas Phase Chemistry

KMC simulations have been augmented from the version presented in Chapter 5 to include coupling between surface chemistry and gas phase chemistry. A Matlab model of a Plug Flow Reactor (PFR) developed by the Frenklach group [110] was chosen to simulate the gas phase chemistry of H_2/O_2 combustion. The gas phase mechanism of 10 species and 22 reactions is taken from You et al. [111] and is shown in Table 7.1.

Table 7.1. H_2/O_2 combustion mechanism employed in coupled KMC/PFR simulations.

	Reaction	Reference
1	$O + O + M \leftrightarrow O_2 + M$	[112]
2	$O + H + M \leftrightarrow OH + M$	[113]
3	$O + H_2 \leftrightarrow H + OH$	[112]
4	$O + HO_2 \leftrightarrow OH + O_2$	[112]
5	$O + H_2O_2 \leftrightarrow OH + HO_2$	[112]
6	$H + O_2 + M \leftrightarrow HO_2 + M$	[114, 115]
7	$H + O_2 \leftrightarrow O + OH$	[112]
8	$H + H + M \leftrightarrow H_2 + M$	[112]
9	$H + OH + M \leftrightarrow H_2O + M$	[112]
10	$H + HO_2 \leftrightarrow O + H_2O$	[112]
11	$H + HO_2 \leftrightarrow O_2 + H_2$	[116]
12	$H + HO_2 \leftrightarrow OH + OH$	[112]
13	$H + H_2O_2 \leftrightarrow HO_2 + H_2$	[112]
14	$H + H_2O_2 \leftrightarrow OH + H_2O$	[112]
15	$OH + H_2 \leftrightarrow H + H_2O$	[112]
16	$OH + OH + M \leftrightarrow H_2O_2 + M$	[117, 118]
17	$OH + OH \leftrightarrow O + H_2O$	[112]
18	$OH + HO_2 \leftrightarrow O_2 + H_2O$	[119]
19	$OH + H_2O_2 \leftrightarrow HO_2 + H_2O$	[117]
20	$HO_2 + HO_2 \leftrightarrow O_2 + H_2O_2$	[112]
21	$O + OH + M \leftrightarrow HO_2 + M$	[120, 121]
22	$OH + CO \leftrightarrow H + CO_2$	[122]

At the start of oxidation ($t_0 = 0$ ms), the KMC and PFR is initialized in parallel with the gas phase conditions (T, P, x_{O2}, x_{H2}) from Roth et al. [93]. x_{C2H2} and x_H are assumed to be 0 at the onset of oxidation. The KMC model begins with an initial substrate, the selection of which is discussed in Section 7.3.1. The surface chemistry starts with the first KMC reaction taking place over the interval Δt_{KMC}, which would be determined using the algorithm described in Section 2.2. The most basic way to couple the KMC and PFR would be for the PFR to be simulated for $\Delta t_{PFR} = \Delta t_{KMC}$, and for the gas phase environment of the KMC to be updated after every KMC time step. However, this method would be computationally expensive as KMC time steps can be on the order of 10^{-7} s. Instead, a fixed time step of 10 μs was selected for Δt_{PFR}. The time step was large enough to reduce computational time and small enough so that further reductions in Δt_{PFR} did not affect the simulation results.

Using this method with different step sizes for the PFR and KMC, the gas phase evolution is simulated for a residence time of Δt_{PFR}, and the surface chemistry is simulated in the KMC model for a duration of Δt_{PFR}. During this time, the gas phase environment remains constant with the gas phase conditions from $t_0 = 0$. The reaction counts during this time interval are recorded in order to calculate how many molecules are added to or removed from the gas phase by surface reactions. For example, when reaction $R\cdot + O_2 \rightarrow R\text{-}O + O$ occurs, one O_2 molecule is removed from the gas phase and one O atom is added.

At $t_1 = t_0 + \Delta t_{PFR}$, the gas phase concentrations from the PFR simulation are updated based on the change in gas phase species (H, H_2, O, O_2, OH, H_2O, HO_2, CO, and CO_2) due to surface reactions. The following equation is used to calculate the change in concentrations,

$$\Delta[H] = \frac{\text{net H atoms produced in KMC}}{1} \times \frac{1}{N_{\text{sites}}} \times \frac{2.3 \times 10^{15} \text{ sites}}{\text{cm}^2} \times \frac{1 \text{ mol}}{N_A \text{ H atoms}} \times \frac{a_p \text{ cm}^2}{1 \text{ cm}^3} , \qquad (2)$$

where N_{sites} is the number of active edge sites of the KMC substrate, 2.3×10^{15} is the number density of C-H sites on soot surfaces as estimated in [14], N_A is Avogadro's number, and a_p is the reacting particle area specified in [93]. The updated gas phase conditions (T, P, x_H, x_{H2}, x_O, x_{O2}, x_{OH}, and x_{H2O}) are set as the new gas phase environment for the KMC simulation for the next Δt_{PFR}. They are also used as the initial values for the next PFR step. Figure 7.1 shows a diagram of the coupling between the PFR and KMC simulations.
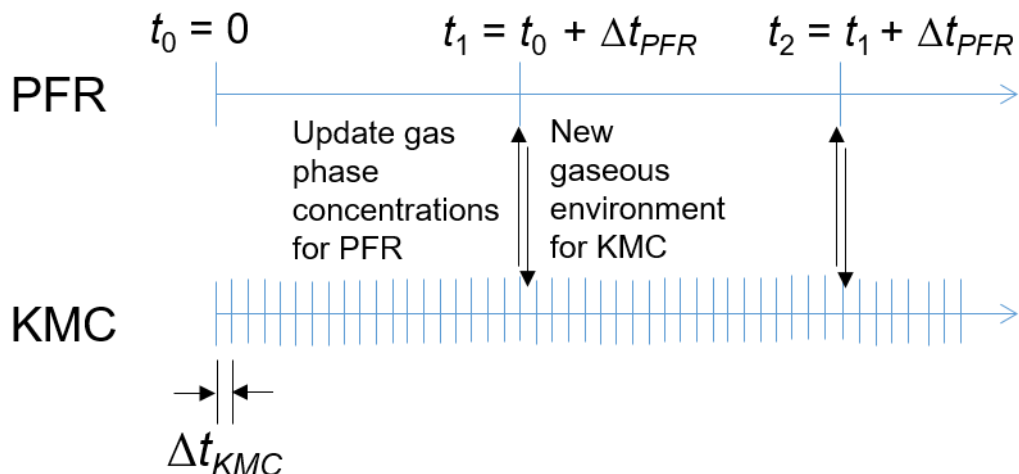
Figure 7.1. Diagram of the coupling between gas phase and surface chemistry.

For some gas phase compositions, it is possible that the time steps for the KMC could exceed the time step for the PFR. As a contingency for those cases, if $\Delta t_{KMC} > \Delta t_{PFR}$, then the gas phase is simulated for Δt_{PFR}, the KMC gaseous environment is updated with PFR results from $t_0 + \Delta t_{PFR}$, and the KMC simulation is advanced to $t_0 + \Delta t_{PFR}$ without a KMC reaction occurring at that step. The KMC reaction counts are reset to zero at the start of each Δt_{PFR} interval. The coupling process is repeated until the end of the KMC simulation. During oxidation, when the substrate is oxidized down to one ring, the substrate is instantly regrown to the initial substrate and the one ring is assumed to instantly fall apart and produce 6 CO molecules and 6 H atoms while consuming 3 O_2 molecules.

To see how the assumption of the final ring falling apart would affect the results, two test cases were performed with an initial substrate of circumcoronene, one where the final ring was assumed to fall apart, and one where it did not fall apart. Figure 7.2 shows time-dependent [CO] and [CO_2] profiles for the test cases and reveals that the concentrations of these species changed by less than 5 % meaning that this assumption has little effect on the results.
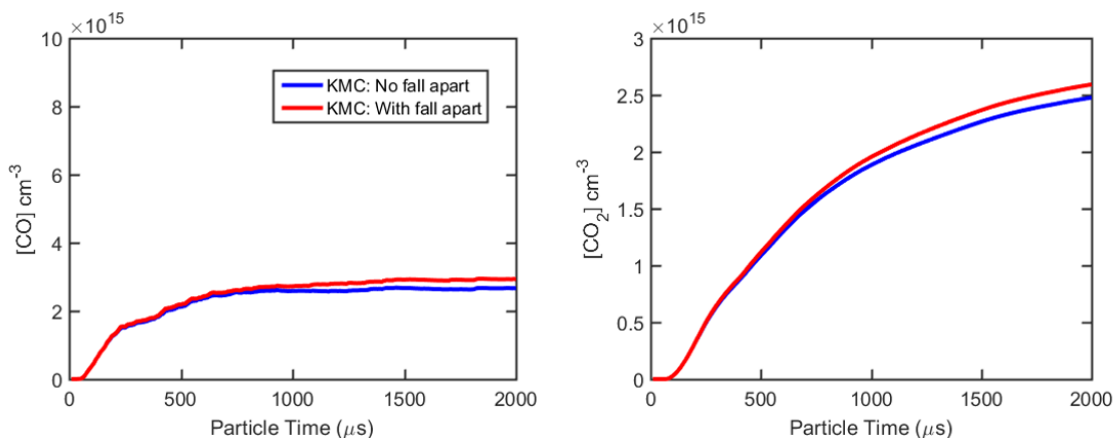
Figure 7.2. CO and CO_2 concentration versus time for test cases where the final ring can either fall apart to produce CO and H or not.

The set of surface reactions employed in the KMC model has been augmented from the 45 growth and 45 oxidation reactions utilized in the calculations from Chapter 5 to include reactions 91 – 104. Reactions 2, 11, and 13 were split into two separate reactions to account for the two ways that each of those reactions consumes or produces gas phase species. The full set of reactions is given in Table 2.1.

7.3 KMC Simulations

KMC simulations were performed using the gas phase conditions specified in Figure 7 of Roth et al. [93] for a soot/O_2/H_2/Ar mixture: $T = 1990$ K, $P = 0.72$ bar, $P_{O2} = 8 \times 10^{-3}$ bar, $P_{O2}/P_{H2} = 0.5$, and $a_p = 0.23$ cm^2/cm^3. This set of conditions was chosen because Roth et al. [93] provided the most results for this particular experiment. Each numerical simulation lasted for 2 ms, and Δt_{PFR} was selected to be 10 μs.

A set of simulations was also performed for only the gas phase reactions occurring in the PFR. In these simulations, benzene acts as soot instead of the graphene susbtrates used in the coupled KMC/PFR simulations. The benzene can undergo hydrogen abstraction to produce phenyl, which can in turn be oxidized to form C_5H_5. As soon as the five-member ring is formed, the molecule is immediately transformed back to benzene and the oxidation process can start over. By modeling the instant refreshing of C-H sites, the PFR model neglects steric effects and thus oxidation can only be limited by a decrease in the concentration of oxidizers (O_2, OH, O). Therefore, the uncoupled PFR simulations can be thought of as an upper limit on the oxidation rate. The coupled KMC/PFR model takes into account steric effects and the changing of the gas phase composition, which causes it to have a lower oxidation rate.

7.3.1 Effect of Initial Substrate Size and Shape

Five initial substrates were studied to determine the effects of substrate size and shape: coronene (7 rings), circumcoronene (19 rings), circumcircumcoronene (37 rings),

circumcircumcircumcoronene (61 rings), and a 5×5 ring rhombus (25 rings). The five substrates are shown in Figure 7.3.

Coronene: 7 rings   Circumcoronene: 19 rings   5 × 5 rhombus: 25 rings

Circumcircumcoronene: 37 rings   Circumcircumcircumcoronene: 61 rings
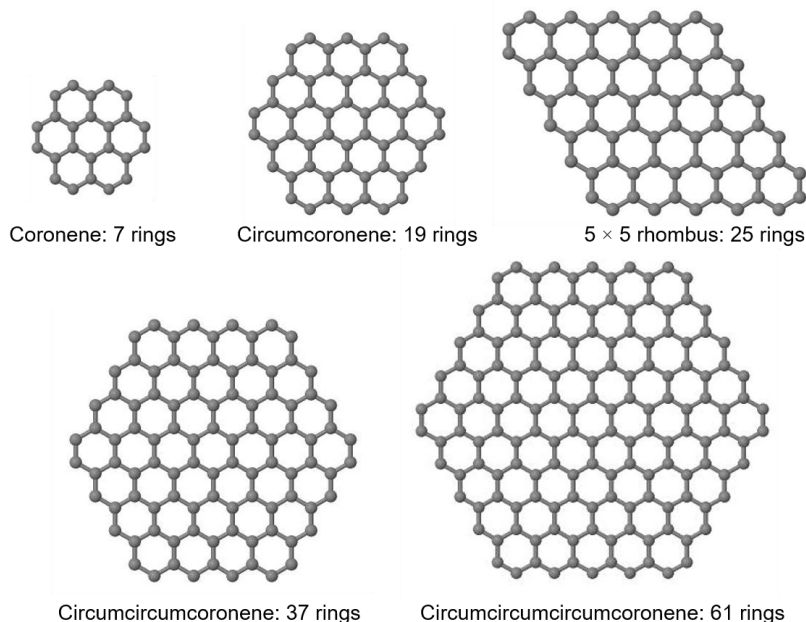
Figure 7.3. Initial substrates for KMC simulations. The H atoms saturating the edge carbon atoms are not shown for clarity.

Gas phase concentration profiles of each of the 10 species were computed from a series of 50 simulation runs performed with different seeds for the random number generator for each substrate. Figure 7.4 shows the effect of initial substrate size on CO and CO_2 concentration profiles. The black line in Figure 7.4 comes from PFR simulations that are not coupled to surface chemistry. The black markers in Figure 7.4 are experimentally-measured data points from Figure 7 of Roth et al. [93].
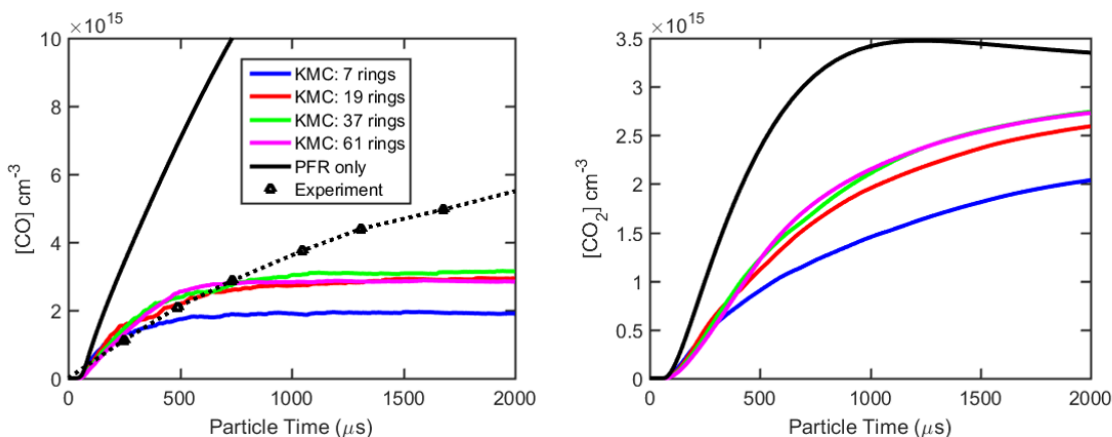
Figure 7.4. CO and CO_2 concentration versus time for KMC simulations with different initial substrate sizes.

Figure 7.4 shows the effects on the magnitude and shape of the CO and CO_2 concentration profiles by changing the initial substrate size. Although the production of CO and CO_2

increase as the substrate size increases from seven rings to 19, further increases to substrate size have no significant effect on formation rates of CO or CO_2. Based on the concentration profiles alone, it is tempting to assume that the oxidation behavior is the exactly the same for the cases with the three largest initial substrate sizes. However, one must look at the underlying reaction statistics in order to get a more detailed understanding of the oxidation kinetics. The reaction counts for these simulations sets can be seen in Table 7.2.

Table 7.2. Reaction counts for KMC simulations with different initial substrate size.

Reaction	Initial substrate size (rings)			
	7	19	37	61
1	173.9	160.9	170.2	194.2
2a	399.3	366.3	391.1	436.0
2b	9.4	9.0	9.8	10.8
3	0.0	0.0	0.0	0.0
4	0.0	0.0	0.0	0.0
5	6.9	18.5	18.3	22.6
6	3.1	7.1	9.6	12.4
7	1.3	4.2	4.6	7.0
8	5.8	18.0	21.8	28.5
9	0.2	1.7	2.9	4.1
10	10.7	30.5	41.5	67.1
11a	10.4	29.4	40.5	65.1
11b	0.3	1.1	1.0	1.9
12	24.8	67.1	88.7	146.8
13a	20.1	47.4	66.8	115.7
13b	0.0	0.0	0.1	0.1
14	0.0	0.0	0.0	0.0
15	0.0	0.8	1.4	2.6
16	0.5	2.1	2.6	3.5
17	0.2	1.3	1.0	1.8
18	0.0	0.0	0.0	0.0
19	0.0	0.0	0.0	0.0
20	0.0	0.0	0.0	0.0
21	0.5	0.7	0.5	0.4
22	0.0	0.4	0.3	0.2
23	0.6	0.6	0.4	0.3
24	2.3	3.2	2.0	1.7
25	0.7	0.7	0.4	0.5
26	0.0	0.0	0.0	0.0
27	0.0	0.0	0.0	0.0
28	0.0	0.0	0.0	0.0
29	0.1	0.1	0.1	0.1
30	0.0	0.0	0.0	0.0

31	0.0	0.1	0.5	0.8
32	0.0	0.0	0.1	0.2
33	0.0	0.0	0.0	0.0
34	0.0	0.0	0.0	0.0
35	0.0	0.0	0.0	0.0
36	0.0	0.0	0.0	0.0
37	0.0	0.0	0.0	0.0
38	0.0	0.0	0.0	0.0
39	0.0	0.0	0.0	0.0
40	0.0	0.0	0.0	0.0
41	0.0	0.0	0.0	0.0
42	0.0	0.0	0.0	0.0
43	0.0	0.0	0.0	0.0
44	0.0	0.0	0.0	0.0
45	1.2	0.7	0.3	0.2
46	0.1	0.4	0.3	0.4
47	0.4	0.9	0.5	0.7
48	1.1	1.7	1.9	2.8
49	0.9	1.8	2.6	3.6
50	0.2	7.7	16.4	31.1
51	0.3	1.4	1.3	1.5
52	1.2	3.4	3.7	4.2
53	2.8	5.8	8.4	12.1
54	3.0	6.3	8.3	15.3
55	0.4	1.5	1.6	1.7
56	1.2	3.9	4.6	4.7
57	2.0	4.9	6.8	13.1
58	2.2	5.3	7.8	14.0
59	1.0	38.7	68.2	153.0
60	0.2	0.9	0.9	1.0
61	0.7	2.3	2.6	3.0
62	1.2	3.3	5.1	8.9
63	1.4	3.3	4.7	8.0
64	2.1	114.0	162.4	400.2
65	0.0	0.1	0.0	0.1
66	0.1	0.3	0.3	0.6
67	0.3	0.5	0.8	1.5
68	0.3	0.4	0.6	1.2
69	2.4	125.4	186.8	446.2
70	0.0	0.1	0.1	0.1
71	0.0	0.1	0.1	0.1
72	0.1	0.2	0.1	0.5
73	0.1	0.2	0.1	0.4
74	0.1	6.5	8.4	20.4
75	0.0	0.1	0.2	0.0

76	0.1	0.2	0.2	0.2
77	0.1	0.2	0.2	0.5
78	0.1	0.2	0.4	0.6
79	0.1	3.8	6.9	13.4
80	0.0	0.0	0.0	0.0
81	0.0	0.0	0.0	0.0
82	0.0	0.0	0.0	0.0
83	0.0	0.0	0.0	0.0
84	0.0	2.1	2.8	6.7
85	0.2	0.9	0.6	0.8
86	0.5	1.6	2.1	2.1
87	1.0	2.3	3.3	6.6
88	1.0	2.2	3.3	6.1
89	1.1	40.4	78.2	169.3
90	0.0	0.0	0.0	0.0
91	0.0	0.0	0.0	0.0
92	235.4	206.6	220.8	235.6
93	0.1	0.3	0.7	0.8
94	1.6	2.5	2.7	4.8
95	0.1	2.6	4.7	9.5
96	0.4	1.5	1.5	2.0
97	1.1	3.2	3.2	4.5
98	1.7	4.6	7.0	13.3
99	1.8	4.5	6.8	9.9
100	0.0	0.1	0.2	0.1
101	0.2	0.3	0.3	0.3
102	0.1	0.6	0.5	1.1
103	0.2	0.5	0.6	1.1
104	6.5	15.8	24.1	41.0

In the current KMC model, carbon can be removed from the graphene edge via oxidation by O_2 (reactions 51-54 and 90), OH (reactions 96-99), H_2O (reactions 100-103), O (reaction 104), or via thermal desorption (reactions 5, 7, 17, 25, and 45). The reaction statistics for oxidation and thermal desorption reactions illustrated in Figure 7.5 and presented in Table 7.3 provide insight into how the kinetics are affected by initial substrate size.
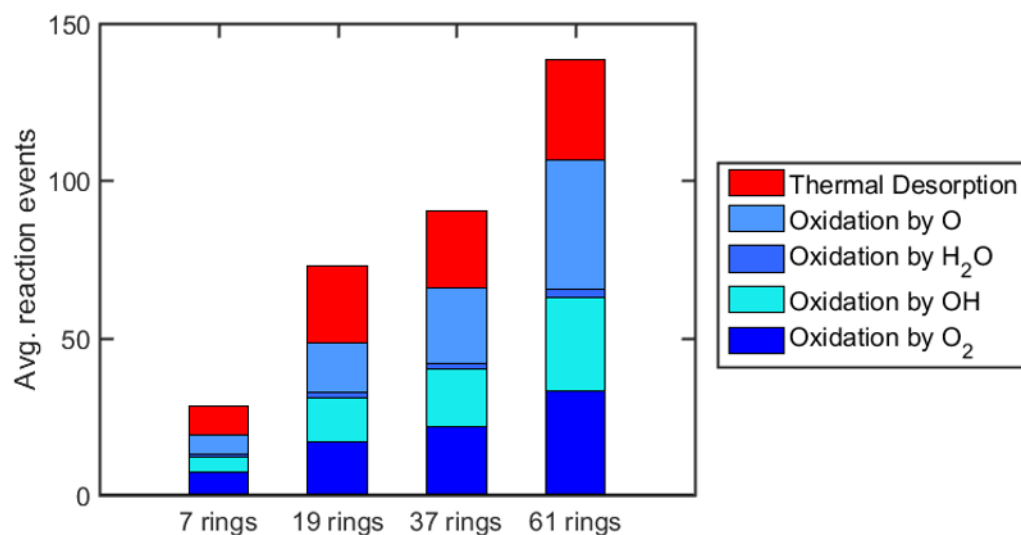
Figure 7.5. Event counts for oxidation and thermal desorption reactions for KMC simulations with different initial substrate sizes.

Table 7.3. Event counts for oxidation and thermal desorption reactions for KMC simulations with different initial substrate sizes.

Reactions	Initial substrate size (rings)			
	7	19	37	61
Oxidation by O_2: R51 – R54, R90	7.2	17.0	21.7	33.0
Oxidation by OH: R96-R99	5.0	13.9	18.5	29.7
Oxidation by H_2O: R100-R103	0.5	1.5	1.6	2.7
Oxidation by O: R104	6.5	15.8	24.1	41.0
Thermal desorption: R5, R7, R17, R25, R45	9.0	24.7	24.3	31.9

The reaction counts in Table 7.3 show that as the initial substrate size increases, the frequency of oxidation and thermal desorption reactions increases. This result is expected due to an increase in the number of edge carbon sites and does not reveal much on its own. To gain a better understanding of the relationship between the reactions that remove carbon, the data from Table 7.3 can be recast in terms of the share of carbon atoms removed by each type of reaction as shown in Figure 7.6 and Table 7.4.
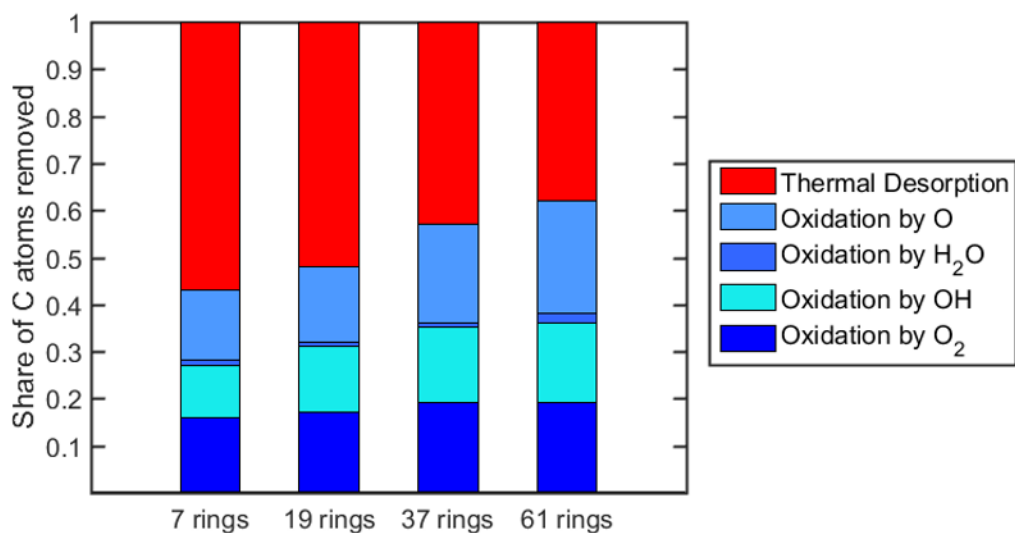
Figure 7.6. Share of carbon atoms removed from the substrate by oxidation and thermal desorption reactions for KMC simulations with different initial substrate size.

Table 7.4. Share of carbon atoms removed from the substrate by oxidation and thermal desorption reactions for KMC simulations with different initial substrate size.

	Initial substrate size (rings)			
Reactions	7	19	37	61
Oxidation by O_2: R51 – R54, R90	16%	17%	19%	19%
Oxidation by OH: R96-R99	11%	14%	16%	17%
Oxidation by H_2O: R100-R103	1%	1%	1%	2%
Oxidation by O: R104	15%	16%	21%	24%
Thermal desorption: R5, R7, R17, R25, R45	57%	53%	43%	38%

The data in Table 7.4 show that the oxidation behavior does change slightly as the initial substrate size increases. A tradeoff occurs between thermal desorption reactions, which account for 57 % of the carbon atoms removed for the smallest initial substrate case, and oxidation reactions which remove 62 % of the carbon atoms for the largest initial substrate case. While the oxidation behavior is not exactly the same for the different cases, the shift between relative frequencies of oxidation and thermal desorption reactions does not manifest in different CO and CO_2 concentration profiles indicating that the oxidation rate is not very sensitive to initial substrate size.

KMC simulations were also performed using a rhombus-shaped graphene substrate in order to see if substrate shape would affect the results. Figure 7.7 shows a comparison of CO and CO_2 concentration profiles between simulations using the rhombus substrate and simulations with circumcoronene and circumcircumcoronene. The species concentration profiles are similar for all three sets of simulations indicating that CO and CO_2 formation

are not significantly affected by the shape of the initial substrate. The reaction statistics for simulations with the rhombus initial substrate are shown in Table 7.5. Figure 7.8 and Table 7.6 show the share of carbon atoms removed by oxidation and thermal desorption for these simulations.
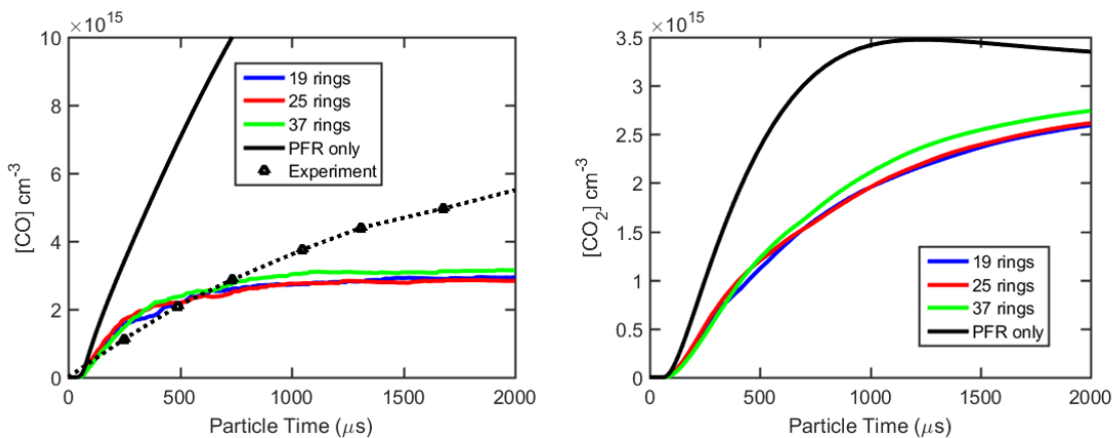
Figure 7.7. CO and CO_2 concentration versus time for KMC simulations with different initial substrate shapes.

Table 7.5. Event counts for KMC simulations with an initial substrate of a rhombus.

Reaction	Initial Substrate Size (rings) 25
1	167.0
2a	374.9
2b	9.0
3	0.0
4	0.0
5	20.7
6	8.4
7	5.5
8	21.5
9	1.5
10	34.0
11a	33.1
11b	0.8
12	73.8
13a	50.3
13b	0.0
14	0.0
15	0.7
16	2.3

17	1.2
18	0.0
19	0.0
20	0.0
21	0.6
22	0.3
23	0.5
24	2.8
25	0.8
26	0.0
27	0.0
28	0.0
29	0.1
30	0.2
31	0.2
32	0.1
33	0.0
34	0.0
35	0.0
36	0.0
37	0.0
38	0.0
39	0.0
40	0.0
41	0.0
42	0.0
43	0.0
44	0.0
45	0.8
46	0.7
47	1.3
48	1.3
49	1.6
50	13.8
51	2.1
52	5.0
53	5.8
54	6.5
55	2.4
56	5.0
57	5.8
58	6.3
59	61.0
60	1.4
61	2.9

|	
62	3.6
63	4.3
64	169.5
65	0.2
66	0.4
67	0.5
68	0.7
69	188.7
70	0.1
71	0.0
72	0.2
73	0.1
74	8.5
75	0.1
76	0.1
77	0.1
78	0.2
79	5.4
80	0.0
81	0.0
82	0.0
83	0.0
84	3.3
85	1.1
86	2.5
87	3.0
88	2.9
89	67.9
90	0.0
91	0.0
92	207.6
93	0.9
94	1.7
95	4.4
96	2.0
97	4.0
98	6.0
99	5.4
100	0.2
101	0.3
102	0.4
103	0.5
104	17.5
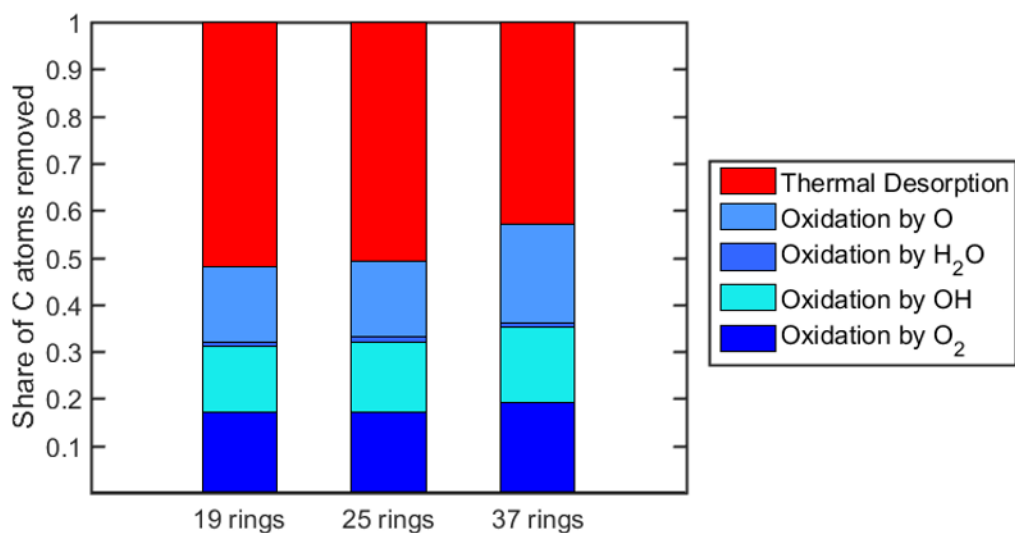
Figure 7.8. Share of carbon atoms removed from the substrate by oxidation and thermal desorption reactions for KMC simulations with different initial substrate shape.

Table 7.6. Share of carbon atoms removed from the substrate by oxidation and thermal desorption reactions for KMC simulations with different initial substrate shape.

	Initial substrate size (rings)		
Reactions	19	25	37
Oxidation by O_2: R51 – R54, R90	17%	17%	19%
Oxidation by OH: R96-R99	14%	15%	16%
Oxidation by H_2O: R100-R103	1%	1%	1%
Oxidation by O: R104	16%	15%	21%
Thermal desorption: R5, R7, R17, R25, R45	53%	52%	43%

The oxidation behavior shown in Figure 7.8 and Table 7.6 for the case with the rhombus substrate is similar to the kinetics exhibited by the cases with substrates of 19 and 37 rings. The fact that the oxidation rate is not highly dependent on either substrate size or shape justifies the choice of using circumcoronene as the initial substrate for the rest of the simulations presented in this chapter.

7.3.2 Effect of Extent of Oxidation Allowed

In the simulations discussed in the previous section, the initial substrate was oxidized down to one ring before it was replaced by a new substrate. However, the reality may be that the outermost layer of the soot surface would not have to be completely oxidized before oxidation would start to take place at the next layer. To test the sensitivity of CO formation to the extent of oxidation allowed before continuing on to the next substrate, different limits

of oxidation were implemented beyond which oxidation would continue with a new substrate. For example, if the initial substrate was circumcoronene ($C_{54}H_{18}$) and the extent of oxidation allowed was set at 50 %, whenever the substrate size would decrease to less than 27 C atoms, a new circumcoronene substrate would be instantly regenerated. Thresholds of 5, 10, 25, 50, and 100 % were tested and the initial substrate was chosen to be circumcoronene. The scenario of 100 % oxidation allowed corresponds with oxidation continuing until one ring remains, and that ring is assumed to fall apart instantly as shown in the results in the previous section. Table 7.7 shows the resulting reaction counts for these simulations.

Table 7.7. Reaction counts for KMC simulations with different extents of oxidation allowed.

Reaction	Extent of oxidation allowed (%)				
	5	10	25	50	100
1	243.8	192.2	161.9	151.3	160.9
2a	200.6	221.5	283.3	299.8	366.3
2b	6.0	6.5	7.3	7.9	9.0
3	0.0	0.0	0.0	0.0	0.0
4	0.0	0.0	0.0	0.0	0.0
5	0.2	1.6	15.2	30.8	18.5
6	0.1	0.9	9.1	15.7	7.1
7	0.3	1.2	7.6	9.8	4.2
8	1.1	5.3	32.7	42.8	18.0
9	0.3	0.8	3.7	4.7	1.7
10	77.6	90.8	86.4	78.2	30.5
11a	64.6	82.6	81.3	74.6	29.4
11b	2.3	3.2	3.3	3.1	1.1
12	174.6	196.0	187.7	167.6	67.1
13a	37.9	80.9	111.3	103.8	47.4
13b	0.0	0.1	0.1	0.1	0.0
14	0.0	0.0	0.0	0.0	0.0
15	0.3	1.3	4.8	3.3	0.8
16	0.4	1.4	7.7	8.7	2.1
17	0.2	0.6	3.4	3.8	1.3
18	0.0	0.0	0.0	0.0	0.0
19	0.0	0.0	0.0	0.0	0.0
20	0.0	0.0	0.0	0.0	0.0
21	0.0	0.0	0.5	1.0	0.7
22	0.0	0.1	0.9	1.4	0.4
23	0.0	0.0	0.2	0.4	0.6
24	0.0	0.1	1.2	2.7	3.2
25	0.0	0.0	0.1	0.6	0.7
26	0.0	0.0	0.0	0.0	0.0
27	0.0	0.0	0.0	0.0	0.0

28	0.0	0.0	0.0	0.0	0.0
29	0.0	0.1	0.3	0.3	0.1
30	0.0	0.0	0.0	0.0	0.0
31	1.5	1.5	0.7	0.7	0.1
32	0.0	0.1	0.0	0.1	0.0
33	0.0	0.0	0.0	0.0	0.0
34	0.0	0.0	0.0	0.0	0.0
35	0.0	0.0	0.0	0.0	0.0
36	0.0	0.0	0.0	0.0	0.0
37	0.0	0.0	0.0	0.0	0.0
38	0.0	0.0	0.0	0.0	0.0
39	0.0	0.0	0.0	0.0	0.0
40	0.0	0.0	0.0	0.0	0.0
41	0.0	0.0	0.0	0.0	0.0
42	0.0	0.0	0.0	0.0	0.0
43	0.0	0.0	0.0	0.0	0.0
44	0.0	0.0	0.0	0.0	0.0
45	0.0	0.0	0.0	0.0	0.7
46	0.0	0.2	0.4	0.6	0.4
47	0.0	0.3	0.9	1.1	0.9
48	8.8	7.2	4.0	3.4	1.7
49	9.8	7.2	4.2	3.1	1.8
50	15.3	12.1	11.6	11.5	7.7
51	0.2	0.7	2.5	3.0	1.4
52	0.5	1.2	4.8	6.1	3.4
53	66.1	48.2	24.4	16.5	5.8
54	65.6	49.7	26.2	17.5	6.3
55	0.3	0.7	2.8	2.8	1.5
56	0.9	1.8	5.8	7.1	3.9
57	63.7	47.1	23.0	15.0	4.9
58	72.1	50.8	24.5	16.7	5.3
59	121.7	84.4	79.0	74.4	38.7
60	0.2	0.4	1.9	2.2	0.9
61	0.5	0.9	3.3	4.7	2.3
62	40.3	30.7	15.4	10.1	3.3
63	46.4	32.4	16.2	10.9	3.3
64	272.8	193.6	205.2	196.8	114.0
65	0.0	0.0	0.1	0.1	0.1
66	0.1	0.1	0.4	0.7	0.3
67	5.4	3.5	1.7	1.3	0.5
68	5.1	3.9	2.0	1.1	0.4
69	297.9	214.2	221.2	213.6	125.4
70	0.0	0.0	0.1	0.1	0.1
71	0.0	0.0	0.2	0.3	0.1
72	2.2	1.8	0.9	0.6	0.2

73	2.4	1.4	0.7	0.7	0.2
74	15.2	9.7	11.1	10.1	6.5
75	0.0	0.0	0.1	0.1	0.1
76	0.0	0.1	0.3	0.3	0.2
77	2.0	1.1	0.8	0.5	0.2
78	2.3	1.4	0.6	0.7	0.2
79	9.6	6.9	6.0	6.3	3.8
80	0.0	0.0	0.0	0.0	0.0
81	0.0	0.0	0.0	0.0	0.0
82	0.0	0.0	0.0	0.0	0.0
83	0.0	0.0	0.1	0.0	0.0
84	5.7	3.0	3.7	3.7	2.1
85	0.1	0.3	1.2	1.4	0.9
86	0.4	0.9	2.4	2.5	1.6
87	23.7	18.0	8.3	5.9	2.3
88	25.4	18.8	9.0	6.0	2.2
89	114.5	83.3	75.6	74.7	40.4
90	0.0	0.0	0.0	0.0	0.0
91	0.0	0.0	0.0	0.0	0.0
92	229.3	199.6	178.7	162.7	206.6
93	0.1	0.1	0.7	0.7	0.3
94	34.6	25.5	12.7	7.0	2.5
95	13.1	8.6	5.6	4.7	2.6
96	0.3	0.6	2.3	2.9	1.5
97	0.4	1.4	4.9	6.1	3.2
98	60.1	44.8	22.9	14.2	4.6
99	57.4	43.0	20.3	13.7	4.5
100	0.0	0.0	0.2	0.3	0.1
101	0.1	0.1	0.4	0.7	0.3
102	11.2	6.5	2.8	2.3	0.6
103	10.8	6.9	3.0	2.0	0.5
104	42.1	48.1	42.7	33.7	15.8

Figure 7.9 shows that CO and CO_2 formation increase as the extent of oxidation allowed before creating a new substrate decreases. This result is consistent with the analysis presented in Chapter 5 which states that oxidation rate decreases over time. By limiting the extent of oxidation allowed and regenerating a new substrate earlier in the oxidation process, the overall oxidation rate will be higher and more product formation will occur. Figure 7.9 shows that as the extent of oxidation allowed is decreased towards 5 %, the CO concentration profile moves closer to the PFR profile. This result is expected as the PFR scenario assumes a constant replenishment of C-H sites for any amount of oxidation and is essentially a minimum case for the extent of oxidation allowed.
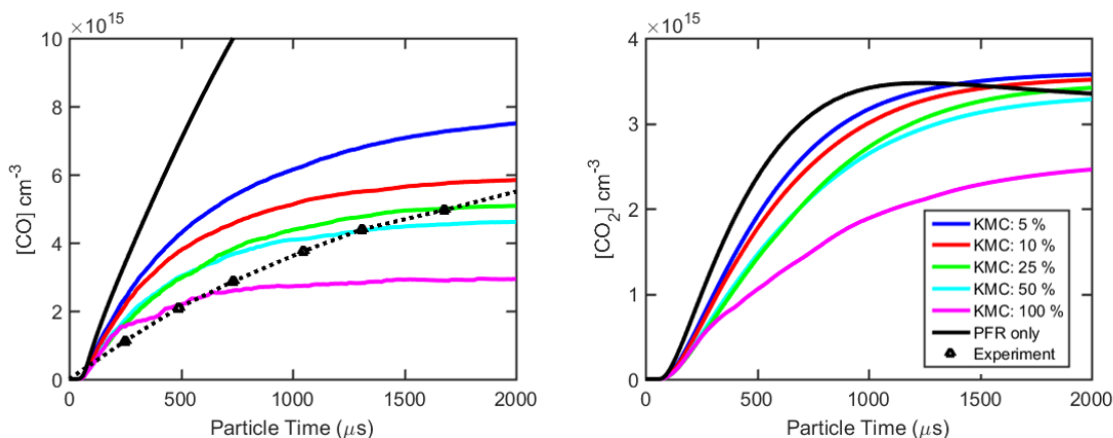
Figure 7.9. CO and CO$_2$ concentration versus time for KMC simulations with different extents of oxidation allowed. Circumcoronene was the initial substrate.

Figure 7.10. Event counts for oxidation and thermal desorption reactions for KMC simulations with different extents of oxidation allowed.

Table 7.8. Event counts for oxidation and thermal desorption reactions for KMC simulations with different extents of oxidation allowed.

Reactions	Extent of oxidation allowed (%)				
	5	10	25	50	100
Oxidation by O$_2$: 51 – 54, 90	132.4	99.7	57.9	43.1	17.0
Oxidation by OH: 96 – 99	118.2	89.8	50.4	36.8	13.9
Oxidation by H$_2$O: 100 – 103	22.0	13.6	6.4	5.3	1.5
Oxidation by O: 104	42.1	48.1	42.7	33.7	15.8
Thermal desorption: 5, 7, 17, 25, 45	0.8	3.3	26.3	45.0	24.7

135

The reaction counts for oxidation and thermal desorption reactions for each of the simulations are shown in Figure 7.10 and Table 7.8. As the extent of oxidation allowed decreases, the number of event counts for oxidation reactions increases with the majority of oxidation occurring by O_2 and OH. In contrast to the trend for oxidation reactions, the number of thermal desorption reactions decreases sharply as the extent of oxidation is decreased. The tradeoff between oxidation and thermal desorption is made even clearer when looking at the share of carbon atoms removed by each type of reaction as shown in Figure 7.11 and Table 7.9.

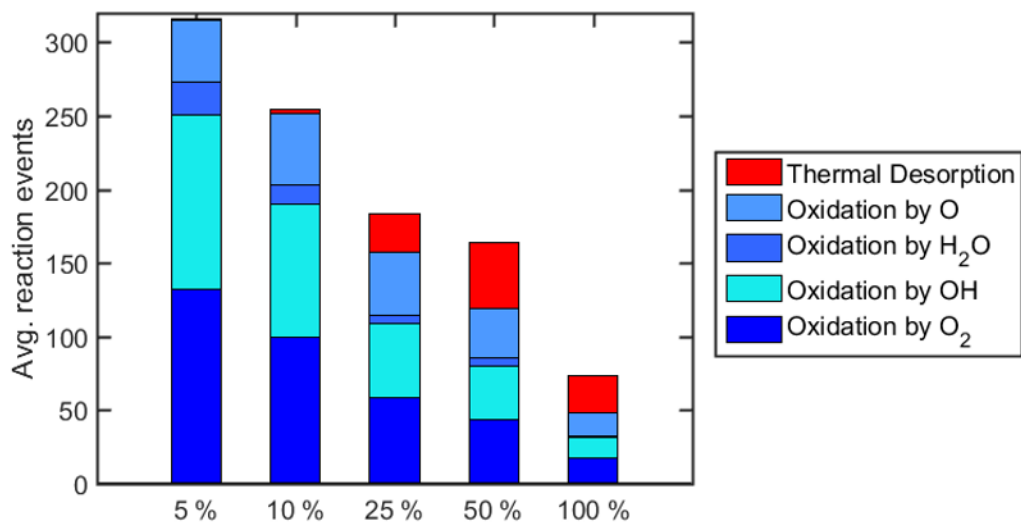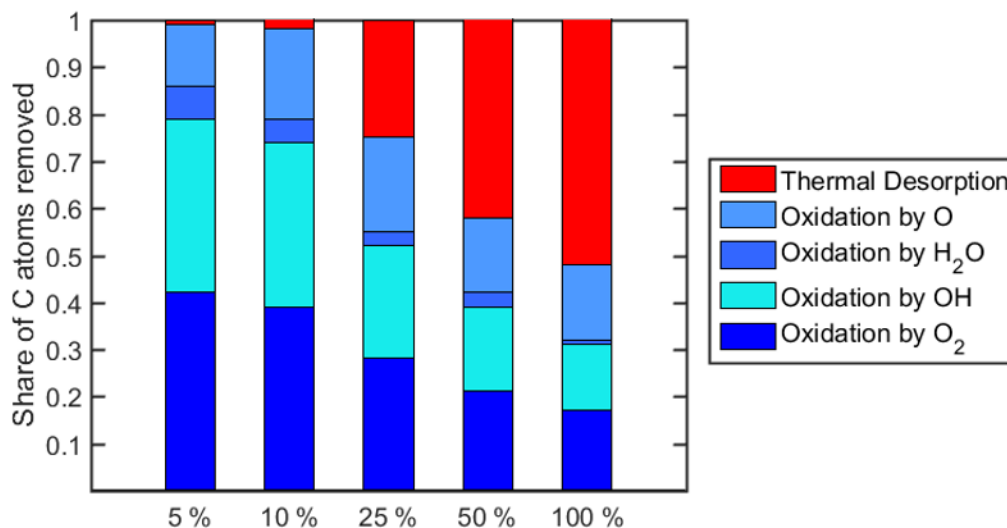Figure 7.11. Share of carbon atoms removed by oxidation and thermal desorption reactions for KMC simulations with different extents of oxidation allowed.

Table 7.9. Share of carbon atoms removed by oxidation and thermal desorption reactions for KMC simulations with different extents of oxidation allowed.

	Extent of oxidation allowed (%)				
Reactions	5	10	25	50	100
Oxidation by O_2: 51 – 54, 90	42%	39%	28%	21%	17%
Oxidation by OH: 96 – 99	37%	35%	24%	18%	14%
Oxidation by H_2O: 100 – 103	7%	5%	3%	3%	1%
Oxidation by O: 104	13%	19%	20%	16%	16%
Thermal desorption: 5, 7, 17, 25, 45	0%	3%	25%	43%	53%

Figure 7.11 reveals the relative order of the mechanisms which remove carbon. Oxidation of six-member rings by O_2 and OH occurs at the onset of oxidation followed by oxidation of five-member rings by O which precedes thermal desorption reactions. These results are consistent with the findings from Chapter 5 that the oxidation behavior of graphene edges changes over time.

7.3.3 Effect of Atomic Hydrogen Production

In the shock tube experiments conducted by Roth et al. [93], the concentration of atomic hydrogen was not measured. It is known that minute quantities of impurities adsorbed to the walls of a shock tube can generate a non-negligible amount of hydrogen atoms upon shock heating, and the additional hydrogen atoms can greatly affect the kinetics of the mixture being tested [123, 124]. Roth et al. did not measure hydrogen atom concentration, so it is possible that hydrogen atoms could have been produced by this mechanism. To simulate this phenomenon, a source term was added to Equation 2 which would allow for a constant rate of production of hydrogen atoms. Equation 3 shows the modified expression for updating the hydrogen concentration.

$$\Delta[H] = \frac{\text{net H atoms produced in KMC}}{1} \times \frac{1}{N_{\text{sites}}} \times \frac{2.3 \times 10^{15}\ \text{sites}}{\text{cm}^2} \times \frac{1\ \text{mol}}{N_A\ \text{H atoms}} \times \frac{a_p\ \text{cm}^2}{1\ \text{cm}^3} + H_{\text{prod}} , \quad (3)$$

Values of 1×10^{-10}, 3×10^{-10}, and 5×10^{-10} mol/cm^3 for the H_{prod} parameter were tested, meaning that the concentration of hydrogen atoms was increased by that value every 10 μs. The initial substrate was chosen to be circumcoronene and oxidation was allowed to continue until the substrate reached one ring before creating a new substrate. Table 7.10 presents the reaction counts for these sets of simulations.

Table 7.10. Reaction counts for KMC simulations with different rates of atomic hydrogen production.

Reaction	$H_{\text{prod}} \times 10^{10}$ (mol cm^{-3})			
	0	1	3	5
1	160.9	206.7	292.7	382.0
2a	366.3	431.2	546.2	652.3
2b	9.0	10.1	12.0	13.6
3	0.0	0.0	0.0	0.0
4	0.0	0.0	0.0	0.0
5	18.5	18.8	22.7	27.0
6	7.1	7.9	10.3	12.1
7	4.2	4.7	5.9	6.2
8	18.0	19.2	24.4	27.9
9	1.7	1.4	1.8	2.8
10	30.5	33.4	44.2	58.1
11a	29.4	32.4	43.2	56.4
11b	1.1	1.0	1.0	1.6
12	67.1	72.2	96.8	124.3
13a	47.4	51.4	71.2	94.6
13b	0.0	0.0	0.0	0.0
14	0.0	0.0	0.0	0.0
15	0.8	1.1	1.6	1.4
16	2.1	2.3	3.0	3.8

17	1.3	1.0	1.5	1.8
18	0.0	0.0	0.0	0.0
19	0.0	0.0	0.0	0.0
20	0.0	0.0	0.0	0.0
21	0.7	0.9	0.5	1.1
22	0.4	0.2	0.2	0.5
23	0.6	0.6	0.6	0.7
24	3.2	3.1	3.0	4.2
25	0.7	0.7	0.9	1.2
26	0.0	0.0	0.0	0.0
27	0.0	0.0	0.0	0.0
28	0.0	0.0	0.0	0.0
29	0.1	0.1	0.2	0.2
30	0.0	0.0	0.0	0.0
31	0.1	0.1	0.2	0.2
32	0.0	0.0	0.0	0.0
33	0.0	0.0	0.0	0.0
34	0.0	0.0	0.0	0.0
35	0.0	0.0	0.0	0.0
36	0.0	0.0	0.0	0.0
37	0.0	0.0	0.0	0.0
38	0.0	0.0	0.0	0.0
39	0.0	0.0	0.0	0.0
40	0.0	0.0	0.0	0.0
41	0.0	0.0	0.0	0.0
42	0.0	0.0	0.0	0.0
43	0.0	0.0	0.0	0.0
44	0.0	0.0	0.0	0.0
45	0.7	0.9	1.3	1.5
46	0.4	0.3	0.6	0.4
47	0.9	0.6	0.7	0.9
48	1.7	1.9	1.7	2.0
49	1.8	2.1	2.1	1.8
50	7.7	5.7	8.1	5.7
51	1.4	1.4	1.8	1.8
52	3.4	3.1	3.5	4.2
53	5.8	6.3	7.1	7.3
54	6.3	7.2	8.0	8.7
55	1.5	1.6	1.8	2.6
56	3.9	4.2	4.3	5.7
57	4.9	5.6	7.2	8.0
58	5.3	6.3	7.4	8.0
59	38.7	31.3	51.6	42.1
60	0.9	1.0	1.0	1.2
61	2.3	2.5	2.3	3.1

62	3.3	4.0	4.1	4.6
63	3.3	3.5	4.7	4.7
64	114.0	72.0	102.6	66.7
65	0.1	0.1	0.0	0.1
66	0.3	0.7	0.3	0.6
67	0.5	0.6	0.7	0.9
68	0.4	0.6	0.8	0.7
69	125.4	81.6	117.6	78.2
70	0.1	0.0	0.1	0.1
71	0.1	0.1	0.1	0.1
72	0.2	0.2	0.2	0.3
73	0.2	0.2	0.2	0.3
74	6.5	3.8	5.2	3.6
75	0.1	0.0	0.1	0.1
76	0.2	0.2	0.1	0.2
77	0.2	0.1	0.3	0.3
78	0.2	0.2	0.4	0.4
79	3.8	3.3	4.8	3.8
80	0.0	0.0	0.0	0.0
81	0.0	0.0	0.0	0.0
82	0.0	0.0	0.0	0.0
83	0.0	0.0	0.0	0.0
84	2.1	0.9	1.3	0.7
85	0.9	0.8	1.0	1.6
86	1.6	2.3	2.1	3.0
87	2.3	2.7	3.1	3.6
88	2.2	2.6	3.4	3.9
89	40.4	33.6	56.7	45.7
90	0.0	0.0	0.0	0.0
91	0.0	0.0	0.0	0.0
92	206.6	227.5	254.2	271.1
93	0.3	0.5	0.7	0.6
94	2.5	2.7	3.1	3.8
95	2.6	2.0	3.7	3.3
96	1.5	1.8	2.0	1.9
97	3.2	3.9	4.0	5.0
98	4.6	4.8	6.4	8.3
99	4.5	4.7	6.0	6.3
100	0.1	0.1	0.2	0.1
101	0.3	0.3	0.5	0.3
102	0.6	0.5	0.6	0.8
103	0.5	0.5	0.6	0.5
104	15.8	16.6	19.3	20.9

Figure 7.12 shows CO and CO_2 concentration profiles for different rates of hydrogen atom production. For simulations in the previous sections, the formation of CO was seen to taper off at later oxidation times. Here though, the production of hydrogen atoms allows for CO formation to continue at its initial rate. When $H_{prod} = 3 \times 10^{-10}$ mol/cm^3, the CO concentration profile shows good agreement with the magnitude and shape of the experimentally-measured CO concentration profile. The increase in CO concentration when H_{prod} increases is directly linked to the decrease in CO_2 concentration seen at later oxidation times. When H concentration is higher due to hydrogen atom production (as seen in Figure 7.13), the reverse of the reaction $CO + OH \rightarrow CO_2 + H$ becomes favorable and CO_2 goes back to CO.
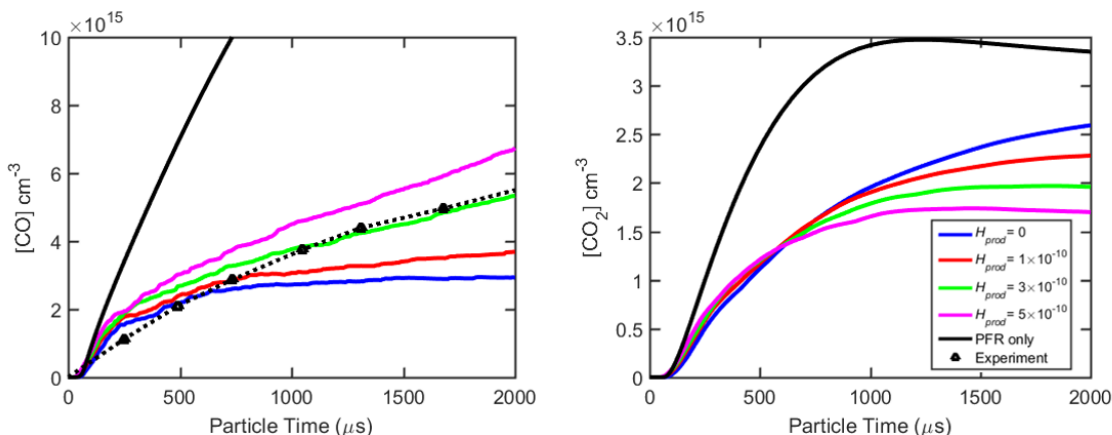

Figure 7.12. CO and CO_2 concentration versus time for KMC simulations with different levels of atomic hydrogen production. Circumcoronene was the initial substrate and the extent of oxidation allowed was 100 %.
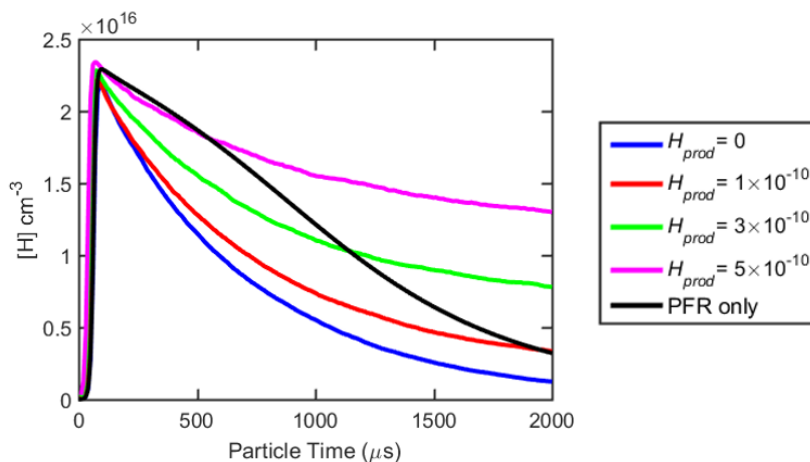

Figure 7.13. [H] versus time for KMC simulations with different rates of atomic hydrogen production. Circumcoronene was the initial substrate and the extent of oxidation allowed was 100 %.

While the frequency of reactions that form radical sites via hydrogen abstraction (reactions 1, 10, 13a, and 92) increased with increasing production of atomic hydrogen, the frequency of radical site deactivation reactions also increased (reactions 2a, 2b, 11a). The net effect

was a modest increase in the event counts for oxidation and thermal desorption reactions as hydrogen production increased, as can be seen in Figure 7.14 and Table 7.11. Presenting the data in terms of the share of carbon atoms removed by oxidation and thermal desorption (Figure 7.15 and Table 7.12) illustrates that increasing hydrogen production had only a marginal effect on the surface reaction oxidation behavior. The share of carbon atoms removed by each type of reaction remained roughly the same for all four cases. These simulations demonstrate that atomic hydrogen production leads to significant changes in the gas phase concentrations of CO, CO_2, and H, but these changes have a smaller effect on the surface oxidation and thermal desorption reaction event counts.
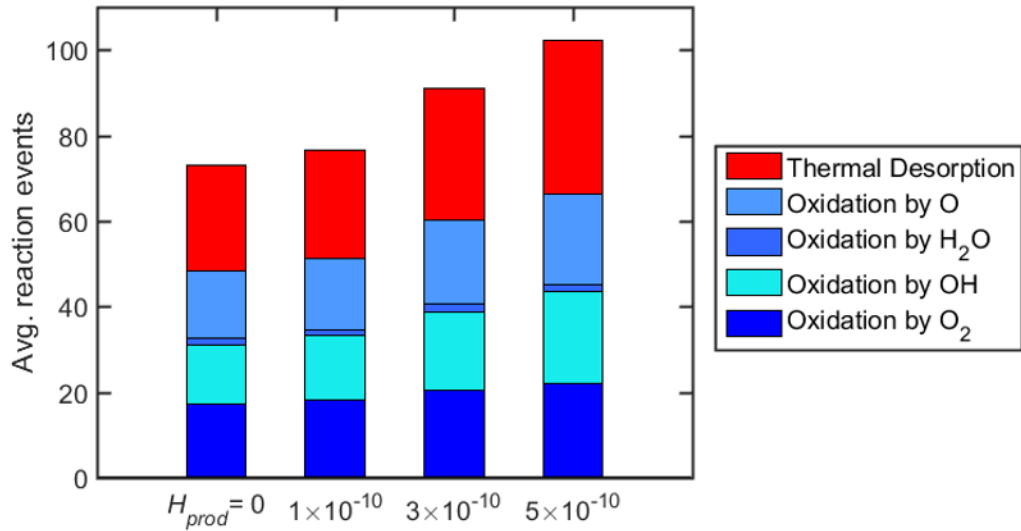

Figure 7.14. Event counts for oxidation and thermal desorption reactions for KMC simulations with different rates of atomic hydrogen production.

Table 7.11. Event counts for oxidation and thermal desorption reactions for KMC simulations with different rates of atomic hydrogen production.

Reactions	$H_{prod} \times 10^{10}$ (mol cm^{-3})			
	0	1	3	5
Oxidation by O_2: R51 – R54, R90	17.0	18.0	20.4	22.0
Oxidation by OH: R96-R99	13.9	15.1	18.4	21.5
Oxidation by H_2O: R100-R103	1.5	1.4	1.9	1.7
Oxidation by O: R104	15.8	16.6	19.3	20.9
Thermal desorption: R5, R7, R17, R25, R45	24.7	25.3	30.9	36.2

Figure 7.15. Share of carbon atoms removed by oxidation and thermal desorption reactions for KMC simulations with different rates of atomic hydrogen production.

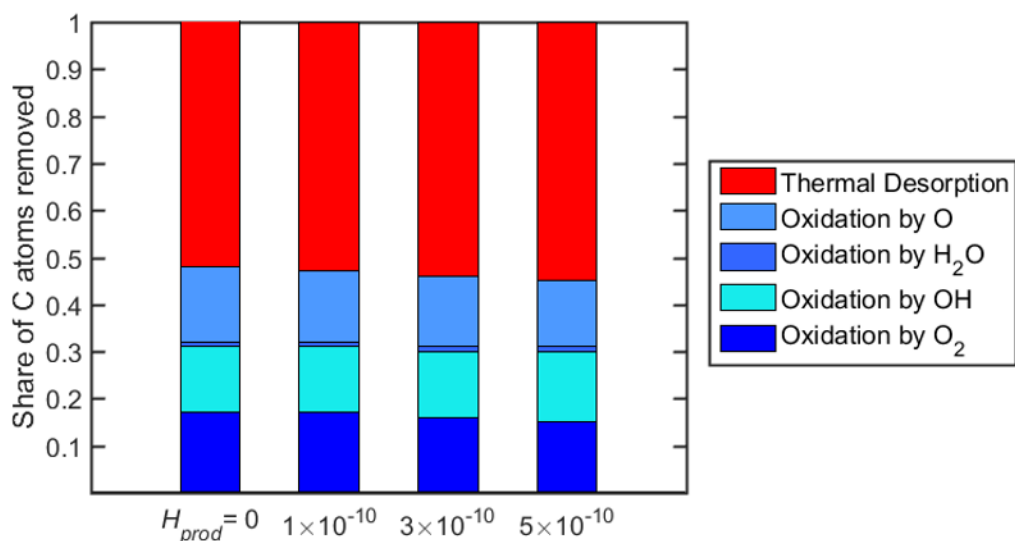Table 7.12. Share of carbon atoms removed by oxidation and thermal desorption reactions for KMC simulations with different rates of atomic hydrogen production.

Reactions	$H_{prod} \times 10^{10}$ (mol cm^{-3})			
	0	1	3	5
Oxidation by O_2: R51 – R54, R90	17.0	18.0	20.4	22.0
Oxidation by OH: R96-R99	13.9	15.1	18.4	21.5
Oxidation by H_2O: R100-R103	1.5	1.4	1.9	1.7
Oxidation by O: R104	15.8	16.6	19.3	20.9
Thermal desorption: R5, R7, R17, R25, R45	24.7	25.3	30.9	36.2

7.4 Summary

The surface chemistry model was augmented to allow for coupling between the surface kinetics and gas phase kinetics. KMC simulations were performed at conditions analogous to those used in high-temperature shock tube experiments done by Roth et al. [93]. The formation rate of CO was found only to depend on substrate size if the substrate was very small (seven rings). Increasing the initial substrate size beyond coronene did not affect the production of CO and CO_2. The substrate shape did not appear to have a significant effect on CO and CO_2 formation either. Decreasing the extent of oxidation allowed before moving on to a new platelet led to increased rates of CO formation and produced CO profiles closer to the PFR-only scenario in which steric effects were not accounted for. The formation of CO was also shown to be sensitive to production of H atoms. Increasing H

production led to an increase in CO and a decrease in CO_2 due to the reverse of the reaction $CO + OH \rightarrow CO_2 + H$ becoming more favorable for higher H concentration. By adjusting modeling parameters (initial substrate, extent of oxidation allowed, and hydrogen production) within reasonable limits, the model did a good job of reproducing the experimental oxidation rates. This analysis shows that the soot oxidation rate depends on gas phase kinetics, steric effects, and how the structure of the soot surface is approximated in models.

8 Summary

This dissertation presented the development of a detailed model of elementary reactions of graphene-edge oxidation and subsequent results of kinetic simulations surface oxidation simulations that utilized the model. The simulations were able to reproduce curvature effects on oxidation rate observed in HRTEM studies [88, 91] and were able to match experimentally measured CO concentration profiles from shock tube experiments of soot oxidation at high-temperature [93]. This detailed model offers further insight into the surface oxidation process.

In Chapter 3, it was determined that the primary pathway for the attack of O_2 on the surface radical site of a graphene-edge six-member ring was the elimination of O and the formation of an oxyradical. The oxyradical could then thermally decompose into a five-member ring and eliminate CO. The computed rate coefficients showed a slight dependence on the number of free edges and size of the PAH, with the rates increasing as the former increases and decreasing as the latter increases. In Chapter 4, oxidation of a graphene-edge five-member ring by O_2 was shown to have a slower rate than oxidation of a six-member ring by several orders of magnitude. The oxidation reactions studied in Chapters 3 and 4, and their corresponding rate coefficients were incorporated into a detailed model of elementary reactions of graphene-edge oxidation. This model was added to a detailed model of soot surface growth.

In Chapter 5, the combined model of surface growth and oxidation reactions were implemented into KMC simulations of graphene-edge oxidation by O_2 at high-temperature. Two principal oxidation pathways were found: thermal decomposition oxyradicals and regeneration of aromatic radical sites. Their competition is temperature-dependent with the former dominating at higher and the latter dominating at lower temperatures. Yet, the overall oxidation rate at the conditions tested was not substantially affected by the presence or absence of the regeneration pathway. This may help in developing reduced models of soot oxidation at flame conditions.

The overall oxidation rate of the graphene substrate was computed to be time-dependent, with reactivity decreasing over time as the ratio of reactive edge sites decreases relative to the number of basal-plane carbon atoms. At the same time, the oxidation rate was found to be higher for graphene with a higher initial curvature. Both results are in accord with experimental observations [88, 91]. Analysis showed that distinct aspects of graphene-edge morphology are responsible for curvature either raising or reducing the oxidative reactivity of the graphene-edge.

In Chapter 6, oxidation of a graphene-edge five-member ring with atomic oxygen was found to be a possible pathway to explain how five-member rings are removed from the substrate. The rate coefficient for oxidation by atomic oxygen exceeded that of oxidation

by molecular oxygen by several orders of magnitude. The detailed surface oxidation model was augmented to include this reaction along with several other oxidation reactions.

In Chapter 7, KMC simulations were then performed in an evolving gas phase environment that was coupled to the surface chemistry for conditions analogous to those of shock tube experiments of soot oxidation at high-temperature. The KMC results showed that the oxidation rate was dependent on several factors including the extent of oxidation allowed for each substrate and the production of H atoms. Oxidation behavior was less sensitive to substrate size and shape. By varying the initial substrate, the extent of oxidation allowed, and the rate of atomic hydrogen production within reasonable bounds, the model was able to reproduce time-dependent CO concentration profiles that are in agreement with experimental measurements [93].

The next step for the detailed surface oxidation model is to be able to match experimental results at low-temperature combustion conditions. This endeavor could be complicated by the fact that different reaction pathways will be favored at low temperatures, and the current model of surface reactions might lack those pathways. If that is the case, quantum chemical and RRKM-ME analyses will need to be conducted to explore those reactions.

Once the KMC model is able to accurately simulate a wide range of soot oxidation conditions, the model will need to be reduced in order to minimize computational expense before it can be implemented into computational fluid dynamics codes of flames. An additional recommendation for the KMC model would be parallelization of the code to decrease computational time. These improvements to the model will facilitate the goal of gaining a better understanding of the process of soot formation.

References

1.   U. S. E. I. Administration, in: *Annual Energy Outlook 2015*, 2015.
2.   B. S. Haynes; H. G. Wagner, Progress in Energy and Combustion Science 7 (4) (1981) 229-273
3.   H. Omidvarborn; A. Kumar; D. S. Kim, J. Environ. Chem. Eng. 2 (2014) 2335-2342
4.   K. K. Shandilya; A. Kumar, Environ. Prog. Sustain. Energy 32 (2013) 1134-1142
5.   J. Xi; B. J. Zhong, Chem. Eng. Tech. 29 (2006) 665-673
6.   H. Omidvarborn; A. Kumar; D. S. Kim; P. K. P. Venkata; V. S. P. Bollineni, J. Hazard Toxic Radioact. Waste 19 (2015)
7.   in: *Soots-Summary of Data Reported and Evaluation*, International Agency for Research on Cancer: 1985; Vol. 35, p 219.
8.   J. Schwartz, Environ. Res. 64 (1994) 36-52
9.   T. C. Bond; S. J. Doherty; D. W. Fahey; P. Forster; T. Berntsen; B. J. DeAngelo; M. G. Flanner; S. Ghan; B. Karcher; D. Koch; S. Kinne; Y. Kondo; P. K. Quinn; M. C. Sarofim; M. G. Schultz; M. Schulz; C. Venkataraman; H. Zhang; S. Zhang; N. Bellouin; S. K. Guttikunda; P. K. Hopke; M. Z. Jacobson; J. W. Kaiser; Z. Klimont; U. Lohmann; J. P. Schwartz; D. Shindell; T. Storelvmo; S. G. Warren; C. S. Zender, J. Geophys. Res-Atmos. 118 (2013) 5380-5552
10.   M. Daly, in: *American Scientist*, 2012.
11.   M. Frenklach, Phys. Chem. Chem. Phys. 4 (11) (2002) 2028–2037
12.   H. Richter; J. B. Howard, Progress in Energy and Combustion Science 26 (2000) 565-608
13.   M. Frenklach, in: Carbon in the Galaxy: Studies From Earth and Space, J. C. Tarter; S. Chang; D. J. DeFrees, (Eds.) NASA Conference Publication 3061: 1990; pp 259-273.
14.   M. Frenklach; H. Wang, Proc. Combust. Inst. 23 (1991) 1559–1566
15.   M. Frenklach; C. A. Schuetz; J. Ping, Proc. Combust. Inst. 30 (2005) 1389-1396
16.   R. Whitesides; D. Domin; R. Salomón-Ferrer; W. A. Lester Jr; M. Frenklach, Proc. Combust. Inst. 32 (2009) 577–583 http://dx.doi.org/10.1016/j.proci.2008.06.096.
17.   R. Whitesides; D. Domin; R. Salomón-Ferrer; W. A. Lester, Jr.; M. Frenklach, J. Phys. Chem. A 112 (10) (2008) 2125–2130 doi:10.1021/jp075785a.
18.   R. Whitesides; A. C. Kollias; D. Domin; W. A. Lester Jr; M. Frenklach, Proc. Combust. Inst. 31 (2007) 539–546 http://dx.doi.org/10.1016/j.proci.2006.07.034.
19.   X. You; R. Whitesides; D. Zubarev; W. A. Lester Jr; M. Frenklach, Proc. Combust. Inst. 33 (2011) 685–692 http://dx.doi.org/10.1016/j.proci.2010.05.110.
20.   A. Violi, J. Phys. Chem. A 109 (34) (2005) 7781-7787
21.   R. Whitesides; M. Frenklach, J. Phys. Chem. A 114 (2) (2010) 689–703 10.1021/jp906541a.
22.   J. Appel; H. Bockhorn; M. Frenklach, Combust. Flame 121 (2000) 122–136
23.   T. Yu; M. C. Lin, J. Am. Chem. Soc. 116 (1994) 9571-9576
24.   K. G. Neoh; J. B. Howard; A. F. Sarofim, in: Particulate Carbon: Formation During Combustion, D. C. Siegla; G. W. Smith, (Eds.) Plenum: New York, 1981; pp 261-282.
25.   M. S. Celnik; M. Sander; A. Raj, Proc. Combust. Inst. 32 (2009) 639-646

26.   K. Brezinsky, Progress in Energy and Combustion Science 12 (1986) 1-24
27.   C.-Y. Lin; M. C. Lin, Int. J. Chem. Kinet. 17 (1985) 1025
28.   C.-Y. Lin; M. C. Lin, J. Phys. Chem. 90 (1986) 425
29.   P. Frank; J. Herzler; T. Just; C. Wahl, Proc. Combust. Inst. 25 (1994) 833
30.   R. Liu; K. Morokuma; A. M. Mebel; M. C. Lin, J. Phys. Chem. 100 (1996) 9314
31.   I. V. Tokmakov; G.-S. Kim; V. V. Kislov; A. M. Mebel; M. C. Lin, J. Phys. Chem. A 109 (27) (2005) 6114–6127 10.1021/jp051712k.
32.   L. R. Radovic, J. Am. Chem. Soc. 131 (2009) 17166–17175 10.1021/ja904731q.
33.   D. Y. Zubarev; N. Robertson; D. Domin; J. McClean; J. Wang; W. A. Lester, Jr.; R. Whitesides; X. You; M. Frenklach, J. Phys. Chem. C 114 (12) (2010) 5429–5437 10.1021/jp9058615.
34.   D. Y. Zubarev; X. You; J. McClean; W. A. Lester, Jr.; M. Frenklach, J. Mater. Chem. 21 (2011) 3404–3409
35.   D. E. Edwards; X. You; D. Y. Zubarev; W. A. Lester Jr; M. Frenklach, Proc. Combust. Inst. 34 (2013) 1759–1766 http://dx.doi.org/10.1016/j.proci.2012.05.031.
36.   X. You; D. Y. Zubarev; W. A. Lester, Jr.; M. Frenklach, J. Phys. Chem. A 115 (49) (2011) 14184–14190 10.1021/jp208974b.
37.   I. Glassman; R. A. Yetter; N. G. Glumac, Combustion, Academic, San Diego, CA, 2015, p.^pp.
38.   D. E. Edwards; D. Y. Zubarev; W. A. Lester; M. Frenklach, J. Phys. Chem. A 118 (37) (2014) 8606-8613
39.   J. R. Barker, Int. J. Chem. Kinet. 33 (2001) 232–245
40.   J. R. Barker, Int. J. Chem. Kinet. 41 (2009) 748–763
41.   J. R. Barker; T. L. Nguyen; J. F. Stanton; C. Aieta; M. Ceotto; F. Gabas; T. J. D. Kumar; C. G. L. Li; L. L. Lohr; A. Maranzana; N. F. Ortiz; J. M. Preses; P. J. Stimac, in: 2016.0 ed.; University of Michigan, Ann Arbor, MI, 2016.
42.   D. T. Gillespie, J. Phys. Chem. 81 (25) (1977) 2340-2361
43.   D. T. Gillespie, Markov processes: An introduction for physical scientists, Academic Press, San Diego, CA, 1992, p.^pp.
44.   R. G. Gilbert; S. C. Smith, Theory of Unimolecular and Recombination Reactions, Blackwell-Scientific, Oxford, U.K., 1990, p.^pp.
45.   H. Hippler; J. Troe; H. J. Wendelken, J. Chem. Phys. 78 (1983) 6709-6717
46.   H. Wang; M. Frenklach, Combust. Flame 96 (1994) 163–170
47.   S. J. Klippenstein, Chem. Phys. Lett. 170 (1) (1990) 71–77 http://dx.doi.org/10.1016/0009-2614(90)87092-6.
48.   S. J. Klippenstein; A. F. Wagner; R. C. Dunbar; D. M. Wardlaw; S. H. Robertson, in: 1.00 ed.; Argonne National Laboratory, Argonne, IL: 1999.
49.   M. Frenklach, J. Chem. Phys. 97 (1992) 5794-5802
50.   M. Frenklach, Phys. Rev. B 45 (1992) 9455-9458
51.   P. Mitchell; M. Frenklach, Proc. Combust. Inst. 27 (1998) 1507-1514
52.   M. Frenklach, Proc. Combust. Inst. 26 (1996) 2285-2293
53.   R. Whitesides; M. Frenklach, Z. Phys. Chemie   (2014) 1-18
54.   N. L. Allinger; Y. H. Yuh; J. H. Lii, J. Am. Chem. Soc. 111 (23) (1989) 8551-8566
55.   J. W. Ponder, in: 4.2 ed.; Washington University School of Medicine: Saint Louis, MO, 2004.

56.   R. L. Murry; J. R. Colt; G. E. Scuseria, J. Phys. Chem. 97 (19) (1993) 4954-4959
57.   J. M. Schulman; R. L. Disch, J. Comput. Chem. 19 (2) (1998) 189-194
58.   R. Meana-Paneda; D. G. Truhlar; A. Fernandez-Ramos, J. Chem. Phys. 134 (9) (2011)
59.   J. T. Jodkowski; M. T. Rayez; J. C. Rayez, J. Phys. Chem. A 103 (1999) 3750-3765
60.   Y. Hidaka; T. Oki; H. Kawano; T. Higashihara, J. Phys. Chem. 93 (1989) 7134-7139
61.   T. Asaba; N. Fujii, Proc. Int. Symp. Shock Tube Waves 8 (1971) 1-12
62.   T. Seta; M. Nakajima; A. Miyoshi, J. Phys. Chem. A 110 (2006) 5081-5090
63.   H. I. Leidreiter; H. G. Wagner, Z. Phys. Chem. 165 (1989) 1
64.   H. Dong; Y. H. Ding; C. C. Sun, J. Chem. Phys. 122 (2005) 064303
65.   J. Schaugg; R. S. Tranter; H.-H. Grotheer, Proceedings of the 8th International Symposium on Transport Phenomena in Combustion   (1995) 130-141
66.   G. R. da Silva; J. W. Bozzelli, J. Phys. Chem. A 112 (2008) 3566-3575
67.   A. M. Mebel; M. C. Lin, J. Am. Chem. Soc. 116 (1994) 9577-9584
68.   B. K. Carpenter, J. Am. Chem. Soc. 115 (1993) 9806-9807
69.   X. Gu; F. Zhang; R. I. Kaiser, Chem. Phys. Lett. 448 (2007) 7-10
70.   D. S. N. Parker; F. Zhang; R. I. Kaiser, J. Phys. Chem. A 115 (2011) 11515-11518
71.   D. R. Albert; H. F. Davis, J. Phys. Chem. Lett. 1 (2010) 1107-1111
72.   D. S. N. Parker; R. I. Kaiser; T. P. Troy; O. Kostko; M. Ahmed; A. M. Mebel, J. Phys. Chem. A in press (2014) 10.1021/jp509170x.
73.   N. M. Marinov; W. J. Pitz; C. K. Westbrook; A. M. Vincitore; M. J. Castaldi; S. M. Senkan; C. F. Melius, Combust. Flame 114 (1998) 192-213
74.   J. Park; Z. F. Xu; M. C. Lin, J. Phys. Chem. A 113 (2009) 5348-5354
75.   C.-W. Zhou; V. V. Kislov; A. M. Mebel, J. Phys. Chem. A 116 (6) (2012) 1571–1585 10.1021/jp2119313.
76.   V. V. Kislov; R. I. Singh; D. E. Edwards; A. M. Mebel; M. Frenklach, Proc. Combust. Inst. 35 (2015) 1861-1869 http://dx.doi.org/10.1016/j.proci.2014.06.135.
77.   H. W. Kroto, Nature 329 (6139) (1987) 529-531
78.   T. G. Schmalz; W. A. Seitz; D. J. Klein; G. E. Hite, J. Am. Chem. Soc. 110 (4) (1988) 1113-1127
79.   R. F. Curl; R. E. Smalley, Sci. Am. 265 (4) (1991) 54-&
80.   J. Aihara, J. Am. Chem. Soc. 117 (14) (1995) 4130-4136
81.   A. Raj; S. Y. Yang; D. Cha; R. Tayouo; S. H. Chung, Combust. Flame 160 (2013) 1812-1826
82.   R. I. Singh; A. M. Mebel; M. Frenklach, J. Phys. Chem. A 119 (2015) 7528-7547
83.   A. Raj; G. R. da Silva; S. H. Chung, Combust. Flame 159 (2012) 3423-3436
84.   M. Frenklach; L. B. Ebert, J. Phys. Chem. 92 (2) (1988) 561-563 Doi 10.1021/J100313a061.
85.   M. Frenklach; D. W. Clary; W. C. Gardiner, Jr.; S. E. Stein, Proc. Combust. Inst. 20 (1985) 887-901
86.   J. M. Thomas; E. E. G. Hughes, Carbon 1 (1964) 209-214
87.   M. Acik; Y. J. Chabal, Jap. J. Appl. Phys. 50 (2011) 070101

88.   R. Vander Wal; A. Yezerets; N. W. Currier; D. H. Kim; C. M. Wang, Carbon 45 (2007) 70-77
89.   I. C. Jaramillo; C. K. Gaddam; R. L. Vander Wal; J. S. Lighty, Combust. Flame 162 (2015) 1848-1856 10.1016/j.combustflame.2014.12.006.
90.   H. L. Fang; M. J. Lance, in: *SAE Technical Paper 2004-01-3043,*, 2004.
91.   R. Vander Wal; A. J. Tomasek, Combust. Flame 134 (2003) 1-9
92.   X. You; H. M. Wang; H. B. Zhang; M. J. Pilling, Phys. Chem. Chem. Phys. 18 (2016) 12149-12162
93.   P. Roth; O. Brandt; S. Von Gersum, Proc. Combust. Inst. 23 (1991) 1485–1491 http://dx.doi.org/10.1016/S0082-0784(06)80417-0.
94.   J. Nagle; R. F. Strickland-Constable, in: Proceedings of the Fifth Carbon Conference, Pergamon: Oxford, 1962; Vol. 1, pp 154-164.
95.   J. R. Walls; R. F. Strickland-Constable, Carbon 1 (1964) 333
96.   K. B. Lee; M. W. Thring; J. M. Beer, Combust. Flame 6 (1962) 137
97.   D. E. Rosner; H. D. Allendorf, A.I.A.A. J. 6 (1969) 640
98.   D. E. Rosner; H. D. Allendorf, Proc. 3rd Int. Symp. High Temp. Tech. (1967)
99.   D. E. Rosner; H. D. Allendorf, Carbon 3 (1965) 153
100.   D. E. Rosner; H. D. Allendorf, Carbon 7 (1969) 515
101.   S. W. Radcliffe; J. P. Appleton, Combust. Sci. Tech. 4 (1971) 171
102.   C. Park; J. P. Appleton, Combust. Flame 20 (1973) 369
103.   C. Park; J. P. Appleton, 9th Symp. on Shock Waves (1973) 793
104.   T. W. Lester; W. R. Seeker; J. F. Merkin, Rev. Sci. Instrum. 51 (1980) 1523
105.   T. W. Lester; W. R. Seeker; J. F. Merkin, 18th Symp. on Comb. (1981) 1257
106.   W. Felder; S. Madronich; D. B. Olsen, Energy Fuels 2 (1988) 743
107.   O. Brandt; P. Roth, Combust. Flame 77 (1989) 69
108.   P. Roth; S. von Gersum, J. Aerosol Sci. 21 (1990) 31
109.   C. P. Fennimore; G. W. Jones, J. Phys. Chem. 71 (1967) 593
110.   M. Frenklach, in: *PrIMe Kinetics ReactionLab, https://github.com/PrIMeKinetics/ReactionLab*, 2016.
111.   X. You; A. Packard; M. Frenklach, Int. J. Chem. Kinet. 44 (2012) 101-116
112.   A. Burcat; B. Ruscic ftp://ftp.technion.ac.il/pub/supported/aetdd/thermodynamics/
113.   G. P. Smith; D. Golden; M. Frenklach; N. W. Moriarty; B. Eiteneer; M. Goldenberg; C. T. Bowman; R. Hanson; S. Song; W. C. Gardiner, Jr.; V. Lissianski; Z. Qin http://www.me.berkeley.edu/grimech/
114.   W. Tsang; R. F. Hampson, J. Phys. Chem. Ref. Data 15 (1986) 1087-1279
115.   M. Conaire; H. J. Curran; J. M. Simmie; W. J. Pitz; C. K. Westbrook, Int. J. Chem. Kinet. 36 (2004) 603-622
116.   J. Troe, Proc. Combust. Inst. 28 (2000) 1463-1469
117.   D. L. Baulch; C. J. Cobos; R. A. Cox; C. Esser; P. Frank; T. Just; J. A. Kerr; M. J. Pilling; J. Troe; R. W. Walker; J. Warnatz, J. Phys. Chem. Ref. Data 21 (1992) 411-734
118.   S. G. Davis; A. V. Joshi; H. Wang; F. Egolfopoulos, Proc. Combust. Inst. 30 (2005) 1283-1292
119.   Z. Hong; R. D. Cook; D. F. Davidson; R. Hanson, J. Phys. Chem. A 114 (2010) 5718-5727
120.   Z. Hong; S. S. Vasu; D. F. Davidson; R. Hanson, J. Phys. Chem. A 114 (2010) 5520-5525

121.   J. V. Michael; J. W. Sutherland; L. B. Harding; A. F. Wagner, Proc. Combust. Inst. 28 (2000) 1471-1478
122.   D. L. Baulch; C. T. Bowman; C. J. Cobos; R. A. Cox; T. Just; J. A. Kerr; M. J. Pilling; D. Stocker; J. Troe; W. Tsang; R. W. Walker; J. Warnatz, J. Phys. Chem. Ref. Data 34 (2005) 757
123.   A. Lifshitz; M. Bidani; H. F. Carroll, Proc. Sym. Shock Tubes and Waves 13 (1982) 602-609
124.   M. Frenklach. Hebrew University, 1976.